To the Graduate Council:
I am submitting herewith a dissertation written by Guoming Guan entitled "On the Analysis of Emission Spectra and Interference Images." I have examined the final copy of this dissertation for form and content and recommend that it be accepted in partial fulfillment of the requirements for the degree of Doctor of Philosophy, with a major in Physics.

Christia Parigger

Dr. Christian Parigger, Major Professor

We have read this dissertation
and recommend its acceptance:

Dr. J. W. L. Lewis

Dr. D. R. Keefer

Dr. H. W. Crater

Dr. L.M. Davis

Accepted for the Council:

Associate Vice Chancellor
and Dean of The Graduate School

On the Analysis of Emission Spectra and Interference Images

A Dissertation

Presented for the

Doctor of Philosophy

Degree

The University of Tennessee, Knoxville

Guoming Guan

May 1999

Dedication

Dedicated to my parents

Acknowledgements

I would like to thank Dr. Christian Parigger for his instructions, advice and assistance in numerical and experimental aspects of this work. I am deeply grateful to Dr. J. W. L. Lewis who has been very supportive throughout the course of my studies and very concise in his many stimulating remarks on this subject. I am also deeply grateful to Dr. Lloyd Davis for his critical remarks. The comments of the other committee members, Dr. Horace Crater and Dr. Dennis Keefer, are greatly appreciated.

I would also like to thank the staff in the Center for Laser Applications: Newton Wright, Jim Few, Jim Hornkohl, Fred Schwartz, Penny Oliver, Carole Thomas and Lisa Turner, for their assistance and advice.

Last but not least I express my thanks to my at the time fellow students for their interest and help, in particular, Ivan Dors, Yuanji Tang, Yuxing Sun and Drs Yingling Chen and David Plemmons.

The work is in part supported by the National Science Foundation under Grant No. CTS-9512489, and by a grant of high performance computer (HPC) time from the Department of Defense (DOD) HPC Center, AEDC at Arnold AFB, for numerical work on the 64 processor Origin 2000 machine. Finally I gratefully acknowledge support from UTSI's Center for Laser Applications.

Abstract

This dissertation addresses the analysis of emission spectra and interference images to determine spectroscopic temperature and ultra-short laser pulse width, respectively. Of particular interest are data fitting methods and techniques. The eigen-analysis technique is elaborated for the determination of the number of significant experimental data. Results of extensive Monte Carlo simulations are presented.

Emission spectra from 1064-nm Nd:YAG laser-induced air breakdown are compared with synthetic spectra to obtain the spectroscopic temperature of the transient plasma. Some 40-300 μs after optical breakdown, OH contributions dominate the emission spectrum in the wavelength range of 305-322 nm. Background emission and line profile effects are investigated in the data reduction of recorded plasma spectra. The background shows a strong correlation with temperature while the line profile is weakly correlated with temperature. The variance of the spectroscopic temperature is proportional to the magnitude of the variation of the data.

The autocorrelation function of ultra-short laser pulses is measured by systematically varying the time delay of crossed beams and recording interference patterns. The analysis is performed by the use of Fourier transform techniques to separate the interference cross term from the low-frequency background. A single autocorrelation coefficient is determined from each image. The average coherence length is obtained by fitting the autocorrelation coefficients with a model autocorrelation function.

Contents

List of Figures

List of Tables

Chapter 1

Introduction

The focus of this dissertation is on the analysis of emission spectra and interference images. Data analysis is an essential part of an experiment or a measurement. There are many discussions on data analysis. Two important references are mentioned here. S. L. Meyer [1], P. R. Bevington and D. K. Robinson [2] elaborated the concepts, the techniques and the formulations of the data analysis in their books. The techniques and representations of data analyses are common for most types of data. Least-square fitting is most commonly used to find values for physical quantities. Monte Carlo simulation provides a powerful technique in error analysis.

Typical types of measured data sets are results of integrations. The quantity of interest, which is in the integrand, is obtained by inverting an integral equation. The integral equations are frequently in the form of the Fredholm integral equation of first kind. Mathematical discussions of the Fredholm integral equation of the first kind can be found in the works collected by C. W. Groetsch[3] and H. Stark[4]. From the point of view of applications in physics, S. Twomey[5, 6], J. Y. Wang [7], J. Heintzenberg [8], C. D. Capps [9], G. Viera [10, 11, 12, 13] and A. Ben-David

[14, 15] studied the solution of the integral equation and published their results. One graduate of UTSI, Dr. Feng Sun, investigated the optical measurement of particle size distribution function by inverting Fredholm integral equations of the first kind [16]. The eigen-analysis technique can be used to obtain the information of significant number of data for a set of kernels.

Spectroscopic methods are frequently used to determine temperature in the investigation of reactive gas phase systems such as flames or plasmas. The theoretical principle is based on the assumption that atoms (or molecules) are distributed among different quantum states in equilibrium according to the Boltzmann distribution. Laser induced fluorescence (LIF) is frequently used for the temperature measurement [17, 18, 19, 20, 21, 22]. Temperature determination by LIF is usually based on atom (or molecule) distribution of ground electronic states. Measurements of emission spectra can also yield temperature information [23, 24, 25]. Temperature determination from an emission spectrum is based on atom (or molecule) distribution in the excited states.

For temperature determination, two methods are often used: Boltzmann plot and direct least-square fitting of a measured spectrum. The Boltzmann plot technique requires the intensities of individual transitions. The temperature is linearly dependent on the logarithms of the intensities and can be found by the use of straight line fitting. It is easy to find out the error propagation equations for the straight line fitting[2]. Direct, weighted least-square fitting may be preferred for the determination of spectroscopic temperature. This is especially useful when the standard

Boltzmann plot techniques are not applicable. The error analyses for direct nonlinear least-square fitting is complicated. The analytical equation of error propagation may be found by the use of the parabolic approximation [26]. Generally Monte Carlo simulations may be utilized in the investigation of error propagation.

Theoretical prediction of an emission spectrum from many species may be calculated by the use of the nonequilibrium air radiation code [27, 28] (NEQAIR) with an assumed equilibrium temperature and the concentration of species as input. Diatomic radicals are transiently present in a wide variety of reactive gas phase systems. Their emissions may dominate the emission spectra in certain wavelength regimes. The spectral structures of particular transitions for selected diatomic molecules can be predicted well from reported spectroscopic data. The emission spectra may be fitted with the dominant spectra of the diatomic molecules while the contributions from the other species are considered as constant.

In this dissertation, the spectroscopic emission spectra from laser-induced micro-plasma are investigated. NEQAIR calculations give an overview of the emission spectrum. The emission from the hydroxyl radical (OH) dominates the emission spectra in the range of 305-322 nm subsequent to laser-induced breakdown typically at delay time of 40-300 μs. The emission spectra are fitted with synthetic OH spectra to determine the temperature of the micro-plasma at different delay times. Monte Carlo simulations are used in the error analysis of the inferred spectroscopic temperature.

An interference image contains information of the two interfering beams. The

contrast ratio is obtained directly from the maximum and minimum of the interference intensities. The first-order coherence may approximately be obtained from the contrast ratio [29]. However, the determination of the maximum and the minimum is usually not accurate and a vast amount of data other than the maximum or the minimum is not used. The Fourier transform technique provides a unique method to decompose the intensity among spatial frequencies in the analysis of images [30, 31, 32]. The interference term is separated from the background of low spatial frequency. The autocorrelation function is determined from this interference term. Data fitting techniques are applied to obtain a measure of the pulse width.

In this dissertation, the interference of femtosecond pulses is investigated. A CCD camera is used to record the interference patterns of two time-delayed beams. The interference pattern is transformed into the spatial frequency domain by use of the Fourier transform technique. The interference term is isolated from the background. An autocorrelation coefficient is obtained by integrating the interference term. The autocorrelation function is obtained from the scan of the overlap of two interference terms. The coherence length is determined by fitting the measured autocorrelation function with a model autocorrelation function.

Chapter 2

Formulation of Data Analyses

2.1 Introduction

The analysis of data or data sets is typically accomplished by the use of digital computers and packaged algorithms. In this dissertation several methods of data analyses are evaluated and applied. We are interested in measurement processes that are formulated by the following integral equation:

$$g(y) = \int_a^b K(y,x)f(x)dx, \tag{2.1}$$

where $K(y,x)$ is the Kernel function. $g(y)$ is usually determined from a measurement and $K(y,x)$ is determined from the experimental arrangement. $f(x)$ is the unknown function of interest. Of particular interest are discrete kernels of the form:

$$g_j = \int_a^b K_j(x)f(x)dx, \tag{2.2}$$

where j=1, 2, ..., M.

Equations (2.1) and (2.2) are known as the type of Fredholm integral equation of the first kind. Typically, deconvolution methods need to be applied to find the quantity of interest f(x). In an ideal measurement, the kernel function may be

represented by a dirac-delta distribution $\delta(x-y)$, and the quantity of interest equals the measured function g(y). An example for such an "ideal" measurement would be the measurement of a spectral line with an instrument (viz. spectrometer) resolution much less than the line width. Usually we are interested in discrete kernels where the indices $j = 1, 2, ..., M$ indicate the M different, discrete measurements of the function f(x).

The numerical solution $f(x)$ to Equation (2.2) can be achieved by the use of digital computers. For orthogonal kernels the process of inversion is simple and direct. For non-orthogonal kernels the inversion can become complicated. The interdependence of the kernels is determined by the eigenvalues of the covariance matrix and the error magnitude or the relative information. As an application of the general method, the interdependence of Gaussian kernels is investigated methodically for different line-widths, intervals and numbers of kernels.

The errors in $g(y)$ may be magnified by the small eigenvalues in direct inversion so that the quantity $f(x)$ is buried in the error noise. Some regularizations (or constraints) were proposed [3, 4, 5] to restrict the error magnification. One of these techniques is singular value decomposition (SVD) in which the error magnification can be suppressed by discarding the small eigenvalues. An alternative method to solve integral equations with an assumption of a model $f(x)$ is by the use of least-square fitting method.

2.2 On Fredholm Integral Equation of the First Kind

A Fredholm integral equation of the first kind occurs in the fields of scattering, tomography, image restoration, and system identification. Two subsets of the Fredholm integral equation of the first kind are the convolution and correlation integral equations. There is no general solution for the Fredholm integral equation except for some special kernels. These special kernels are summarized below.

The solution $f(x)$ is the well-known Fourier transform of $g(y)$ if $K(y,x)$ is a function such as e^{ixy}, e^{-ixy}, $cos(xy)$, or $sin(xy)$. The solution $f(x)$ is the Laplace transform of $g(y)$ if $K(y,x)$ is an exponential function of the form e^{-xy}. The solution $f(x)$ is the following [33] if $K(y,x)$ is the Gaussian of form $e^{-(x-y)^2}$:

$$f(x) = \frac{1}{\pi^{1/2}} \sum_{n=0}^{\infty} \frac{g^{(n)}(0)}{2^n n!} \mathcal{H}_n(x), \tag{2.3}$$

where $\mathcal{H}_n(x)$ is an n^{th}-order Hermite polynomial and $g^{(n)}(0)$ is the value at $y = 0$ of n^{th}-order derivative of $g(y)$.

2.3 Interdependence of Kernels

Discrete kernels are discussed in the following. S. Twomey [5] studied the interdependence of M kernels in the Fredholm integral equation of the first kind (Eq. (2.2)) and he introduced the terminology "information content" to describe the interdependence of the kernels. In this section the kernel interdependence and error magnification will be discussed according to S. Twomey's description. Aspects of

error magnification are also discussed in the next section.

The eigenanalysis method is elaborated for M kernels in the following. To accomplish the analyses mathematically, one first introduces a function $h(x)$,

$$h(x) = \sum_{j=1}^{M} a_j K_j(x), \tag{2.4}$$

with constraint $\sum a_j^2 = 1$ of the set of real numbers $\{a_j\}$.

One first introduces the concepts of orthogonal kernels and linear dependent kernels. Two kernels are orthogonal if

$$\int_a^b K_i^*(x) K_j(x) dx = 0. \tag{2.5}$$

The kernels are orthogonal if any two of the kernels are orthogonal. Otherwise, the kernels are non-orthogonal.

The kernels $\{K_j(x)\}$ are linearly dependent if there exists a set of $\{a_j\}$ so that $h(x) = 0$. Otherwise, the kernels are independent. Orthogonal kernels are independent kernels.

One second calculates the integration of the square of the function $f(x)$,

$$\begin{aligned} \int_a^b |h(x)|^2 dx &= \int_a^b |\sum_j a_j K_j(x)|^2 dx = \sum_i \sum_j a_i^* a_j \int_a^b K_i^*(x) K_j(x) dx \\ &= \mathbf{a}^+ \mathbf{C} \mathbf{a}, \end{aligned} \tag{2.6}$$

where $\mathbf{C}$ is called covariance matrix, $C_{ij} = \int_a^b K_i^*(x) K_j(x) dx$, and the vector $\mathbf{a}$ represents the set $\{a_j\}$. Of particular importance are the eigenvalues of the covariance matrix. These are found by diagonalizing the covariance matrix $\mathbf{C}$,

$$\mathbf{U}^+ \mathbf{C} \mathbf{U} = \mathbf{\Lambda}, \tag{2.7}$$

where the columns of $\mathbf{U}$ consist of corresponding eigenvectors $\{\mathbf{u}_l\}$ of the matrix $\mathbf{C}$. The diagonal elements of $\mathbf{\Lambda}$ are the eigenvalues of the matrix $\mathbf{C}$.

The eigenvectors $\{\mathbf{u}_l\}$ are then used as the basis for the expansion of the vector $\mathbf{a}$,

$$\mathbf{a} = \sum_i \beta_i \mathbf{u_i} = \mathbf{U}\beta. \tag{2.8}$$

Here the vector β represents of the set of expansion coefficients $\{\beta_i\}$. $\sum \beta_i^2 = 1$ since the constraint $\sum a_j^2 = 1$ implies $\mathbf{a}^+\mathbf{a} = \beta^+\mathbf{U}^+\mathbf{U}\beta = \beta^+\beta = 1$. Therefore,

$$\int_a^b |h(x)|^2 dx = \mathbf{a}^+\mathbf{C}\mathbf{a} = \sum_i \lambda_i \beta_i^2 \geq \sum_i \lambda_{min}\beta_i^2 = \lambda_{min}, \tag{2.9}$$

where the subscript *min* represents the number corresponding to the minimum eigenvalue. The minimum of the integration $\int_a^b |h(x)|^2 dx$ is the smallest eigenvalue λ_{min} when $\beta_{min} = 1$ and $\beta_i = 0$ for the others, or $\mathbf{a} = \mathbf{u}_{min}$ according to Eq. (2.8).

One third assumes a_l is the largest among the set of coefficients $\{a_j\}$ for the minimum of $\int_a^b |h(x)|^2 dx$ and expresses $K_l(x)$ as a sum of $h(x)$ and of the other kernels:

$$K_l(x) = -\frac{1}{a_l}\sum_{l\neq j} a_j K_j(x) + \frac{1}{a_l}h(x). \tag{2.10}$$

Substitution of $K_l(x)$ into Eq. (2.2) yields

$$g_l = -\frac{1}{a_l}\sum_{l\neq j} a_j g_j + \frac{1}{a_l}\int_a^b h(x)f(x)dx. \tag{2.11}$$

The equation implies that specific data, g_l, is predicted by the other data and an additional integral-term. g_l is totally predicted by the other data if the kernels are dependent.

It is discussed in the following whether this integral-term in Eq. (2.11) can be neglected compared to the errors of the data. One models experiment data by

$$g_j^e = g_j + \epsilon_j, \tag{2.12}$$

where g_j^e is the measured value, g_j is determined by Eq. (2.2), and ϵ_j includes both random and systematic errors. Upon substitution of g_j of Eq. (2.11) into Eq. (2.12), one finds:

$$\begin{aligned} g_l^e &= g_l + \epsilon_l = -\frac{1}{a_l}\sum_{l\neq j} a_j(g_j^e - \epsilon_j) + \frac{1}{a_l}\int_a^b h(x)f(x)dx + \epsilon_l \\ &= -\frac{1}{a_l}\sum_{l\neq j} a_j g_j^e + \frac{1}{a_l}\int_a^b h(x)f(x)dx + \frac{1}{a_l}\sum_{j=1}^{M} a_j\epsilon_j. \end{aligned} \tag{2.13}$$

The additional information in l^{th}-data is masked by the errors (or noise) if the value of the integral-term (second term) is less than the sum-term (third term) that contains the errors. This comparison of the integral-term and the error-term indicates the set of data to be kept to describe the measurement. For the mentioned comparison, one applies the mean value theorem and uses $\int_a^b h(x)^2dx = \lambda_{min}$ at the minimum,

$$|\int_a^b h(x)f(x)dx|^2 = f_m^2|\int_a^b h(x)dx|^2 \leq f_m^2\int_a^b h^2(x)dx = f_m^2\lambda_{min}. \tag{2.14}$$

Therefore, the kernels are independent only if

$$f_m^2\lambda_{min} > |\sum_{j=1}^{M} a_j\epsilon_j|^2. \tag{2.15}$$

$|\sum_{j=1}^{M} a_j\epsilon_j|^2$ is the length of the projection of the error vector ϵ on the unit vector $\{a_1, a_2, ..., a_l, ..., a_M\}$.

2.4 Direct Inversion and Error Magnification

In this section, the direct inversion of the integral equation is addressed. First the concept is introduced of Lebesgue (L^2) space of [a, b] and of the orthonormal basis $\phi_i(x)$, i=0, 1, 2, ... which span the L^2 space. The function $f(x)$ and the set of kernels $\{K_j(x)\}$ can be expanded by the use of this orthonormal basis,

$$f(x) = \sum \xi_i \phi_i(x), \tag{2.16}$$

$$K_j(x) = \sum \eta_{ji} \phi_i(x). \tag{2.17}$$

M kernels span an L^2 subspace. Consequently, $f(x)$ may be decomposed as $s(x)$, "inside" this subspace, and $r(x)$, "outside" the subspace as denoted by C. D. Capps et al. [9]. This is formally written as follows,

$$f(x) = s(x) + r(x). \tag{2.18}$$

Any component that is outside this subspace can not be represented by the kernels, or $\int_a^b K_j(x) r(x) dx = 0$. Therefore, only $s(x)$ is determined from the integral equation.

For direct inversion, one constructs the orthonormal basis $\{\phi_j(x)\}$ in the subspace by using the eigenvectors of the covariance matrix $\mathbf{C}$. The vectors $\phi(x)$, $\mathbf{K}(x)$, ξ and η represent the sets $\{\phi_j(x)\}$, $\{K_j(x)\}$, $\{\xi_j\}$ and $\{\eta_j\}$, respectively,

$$\phi(x) = \mathbf{\Lambda}^{-1/2} \mathbf{U}^{+} \mathbf{K}(x). \tag{2.19}$$

Now, one can deduce the expansion coefficients of Eq. (2.16). The expansion coefficients of $f(x)$ is:

$$\xi = \int_a^b \phi(x) f(x) dx = \int_a^b \mathbf{\Lambda}^{-1/2} \mathbf{U}^{+} \mathbf{K}(x) f(x) dx$$

$$= \mathbf{\Lambda^{-1/2}U^{+}g}. \tag{2.20}$$

It is noted that $r(x)$ is outside the subspace and these expansion coefficients constitute $s(x)$ only. Therefore, $s(x)$ becomes

$$s(x) = \phi^{+}(\mathbf{x})\xi = \mathbf{K^{+}(x)U\Lambda^{-1}U^{+}g}. \tag{2.21}$$

Substitution of the experimental data (see Eq. (2.12)) into Eq. (2.21) leads to

$$\begin{aligned} s^{e}(x) &= \mathbf{K^{+}(x)U\Lambda^{-1}U^{+}g^{e}} = \mathbf{K^{+}(x)U\Lambda^{-1}U^{+}(g+\epsilon)} \\ &= s(x) + \varepsilon(x), \end{aligned} \tag{2.22}$$

where $s^{e}(x)$ is the quantity of interest inverted from the experimental data g^{e}, and

$$\varepsilon(x) = \mathbf{K^{+}(x)U\Lambda^{-1}U^{+}}\epsilon. \tag{2.23}$$

Small eigenvalues have a large contribution in $\varepsilon(x)$ because of $\mathbf{\Lambda^{-1}}$. The errors are magnified by the small eigenvalues, which actually yields the terminology "error magnification."

2.5 Solution without Error Magnification

In this section, the solution without error magnification is discussed. We expresses $\{g_j\}$ in a form of expansion by the use of the orthonormal basis Eq. (2.19),

$$g_j = \sum_{l} U_{jl}\xi_l\lambda_l^{1/2}. \tag{2.24}$$

The expansion coefficient ξ_l correspond to small eigenvalue λ_l has little contribution to the quantity g_j. Therefore, it is not feasible to invert such ξ_l from $\{g_j\}$.

We construct a new orthonormal basis $\{\phi'_j(x)\}$ by discarding the small eigenvalues,

$$\phi'(\mathbf{x}) = \Lambda'^{1/2} U^+ \mathbf{K}(\mathbf{x}), \tag{2.25}$$

where Λ'_{ii} is Λ_{ii}^{-1} if $\Lambda_{ii} > \varsigma$, otherwise the element of $\mathbf{\Lambda}'$ is 0. ς is an arbitrary small constant. The choice of ς will be considered later. It is to be noted that the number of basis functions is less than the number of total kernels.

In the new basis $\{\phi'_j(x)\}$, the expansion coefficients of Eq. (2.16) and $s(x)$ become

$$\xi = \int_a^b \phi'(x) f(x) dx = \mathbf{\Lambda'^{1/2} U^+ g}, \tag{2.26}$$

$$s(x) = \phi^+(\mathbf{x})\xi = \mathbf{K}^+(\mathbf{x})\mathbf{U\Lambda' U^+ g}, \tag{2.27}$$

and the error in $s^e(x)$ becomes

$$\varepsilon(x) = \mathbf{K}^+(\mathbf{x})\mathbf{U\Lambda' U^+}\epsilon. \tag{2.28}$$

The errors is restricted by choosing a moderate ς in the inversion. The criterion for choosing ς is based on, first, the error magnitude as discussed in Section 2.3, and second, the comparison of a new set of data, which is obtained from Eq. (2.2) when $s^e(x)$ is substituted into $f(x)$, with the data $\{g_j\}$. A typical choice for the value of ς is 1 % of the maximum eigenvalues. This technique of discarding the small eigenvalues is in principle the same as that of discarding the zero eigenvalue in singular value decomposition (SVD). Therefore, above process of inversion is referenced as SVD method.

2.6 Program Description

In the numerical investigation a set of kernels is selected and the eigenvalues of the covariance matrix is evaluated to describe the interdependence of the kernels. The eigenvalues and the relative information are usually plotted versus the ordered number of the eigenvalue. The ordered number of the eigenvalue equals the particular eigenvalues' position in the eigenvalue array that is sorted in descending order. According to S. Twomey [5], the relative information $R_{inf}(n)$ is defined as

$$R_{inf}(n) = \frac{\sum_{i=1}^{n} \lambda_i}{\sum_{i=1}^{M} \lambda_i}. \tag{2.29}$$

The number of significant eigenvalues may be obtained by comparing the absolute eigenvalue with the error term $(|\sum_{j=1}^{M} a_j \epsilon_j|/f_m)^2$ or by the percentage of relative information. The graph of relative information is preferred in describing the degeneracy of kernels since it does not depend on the absolute values of eigenvalue and the error magnitude. A linear increase of relative information indicates that the kernels are independent while a saturation of relative information indicates the degeneracy of kernels.

The numerical results were obtained on Silicon Graphics machines (Power Challenge L and Origin 2000) by the use of a scientific mathematical library. This library, named "complib.sgimath", contains an extensive collection of industry standard libraries such as BLAS, EISPACK, LINPACK, and LAPACK. The following subroutines are used: DGEEV from LAPACK to compute eigenvalues and eigenvectors of

the covariance matrix; DGECO and DGEDI from LINPACK to compute the inverse of a matrix; DGELSS from LAPACK to compute the minimum norm solution (or the inversion) to a real linear least-squares problem. DGELSS is a SVD method of inversion.

2.7 Analysis with Gaussian Kernels

A Gaussian kernel has a simple form and many kernels can be approximated by a Gaussian kernel. The discrete Gaussian kernel is assumed as

$$K_j(x) = \frac{1}{\pi^{1/4}}\sqrt{\frac{2}{\sigma}}e^{-(x-x_j)^2/\sigma^2}, \tag{2.30}$$

where σ is the line width of the Gaussian. The data range is limited from c to d and M is the number of data. The kernel is centered at x_j,

$$x_j = c + (j-1)\Delta, \tag{2.31}$$

where $\Delta = \frac{(d-c)}{(M-1)}$, j=1, 2, ..., M. These kernels are assumed to be applicable for spectroscopic measurements. The measured data are the convolution of Gaussian kernels with the function of interest. The integration is extended to $-\infty$ and ∞; contributions to the integral are negligible for points that are spectrally separated by more than 5 line-widths of the Gaussian kernel. The covariance matrix and the eigenvalues of the covariance matrix are computed subsequently.

Figure 2.1 shows the eigenvalue and relative information for different σ when the total number of kernels M, c and d are fixed at $M = 512$, $c = 305$ nm and $d = 325$ nm, respectively. The number of significant eigenvalues decreases as σ increases.

The number of significant eigenvalues are about 80, 40, 20 for σ=0.2 nm, 0.4 nm, 0.8 nm, respectively.

Figure 2.2 shows the eigenvalue and relative information for different number of total kernels when σ, c and d are fixed at σ= 0.1 nm, c = 305 nm and d = 325 nm, respectively. The relative information is close to a straight line for $M = 100$. The curve of relative information are almost same for M = 200, 300, 512. About 98% relative information is contained in the largest 150 eigenvalues, or equivalently, 150 eigenvalues are required to characterize this measurement.

Figure 2.3 shows the eigenvalue and relative information for different number of total kernels when σ and Δ are fixed at $\sigma = 0.1$ and $\Delta = 0.039$. The number of significant eigenvalues is almost proportional to M.

There is an optimum interval for an experimental arrangement, which is related to the parameter σ. A different, narrower interval would not yield more information than the optimum interval. The following relation is found between the optimum interval Δ and σ,

$$\Delta \sim 1.33\sigma. \tag{2.32}$$

One can obtain all of the information by collecting data at an interval 1.3σ. The number of significant data for Gaussian kernels is approximately proportional to the range and the inverse of the width of the Gaussian kernel.

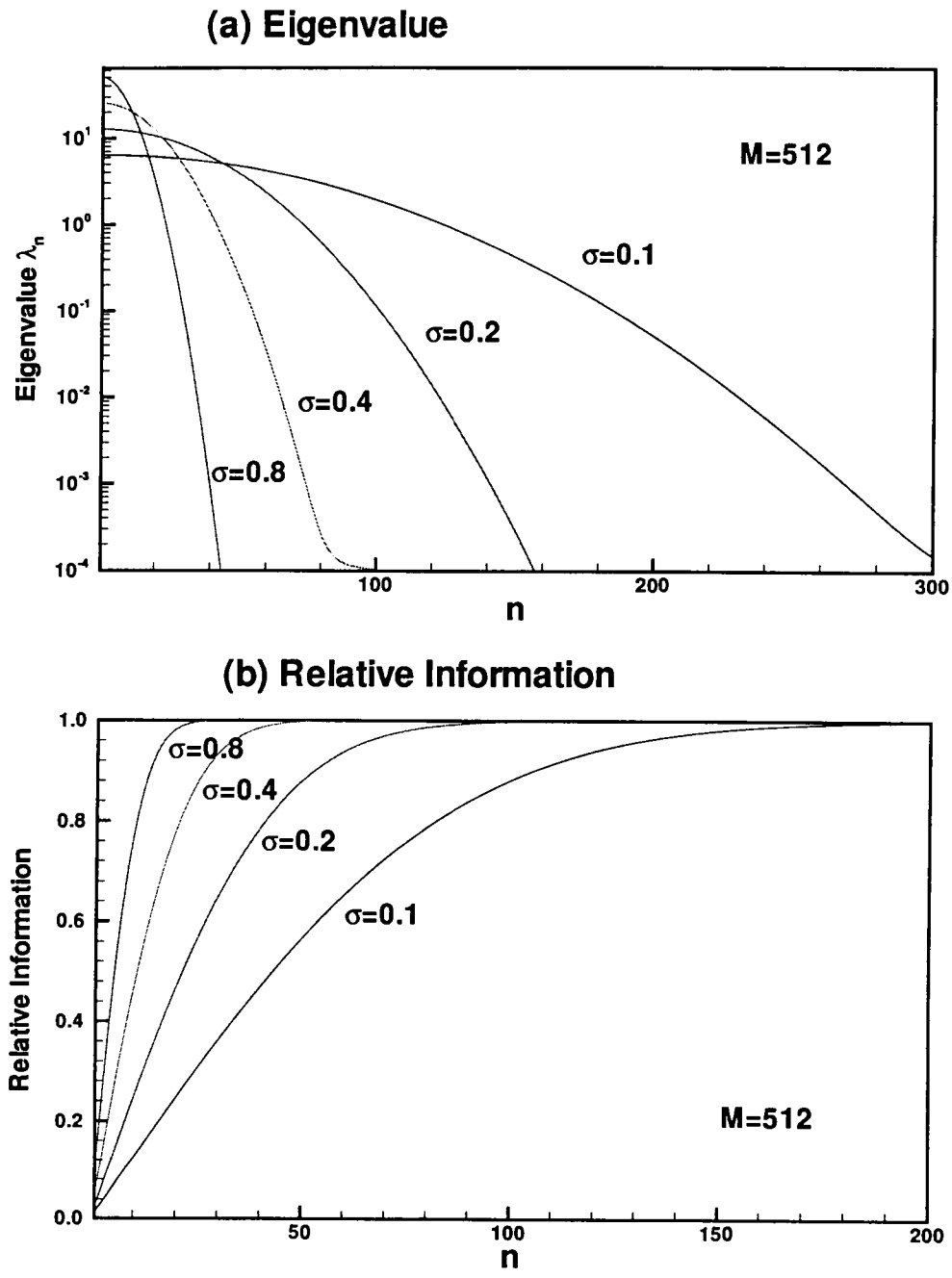

Figure 2.1: Eigenvalues and relative information for Gaussian kernels (I): fixed range c=305 nm and d=325 nm and fixed interval $\Delta = 0.039$ nm.

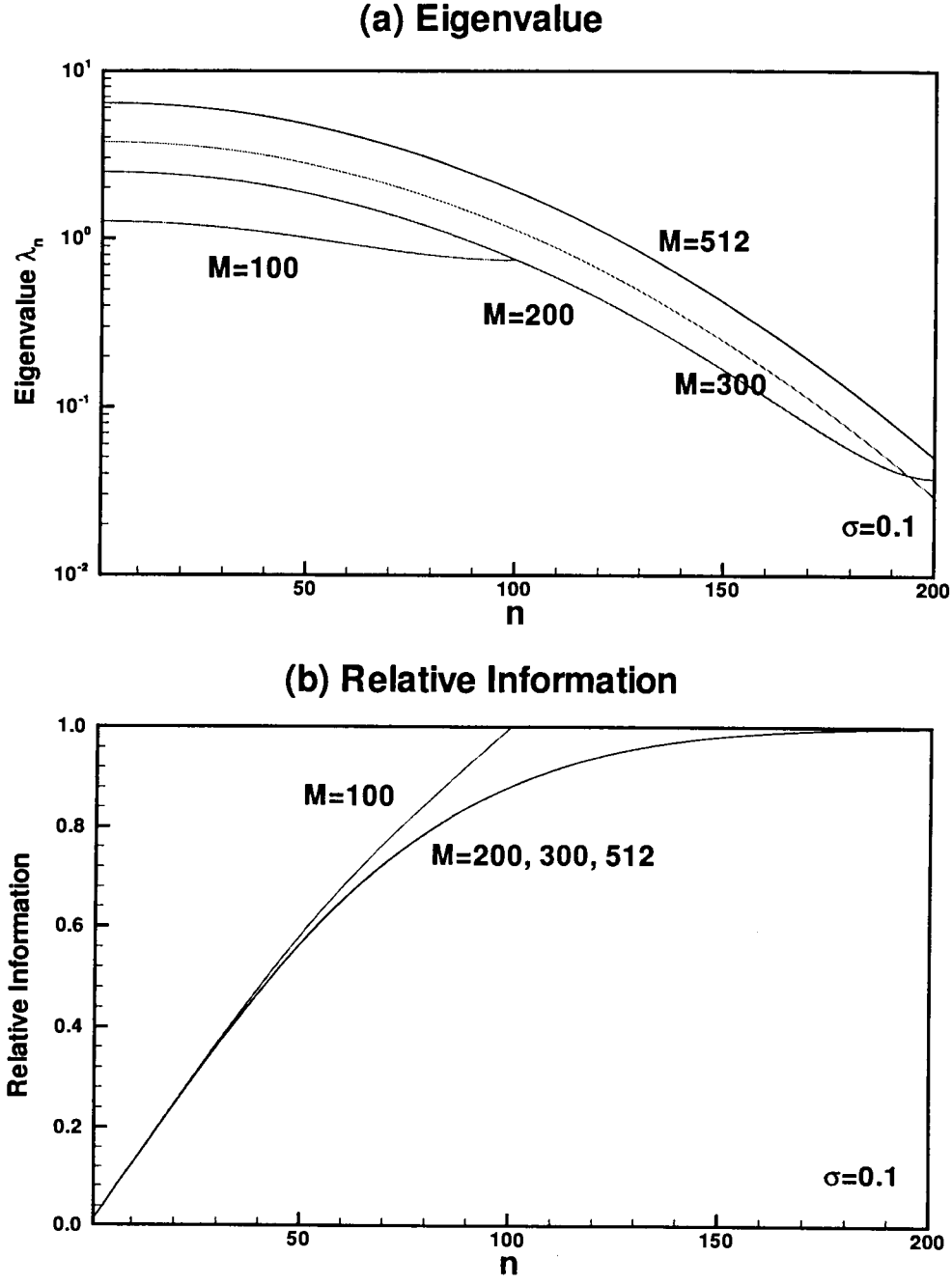

Figure 2.2: Eigenvalues and relative information for Gaussian kernels (II): fixed Gaussian line width $\sigma = 0.1$ nm and fixed range c=305 nm and d=325 nm.

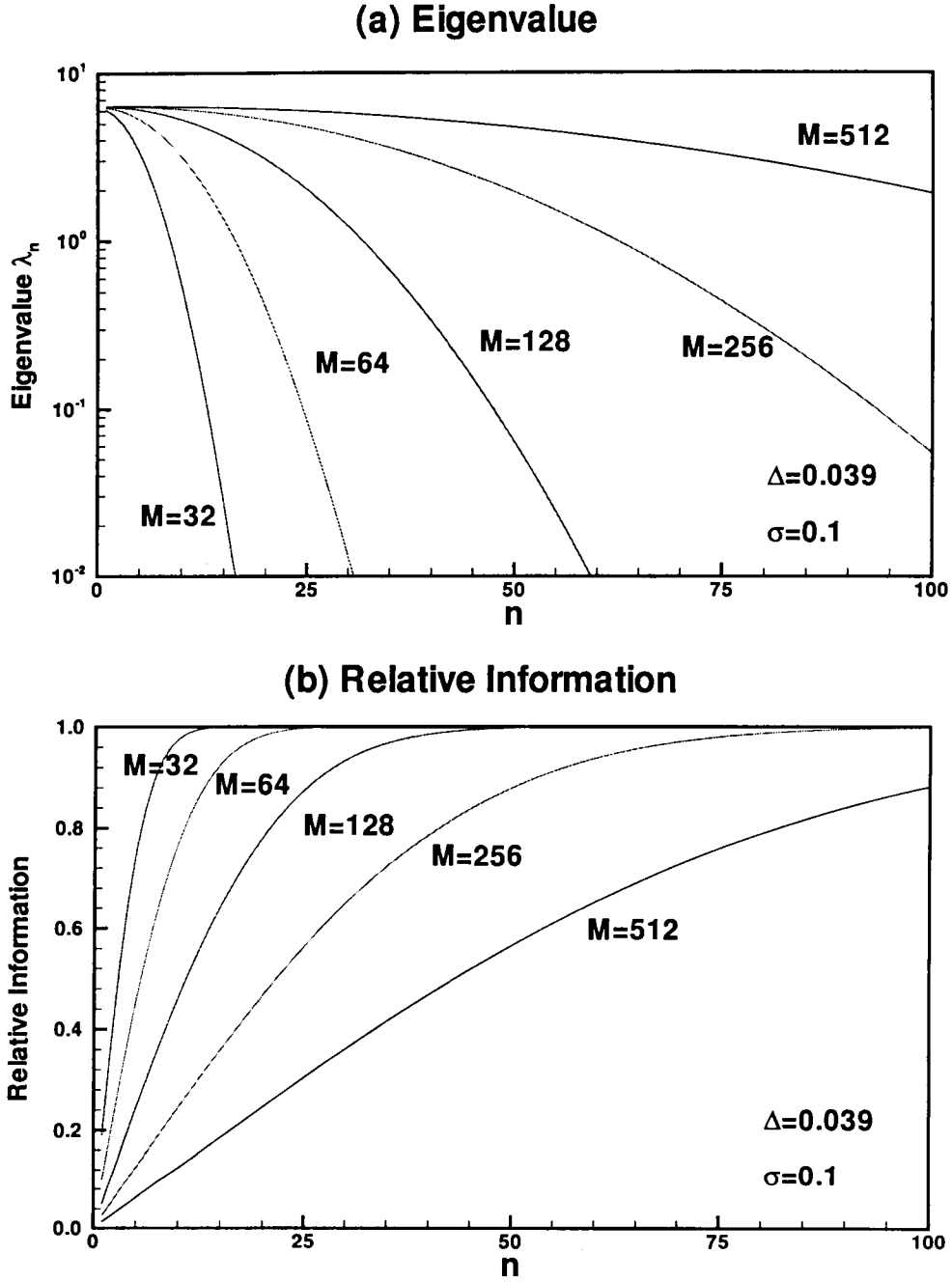

Figure 2.3: Eigenvalues and relative information for Gaussian kernels (III): fixed Gaussian line width $\sigma = 0.1$ nm and fixed interval $\Delta = 0.039$ nm.

Chapter 3

Data Analysis Techniques

3.1 Introduction

In this Chapter techniques of data analyses are presented. For the process of data analysis one usually assumes a model for the measured data. A set of physical quantities can be obtained by fitting measured data with the assumed model. The method of least-square fitting (LSF) is widely applied in data fitting. There are many discussions about least-square fitting as indicated by a short list of references [1, 2, 34, 35]. According to the data model, LSF may be categorized as linear least-square fitting (L-LSF) and nonlinear least-square fitting (NL-LSF). The error analysis for L-LSF is direct as is discussed, for example, in the book of P. R. Bevington and D. K. Robinson [2]. The error analysis for NL-LSF is complicated and may be accomplished in the parabolic approximation [26]. However, the error analysis can be accomplished in general by resorting to numerical methods. Monte Carlo simulations are used in the error analysis. The mean value, the variance and correlation of physical quantities of interest can be obtained by the use of Monte Carlo simulations.

The least-square fitting and the error propagation is investigated for simple,

model sets of data. These model sets of data depend exponentially on the parameter of interest. The emphasis of this study is on the evaluation of the error propagation and of the correlation between the fitting parameters.

3.2 Formulation of Least-square Fitting

The starting point is the supposition that y_j are the measured values of a physical quantity described by $g(\mathbf{x}_j, u, v, ...)$ at point $\mathbf{x_j}$ where $j = 1, 2, ..., M$, and $\{u, v, ...\}$ are the parameters. The normalized residuals are defined by

$$r_j = \frac{y_j - g(\mathbf{x}_j, u, v, ...)}{\sigma_j}, \tag{3.1}$$

where σ_j is the variance of y_j at position $\mathbf{x}_j$. The merit function for LSF is traditionally defined as

$$\chi^2(u, v, ...) = \sum_{j=1}^{M} w_j r_j^2 = \sum_{j=1}^{M} w_j (\frac{y_j - g(\mathbf{x}_j, u, v, ...)}{\sigma_j})^2, \tag{3.2}$$

where w_j is the weight at each data point. The numerical solution of parameters is determined by minimizing the merit function. It is named as linear least-square fitting if g is linearly dependent on $\{u, v, ...\}$ only. Otherwise, it is called nonlinear least-square fitting.

The development of the dependence of χ^2 on the independent parameters is accomplished by expanding the merit function χ^2 near its minimum described by the parameter set $\{u_0, v_0, ...\}$ as follows, [1, 2, 35]

$$\chi^2(u, v, ...) = \chi^2(u_0, v_0, ...) + (u - u_0)\frac{\partial \chi^2}{\partial u} + (v - v_0)\frac{\partial \chi^2}{\partial v} + ...$$

$$+\frac{1}{2}(u-u_0)^2\frac{\partial^2\chi^2}{\partial u^2}+\frac{1}{2}(v-v_0)^2\frac{\partial^2\chi^2}{\partial v^2}+(u-u_0)(v-v_0)\frac{\partial^2\chi^2}{\partial u\partial v}+...$$

$$= \chi^2(u_0,v_0,...)-2(u-u_0)\beta_u-2(v-v_0)\beta_v+...$$

$$+(u-u_0)^2\alpha_{uu}+(v-v_0)^2\alpha_{vv}+2(u-u_0)(v-v_0)\alpha_{uv}+..., \qquad (3.3)$$

where,

$$\beta_\mu = -\frac{1}{2}\frac{\partial\chi^2}{\partial\mu}$$

$$= \sum_{j=1}^{M} w_j\frac{y_j-g(\mathbf{x}_j,u_0,v_0,...)}{\sigma_j^2}\left(\frac{\partial g(\mathbf{x}_j,u,v,...)}{\partial\mu}\right)_{u=u_0,v=v_0,...}, \qquad (3.4)$$

$$\alpha_{\mu\nu} = \frac{1}{2}\frac{\partial\chi^2}{\partial\mu\partial\nu}$$

$$= \sum_{j=1}^{M}\frac{w_j}{\sigma_j^2}\left[\left(\frac{\partial g(\mathbf{x}_j,u,v,...)}{\partial\mu}\right)_{u=u_0,v=v_0,...}\left(\frac{\partial g(\mathbf{x}_j,u,v,...)}{\partial\nu}\right)_{u=u_0,v=v_0,...}\right.$$

$$\left.-(y_j-g(\mathbf{x}_j,u,v,...))\left(\frac{\partial^2 g(\mathbf{x}_j,u,v,...)}{\partial\mu\partial\nu}\right)_{u=u_0,v=v_0,...}\right]. \qquad (3.5)$$

The indices μ,ν may be any of $\{u,v,...\}$. β_μ should be zero at the minimum of χ^2 if $g(\mathbf{x}_j,u,v,...)$ is a smooth function. In the work of this dissertation Powell's method [36] is used to find the minimum of the merit function.

Now we introduce the parabolic approximation in which higher order terms are omitted. The parabolic approximation is always valid for linear least-square fitting because the differentiation to g with order higher than one is zero. However, the parabolic approximation is often violated in the process of nonlinear least-square fitting. In the parabolic approximation, one obtains:

$$\Delta\chi^2 = \chi^2(u,v,...)-\chi^2(u_0,v_0,...)$$

$$= \sum_{\mu\nu}(\mu-\mu_0)(\nu-\nu_0)\alpha_{\mu\nu} \qquad (3.6)$$

The correlation coefficients [1, 2, 35] between parameters are also important. The definition of the correlation coefficient for the parameters u and v, ρ_{uv}, is deferred to Appendix D. By comparing Eq. (3.6) and Eq. (D.4), one finds

$$\rho_{uv} = -\frac{\alpha_{uv}}{(\alpha_{uu}\alpha_{vv})^{1/2}}. \tag{3.7}$$

Note that the obtained correlation coefficient is only defined for different parameters u and v.

3.3 General Error Analysis

In this section the error propagation equations are presented. The derivation of the error propagation equations is in accord with the references [1, 2]. One assumes that a quantity z is determined by variables $\{u, v, ...\}$ as a function $f(u, v, ...)$, i.e., a set of measured data $\{u_i, v_i, ...\}$ yields a value z_i,

$$z_i = f(u_i, v_i, ...). \tag{3.8}$$

The averages and variances of $\{u, v, ...\}$ are determined from collection sets of measured data $\{u_i, v_i, ...\}$. The average and variance of z may be determined from those of $\{u, v, ...\}$. To obtain the relation, one expresses z_i by the use of the Taylor expansion of $f(u_i, v_i, ...)$ around the average $\bar{u}, \bar{v}, ...$,

$$\begin{aligned} z_i &= f(\bar{u}, \bar{v}, ...) + (u_i - \bar{u})\frac{\partial f}{\partial u} + (v_i - \bar{v})\frac{\partial f}{\partial v} + ... \\ &+ \frac{1}{2}(u_i - \bar{u})^2\frac{\partial^2 f}{\partial u^2} + \frac{1}{2}(v_i - \bar{v})^2\frac{\partial^2 f}{\partial v^2} + (u_i - \bar{u})(v_i - \bar{v})\frac{\partial f}{\partial u}\frac{\partial f}{\partial v} + ... \end{aligned} \tag{3.9}$$

Then the average and the variance of z are:

$$\begin{aligned}
\bar{z} &= \frac{1}{N}\sum_i z_i \\
&= f(\bar{u},\bar{v},...) + \frac{1}{2}\sigma_u^2\frac{\partial^2 f}{\partial u^2} + \frac{1}{2}\sigma_v^2\frac{\partial^2 f}{\partial v^2} + ... + \sigma_{uv}^2\frac{\partial f}{\partial u}\frac{\partial f}{\partial v} + ..., \qquad (3.10) \\
\sigma_z^2 &= \frac{1}{N}\sum_i (z_i - \bar{z})^2 \\
&= \sigma_u^2(\frac{\partial f}{\partial u})^2 + \sigma_v^2(\frac{\partial f}{\partial v})^2 + ... + 2\sigma_{uv}^2\frac{\partial f}{\partial u}\frac{\partial f}{\partial v} + ..., \qquad (3.11)
\end{aligned}$$

where the covariance σ_{uv}^2 is given by

$$\sigma_{uv}^2 = \frac{1}{N}\sum_i (u_i - \bar{u})(v_i - \bar{v}). \qquad (3.12)$$

The covariance vanishes, i.e., $\sigma_{uv} = 0$, on the average of u and v if u and v is not correlated.

The uncertainty of the fitting parameters in least-square method can be evaluated with the error propagation equations. For this evaluation one considers a parameter μ, which could be any of $\{u, v, ...\}$, as a function of the measured data set $\{y_j\}$. The dependence of this general parameter μ on the set $\{y_j\}$ originates from the data fitting. By the use of the error propagation equations, one finds for the uncertainty of the parameter μ,

$$\sigma_\mu^2 = \sum_{ij}\sigma_{ij}^2\frac{\partial \mu}{\partial y_i}\frac{\partial \mu}{\partial y_j} + ..., \qquad (3.13)$$

where the covariance σ_{ij} has been previously defined. The covariance σ_{jj}^2 is usually denoted as σ_j^2.

The covariance of different data is zero if the errors for different data are not correlated. When omitting the contributions from the higher order the uncertainty

reduces to the following expression for the variance of the parameter μ,

$$\sigma_\mu^2 = \sum_{j=1}^{M} \sigma_j^2 (\frac{\partial \mu}{\partial y_j})^2. \tag{3.14}$$

It is in general difficult to determine $\frac{\partial \mu}{\partial y_j}$ for nonlinear least-square fitting without introducing further assumptions or dependencies of μ on the set of data. K. H. Burrell [26] published an error propagation equation in the parabolic approximation for equal weights $\{w_j\}$, i.e., all weights are set to 1. For different weights, the error propagation equation in the parabolic approximation is obtained as the following,

$$\sigma_\nu^2 = \sum_{j=1}^{M} (\sum_{\mu} \frac{w_j}{\sigma_j} \theta_{\mu\nu} \frac{\partial g(\mathbf{x}_j, u, v, ...)}{\partial \mu})^2. \tag{3.15}$$

The matrix $(\theta_{\mu\nu})$ is the inverse matrix of the matrix $(\alpha_{\mu\nu})$ defined in Eq. (3.5) and the parameters μ, ν could represent any parameters of the set $\{u, v, ...\}$.

3.4 Error Propagation for One Parameter Fitting

In this section the error propagation for one-parameter fitting is discussed. The function $g(x_j, U)$ denotes the model-function for the data set $\{y_j\}$. The parameter U is obtained by fitting $g(x_j, U)$ with $\{y_j\}$. The merit function is the same as Eq. (3.2) but it is restated here for the one-parameter case,

$$\chi^2 = \sum_{j=1}^{M} \frac{w_j}{\sigma_j^2} [y_j - g(x_j, U)]^2. \tag{3.16}$$

There exists only one element in the matrix α. Therefore, Eq. (3.5) reduces to the following expression,

$$\alpha = \sum_{j=1}^{M} \frac{w_j}{\sigma_j^2} [(\frac{\partial g(x_j, U)}{\partial U})^2 - (y_j - g(x_j, U)) \frac{\partial^2 g(x_j, U)}{\partial U^2}], \tag{3.17}$$

and one finds for the uncertainty or variance of U,

$$\sigma_U^2 = \sum_{j=1}^{M} (\frac{w_j}{\alpha \sigma_j} \frac{\partial g(\mathbf{x}_j, U)}{\partial U})^2. \tag{3.18}$$

This is the error propagation equation for one parameter fitting.

3.5 Monte Carlo Simulation Method

Monte Carlo simulations provide us with the numerical solution to the probability distribution problem. The procedure is to "draw random numbers from appropriate distribution so as to mimic our best understanding of the underlying process and measurement errors in our apparatus" [36]. A set of synthetic data is generated by the use of random numbers. The quantities of interest are determined by fitting the synthetic data. Typically, probability distributions for the quantities will be obtained.

The Gaussian probability distribution is used as the error probability distribution in our investigation,

$$P(x; x_0, \sigma_x) = \frac{1}{\sqrt{2\pi}\sigma_x} exp[-\frac{1}{2}(\frac{x - x_0}{\sigma_x})^2]. \tag{3.19}$$

The random numbers are generated by the subroutine CLARNV which is in the mathematical library "complib.sgimath". Figure 3.1 shows the distribution of N random numbers that were generated with this CLARNV subroutine. The solid curve illustrates the Gaussian distribution function for $x_0 = 0$ and $\sigma_x = 1$. The average and variance of the random number is also shown in Fig. 3.1. The histogram

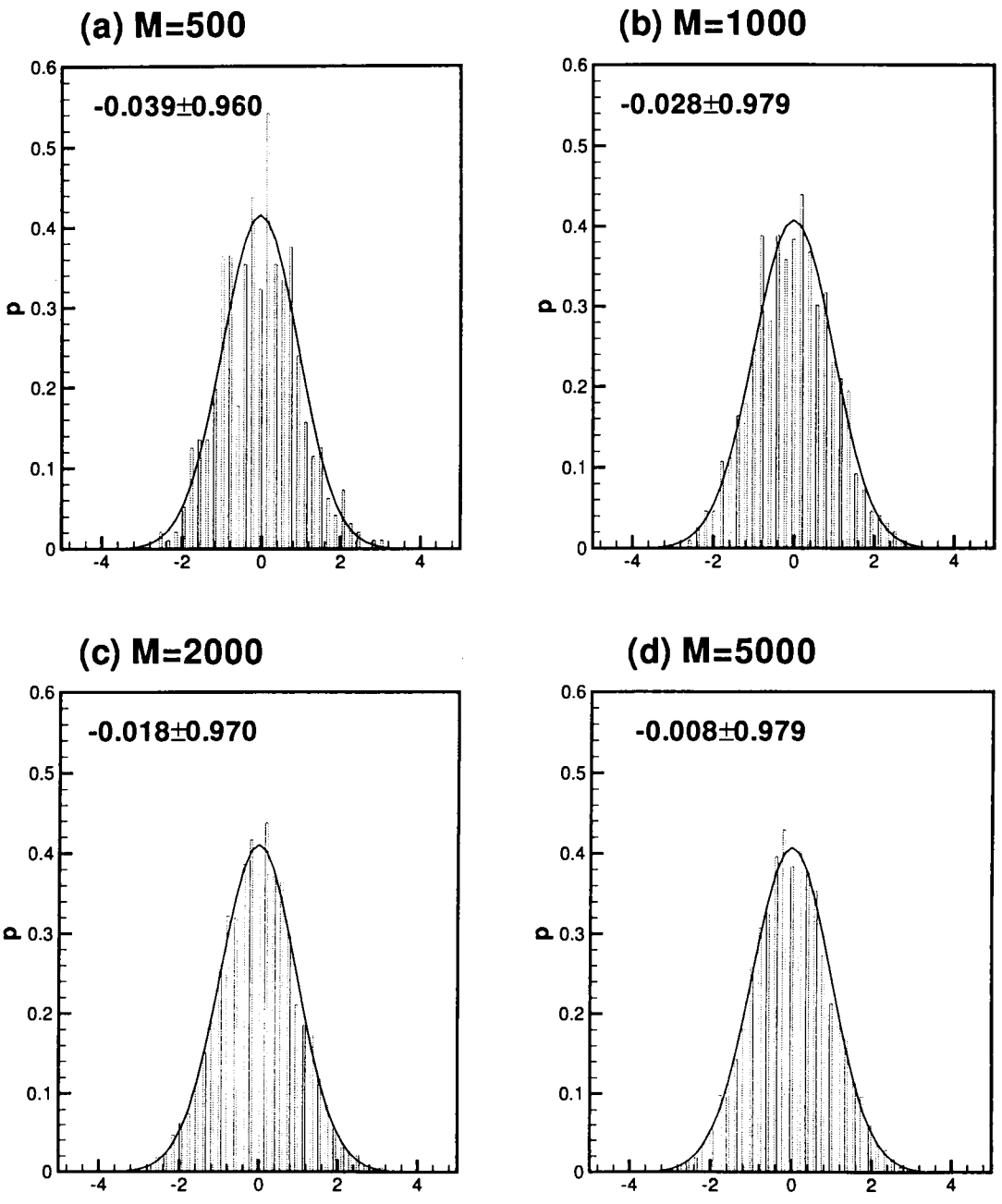

Figure 3.1: Distribution of the generated random numbers.

distributions of random numbers appears visually very close to the smooth Gaussian distribution for N over 1000.

3.6 Numerical Investigations of Simple Models

In this section sets of data models with an exponential parameter dependency are investigated. These models can be viewed as simulations for spectroscopic data. Individual terms of the model function can be associated with spectral lines: each term consists of amplitude and line profile. The amplitude is related to temperature by the usual Boltzmann factor $e^{-\epsilon/kT}$ in equilibrium, where ϵ is the relative upper energy and k is Boltzmann constant. For simplicity in the description, $e^{-\gamma U}$ is used in favor of $e^{-\epsilon/kT}$ where γ is a constant that is proportional to the ϵ/k term. The investigations are performed by the use of Monte Carlo simulations. In addition, the results from the simulations are compared with analytic results.

In the investigation with Monte Carlo simulations, we use the following simple models:

$$g(x,U) = 0.89\, e^{-\gamma U} e^{-(x-310.)^2/0.05}, \tag{3.20}$$

$$g(x,U) = 0.89\, e^{-U} e^{-(x-310.)^2/0.05} + 0.89\, e^{-2U} e^{-(x-315.)^2/0.05}. \tag{3.21}$$

Equation (3.20) represents one spectral line that is associated with a spectral transition. Equation (3.21) represents two well separated spectral lines describing two transitions from two different upper energy levels, for which the parameter γ is 1 and 2, respectively.

The numerical investigation is described in the following. One assumes a set of the measured data $\{y_j\}$ determined by

$$y_j = g(x_j, U), \tag{3.22}$$

where $x_j = c+(j-1)\Delta$ and $\Delta = \dfrac{(d-c)}{(M-1)}$, $j = 1, 2, ..., M$. Alternate assumptions are discussed later in this section. One further assumes that four hundred wavelength-dependent data (i.e., M=400) are recorded from $c = 305$ nm to $d = 325$ nm.

The inclusion of the random numbers results in a variation of data y_j: a random number R_j is added according to

$$y'_j = y_j + R_j, \tag{3.23}$$

where the random number R_j is further specified depending on the error model. Two typical error models are considered. The first error model uses

$$R_j = 0.1 * y_j * R(), \tag{3.24}$$

while the second error model uses

$$R_j = 0.1 * y_{max} * R(), \tag{3.25}$$

where y_{max} denotes the maximum of the set $\{y_j\}$ and R() denotes a generator function of random number, for which the subroutine CLARNV described in previous section is used. The random number is proportional to data value y_j for the first error model. The random number is independent on the data y_j for the second error model. Therefore the variances of data y_j are

$$\sigma_j \;=\; 0.1 * y_j, \tag{3.26}$$

and

$$\sigma_j = 0.1 * y_{max}, \tag{3.27}$$

respectively.

The parameter U is found by fitting the data $\{y'_j\}$ with $g(x_j, U)$. The technique of nonlinear least-square fitting is applied in data fitting. The distribution of quantity U is obtained after repeating the process many times - vary $\{y_j\}$ and fit. The weights w_j may be assumed as a constant or dependent on y_j or dependent on σ_j. The actual choice of weights will depend on our knowledge of a particular data set, for example, knowledge regarding the acquisition method.

The analytic formulation is summarized below. By substituting α in Eq. (3.17) into the error propagation equation of Eq. (3.18), the variance of quantity U is obtained,

$$\sigma_U^2 = \sum_{j=1}^{M} (\frac{w_j}{\sigma_j} \frac{\partial g(x_j, U)}{\partial U})^2 / [\sum_{j=1}^{M} \frac{w_j}{\sigma_j^2} (\frac{\partial g(x_j, U)}{\partial U})^2]^2, \tag{3.28}$$

where the second term of α is close to zero for the used data model. Now we substitute $g(x_j, U)$ with the one-line model function. The variance of U for the one-line model is the following value if w_j is assumed to be equal to 1 and σ_j is assumed to be proportional to y_j as indicated in Eq. (3.26),

$$\sigma_U^2 = 1 / \sum_{j=1}^{M} \frac{1}{\sigma_j^2} (\frac{\partial g(x_j, U)}{\partial U})^2 = \frac{1}{M} (\frac{0.1}{\gamma})^2. \tag{3.29}$$

The variance of quantity U for the one-line model is the following value if w_j is

assumed to be equal to σ_j^2 and σ_j is proportional to y_j as indicated in Eq. (3.26),

$$\begin{aligned}\sigma_U^2 &= \sum_{j=1}^{M}(\sigma_j\frac{\partial g(x_j,U)}{\partial U})^2/[\sum_{j=1}^{M}(\frac{\partial g(x_j,U)}{\partial U})^2]^2 \\ &= \frac{0.01}{\gamma^2}\sum_{j=1}^{M}g^4(x_j,U)/(\sum_{j=1}^{M}g^2(x_j,U))^2. \end{aligned} \tag{3.30}$$

By substituting the values of $g(x_j,U)$ into the above equation and summing over all 400 data, the variance of U becomes

$$\sigma_U^2 = (\frac{0.036}{\gamma})^2. \tag{3.31}$$

The numerical results are summarized in next several paragraphs. In all numerical computations the weight for each data is assumed equal to σ_j^2. Therefore, the merit function becomes

$$\chi^2(u,v,...) = \sum_{j=1}^{M}(y_j - g(\mathbf{x}_j,u,v,...))^2. \tag{3.32}$$

The one-spectral-line model is investigated for different values of γ and compared with the analytical result Eq. (3.31). The first error model Eq. (3.24) is used in generating random errors. The variances of quantity U with different γ is listed in table 3.1. The numerical results agree very well with the analytical result Eq. (3.31). It is shown that larger γ produce less error, i.e., that high energy levels are more accurate in determining the temperature. Figure 3.2(a) shows curve y_j in black, a

Table 3.1: Variance of quantity U versus γ.

γ	0.2	0.3	0.6	1	2
σ_U	0.181	0.120	0.059	0.036	0.018
$\gamma\sigma_U$	0.036	0.036	0.035	0.036	0.036

set of variation y'_j in red, and their differences in blue with γ =1. Figure 3.2(b) shows bar chart of probability distribution of U from the Monte Carlo simulations with γ =1. Similarly, the variance of quantity U for the data model of two-separate-line (see Eq. (3.21)) is found to be 0.016 from Monte Carlo simulations.

In the following, the spectroscopic data models are modified to include background contribution. The two-separate-line model is investigated only. The data is fitted with model $Ag(x_j, U) + B$. Here, A is a constant factor and B is the background.

Two types of data are used. The first type of data set $\{y_j\}$ is determined by the following form,

$$y_j = g(x_j, U) + 0.05, \tag{3.33}$$

where $g(x, U)$ is described by Eq. (3.21). We refer to this type of data as the "simple" two-separate-line model. The variation technique described by Eq. (3.23) and Eq. (3.24) (first error model) is applied to $\{y_j\}$ to generate new data sets $\{y'_j\}$. A set of parameters (U, A, B) is then determined by fitting each variation set $\{y'_j\}$ with $Ag(x_j, U) + B$. A distribution of (U, A, B) is obtained through this process of Monte Carlo simulations. The average and variance of U, A and B are shown in table 3.2. Note the variance of U is more than 3 times larger than the value 0.016 when including A and B. The correlation coefficients are shown in table 3.3 . Parameters U and A have strong correlation while U has almost no correlation with B.

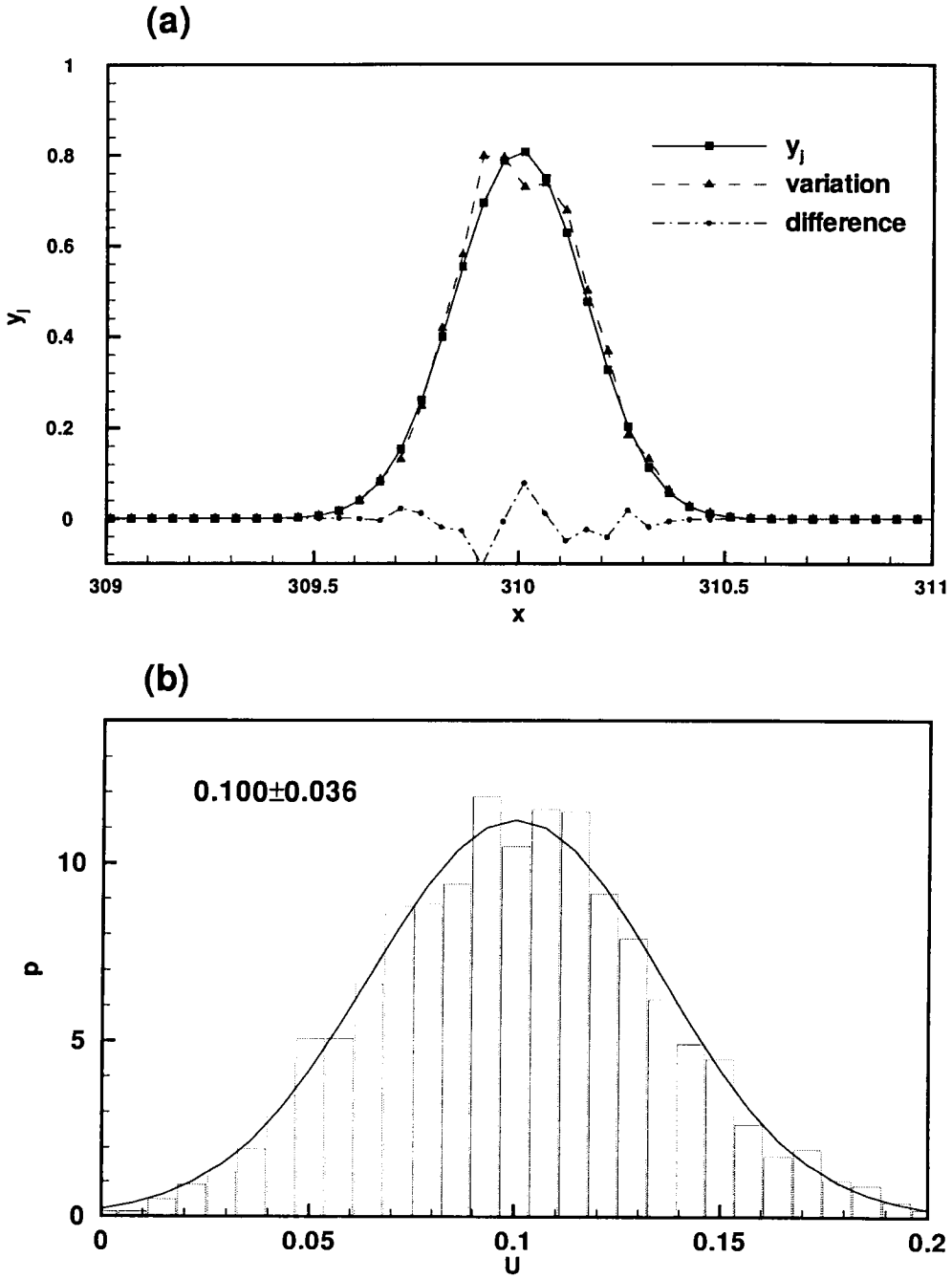

Figure 3.2: Monte Carlo simulation results for the one-spectral-line model: (a) y_j and its variation; (b) the probability distribution of quantity U from the Monte Carlo simulations.

Table 3.2: Average and variance of parameters for the "simple" model.

	U	A	B
Average	0.101	1.005	0.0500
Variance	0.054	0.086	0.0004

Table 3.3: Correlation coefficients for the "simple" model.

	U	A	B
U		0.95	-0.03
A	0.95		-0.18
B	-0.03	-0.18	

The second type of data set $\{y_j\}$ is determined as follows,

$$y_j = e^{-U}\theta(\frac{x_j - 310.}{0.5}) + e^{-2U}\theta(\frac{x_j - 315.}{0.5}) + 0.3, \tag{3.34}$$

where the line profile $\theta(x)$ is a triangle function:

$$\theta(x) = 1 - |x| \qquad |x| \leq 1; \qquad 0 \qquad |x| > 1. \tag{3.35}$$

This type of data set is labelled the "triangle" two-separate-line model. The variation technique described by Eq. (3.23) and Eq. (3.25) (second error model) is applied to $\{y_j\}$ to generate a new data set $\{y'_j\}$. Each variation set $\{y'_j\}$ is fitted with $Ag(x_j, U) + B$ where $g(x, U)$ is

$$g(x, U) \;=\; e^{-U}e^{-(x - 310.)^2/D^2} + e^{-2U}e^{-(x - 315.)^2/D^2}. \tag{3.36}$$

A new variable D is introduced to investigate on the different line profiles. A set of parameters (U, A, B, D) is determined by the data fitting. A distribution of (U, A, B, D) is obtained from Monte Carlo simulations. The average and variance of U,

Table 3.4: Average and variance of parameters for the "triangle" model.

	U	A	B	D
Average	0.102	0.642	0.299	0.313
Variance	0.053	0.051	0.005	0.012

Table 3.5: Correlation coefficients for the "triangle" model.

	U	A	B	D
U		0.93	0.05	0.03
A	0.93		-0.06	0.05
B	0.05	-0.06		-0.23
D	0.03	0.05	-0.23	

A, B and D are shown in table 3.4. The correlation coefficients are shown in table 3.5. Parameters U and A have strong correlation while U has almost no correlation with B and D.

Figure 3.3 shows the two types of data set $\{y_j\}$, typical variation set $\{y'_j\}$ and their differences for (a) "simple" model and (b) "triangle" model. Figure 3.4 displays the scatter plots for (U, A) and (U, B) from Monte Carlo simulations for the "simple" model. The averages, variances and correlations of parameters U, A and B are also shown in Fig. 3.4. Figure 3.5 displays the scatter plots for (U, A), (U, B) and (U, D) from Monte Carlo simulations for the "triangle" model. Also the averages, variances and correlations of parameters U, A, B and D are shown in Fig. 3.5.

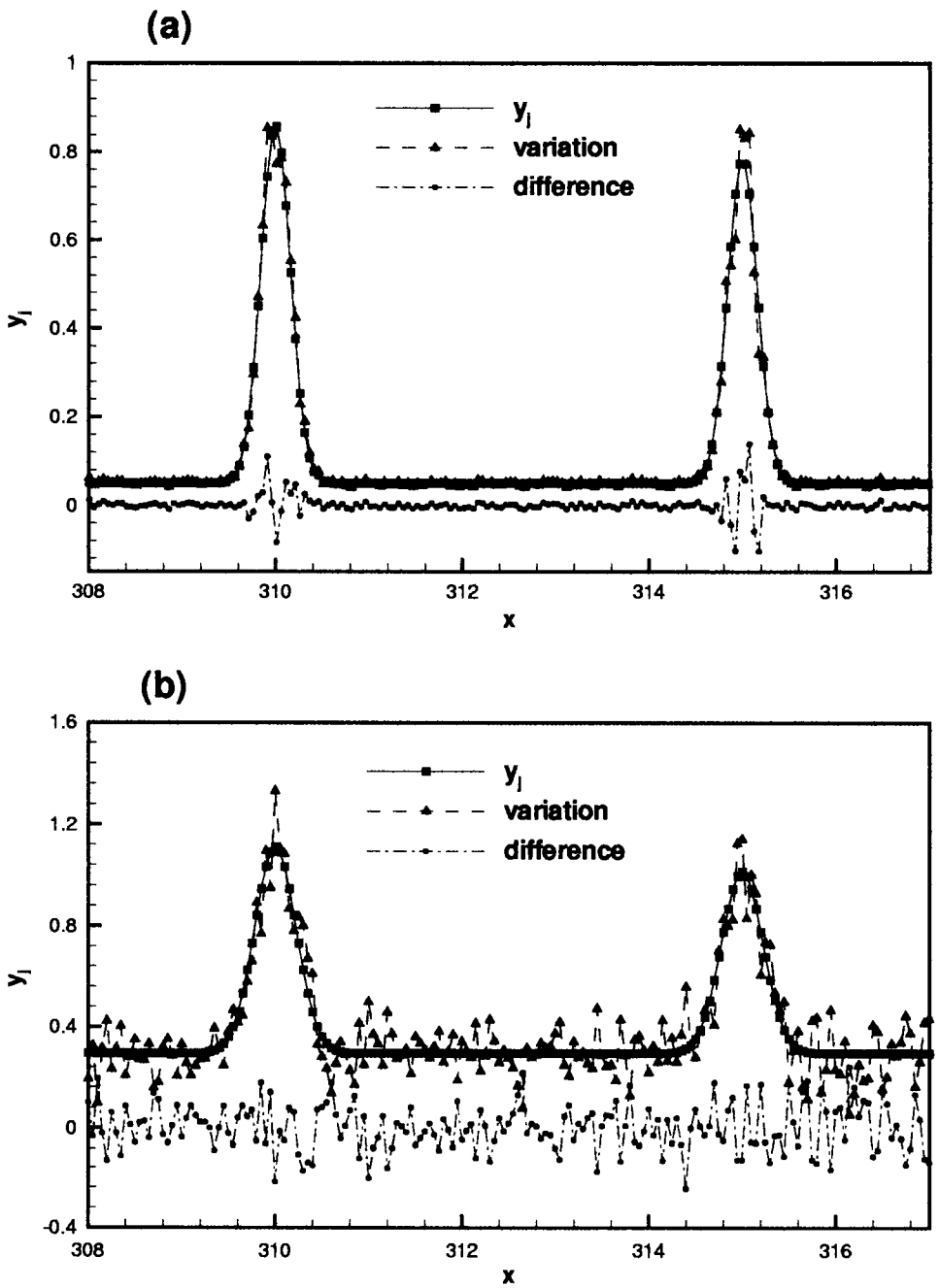

Figure 3.3: Data sets for the two-separate-line models: (a) "simple" model; (b) "triangle" model.

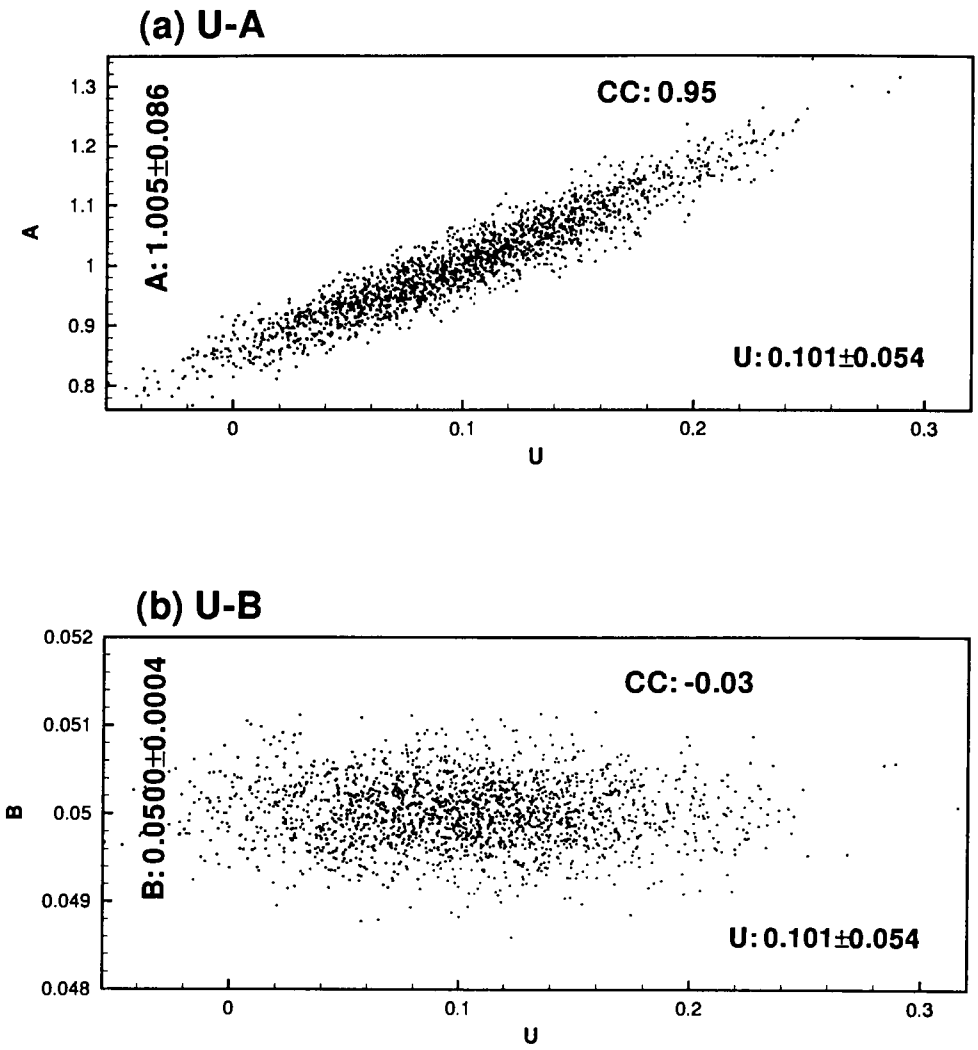

Figure 3.4: Scatter plots from Monte Carlo simulations for the "simple" model: (a) (U, A); (b) (U, B).

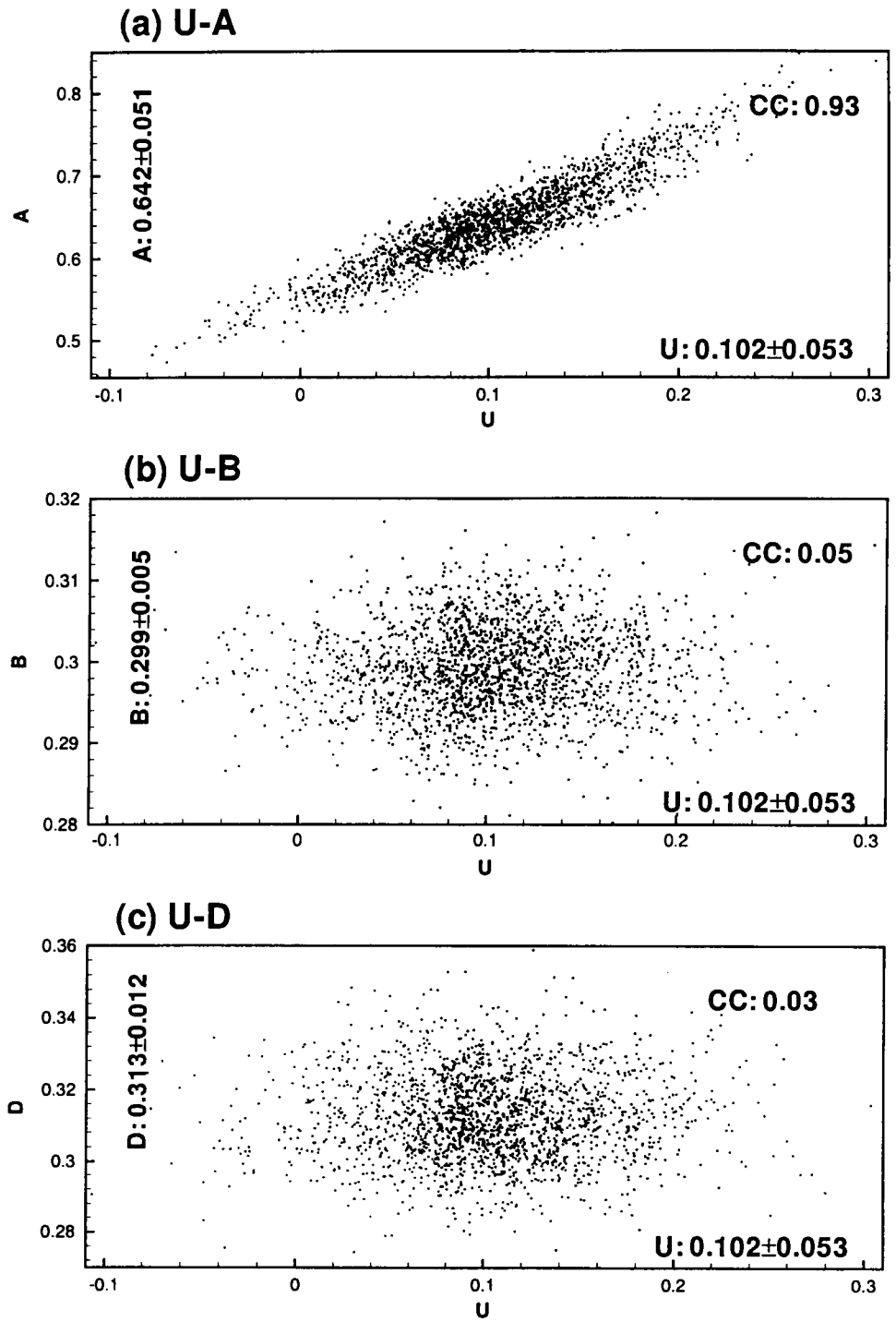

Figure 3.5: Scatter plots from Monte Carlo simulations for the "triangle" model: (a) (U, A); (b) (U, B); (c) (U, D).

Chapter 4

Analyses of Emission Spectra

4.1 Introduction

The emission spectra contain temperature information of the emission source. The determination of spectroscopic temperature comprises here the measurement of emission spectra and subsequent fitting of the experimental data. [24, 25, 37] The theoretical model of spectral data is critical in data fitting. Diatomic radicals are transiently present in a wide variety of reactive gas phase systems. Their emissions may dominate the emission spectra in some special ranges of wavelength and temperature. The spectral structures of such diatomic molecules can be predicted well from reported spectroscopic data. Therefore, the emission spectrum may be modeled as diatomic radical emissions plus a background contribution, which includes emissions from the other species.

In this Chapter the emission spectra of plasma after laser-induced breakdown of air [23] are studied in the wavelength range of 300 to 322 nm. An overview of the plasma emission spectra is computed by the use of the nonequilibrium air radiation code (NEQAIR). [27, 28] OH emission dominates the plasma emission spectra below

temperature 4500 K in this wavelength range of 305-322 nm. Above 4500 K N_2 Second Positive emissions become important; however, in this dissertation spectra are analyzed that show dominant OH contributions. The plasma emission spectra are fitted with synthetic OH spectra to determine the spectroscopic temperature. The temperature of fitting in the range 305-312 nm is more reliable than the temperature of fitting in the range 305-322 nm since the vibration states might not be in thermal equilibrium with the surrounding gases. The precision and reliability of this temperature measurement is also investigated. Monte Carlo simulations are used to study the error propagation. The variance of estimated temperature is nearly proportional to the error magnitude. The correlation coefficients are also evaluated by the use of Monte Carlo simulations. The background is found to be important in determining the temperature but the line shape is found to have hardly any relation with temperature.

4.2 Measurement of Laser-Induced Air Breakdown Spectra

The experimental data are provided by Drs C. Parigger and D. Plemmons. [23] The emission spectra were measured at different delay times after the laser-induced optical breakdown in nominal STP laboratory air. A Coherent Infinity 40-100 Nd:YAG laser was operated at a frequency of 10 or 100 Hz with 1064-nm radiation of 3.5-ns pulse width. The 1064-nm beam was focused with a typical peak intensity of $10^{13} W/cm^2$. The spectra were resolved with a 0.275-m Jarrel-Ash or a 0.64-m Jobin-

Yvon spectrometer and recorded with an array detector. Wavelength calibrations were performed with standard light sources and the sensitivity correction was accomplished with a deuterium lamp. The detector's data were corrected for dark-noise contribution.

4.3 Prediction of Spectroscopic Features

In this dissertation, the Nonequilibrium Air Radiation (NEQAIR) program [27, 28] is utilized to compute emission spectra of plasma. However, only the equilibrium aspects of the NEQAIR code were utilized. In the computation, the temperature and concentrations of the different species are required as the input of this version of the NEQAIR program. The concentrations of air components is calculated by using the Gordon-McBride chemical equilibrium code. [38] Figure 4.1 shows the temperature dependency of species number densities of wet air which contains approximately 1% water. Note that the OH concentration has a maximum around T = 3000 K.

Results from the NEQAIR computation are presented in the following. Figures 4.2 and 4.3 show synthetic emission spectra at different temperature. Input data are used as illustrated in Fig. 4.1. For the curves indicated as "Total", the OH number densities are extracted from Fig. 4.1. For the curves indicated as "Background", the OH number densities are set to zero. We label the emission without OH the "background emission" since it is the emission from species other than OH. Both total emissions and background emissions increase dramatically from 3000 K to 3500 K. The total emissions decrease over 4000 K because the concentration of OH decreases

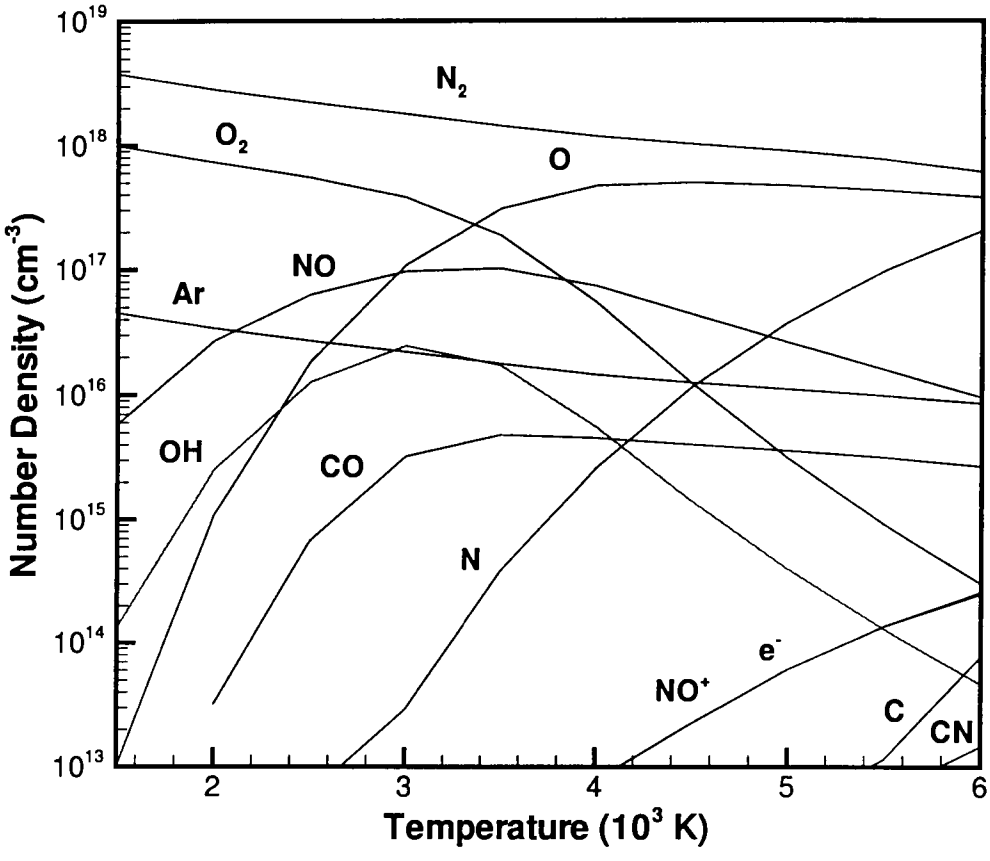

Figure 4.1: Number density of air species concentrations at different temperature.

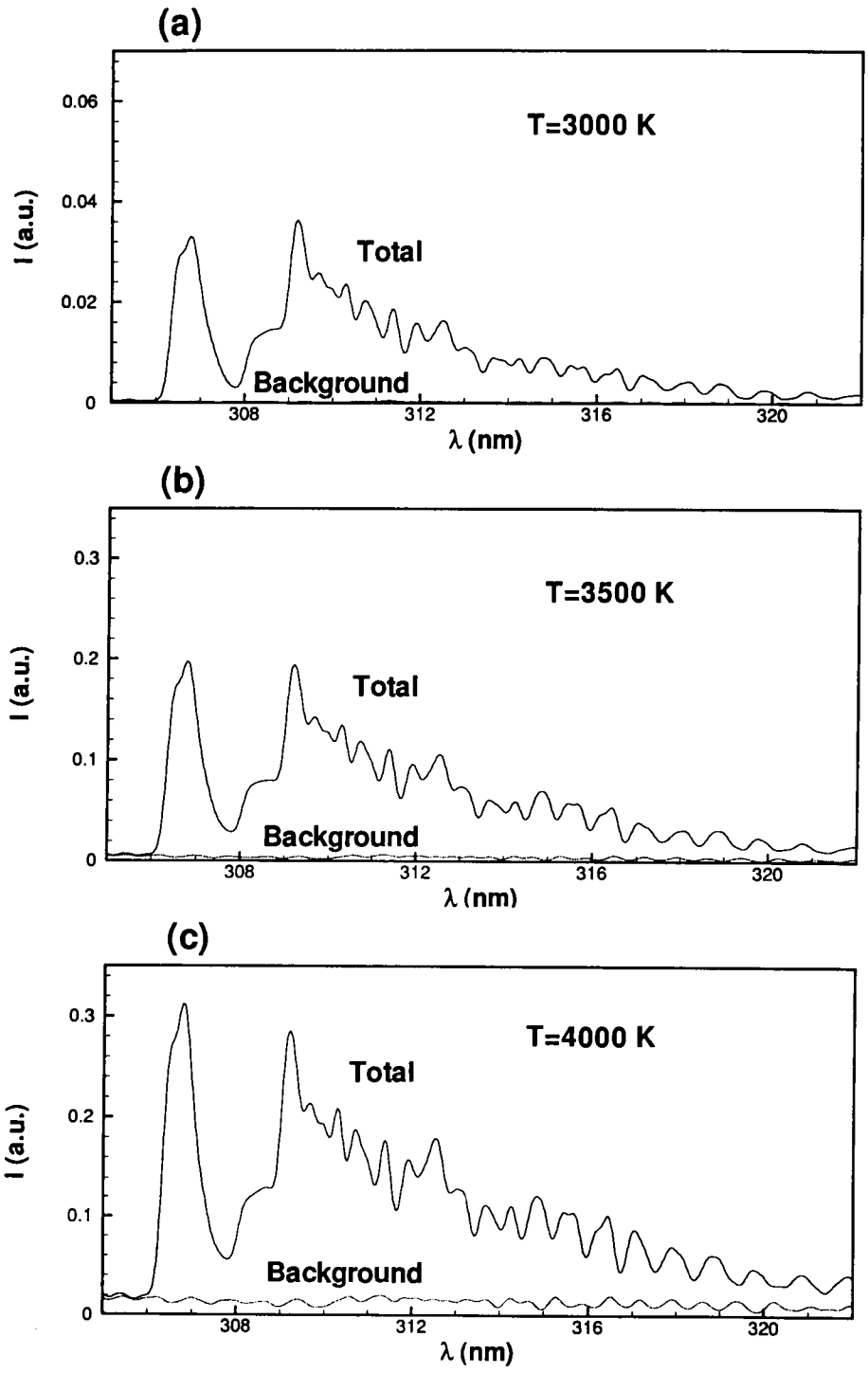

Figure 4.2: Synthetic emission spectra with and without OH (I): (a) $T = 3000K$; (b) $T = 3500K$; (c) $T = 4000K$.

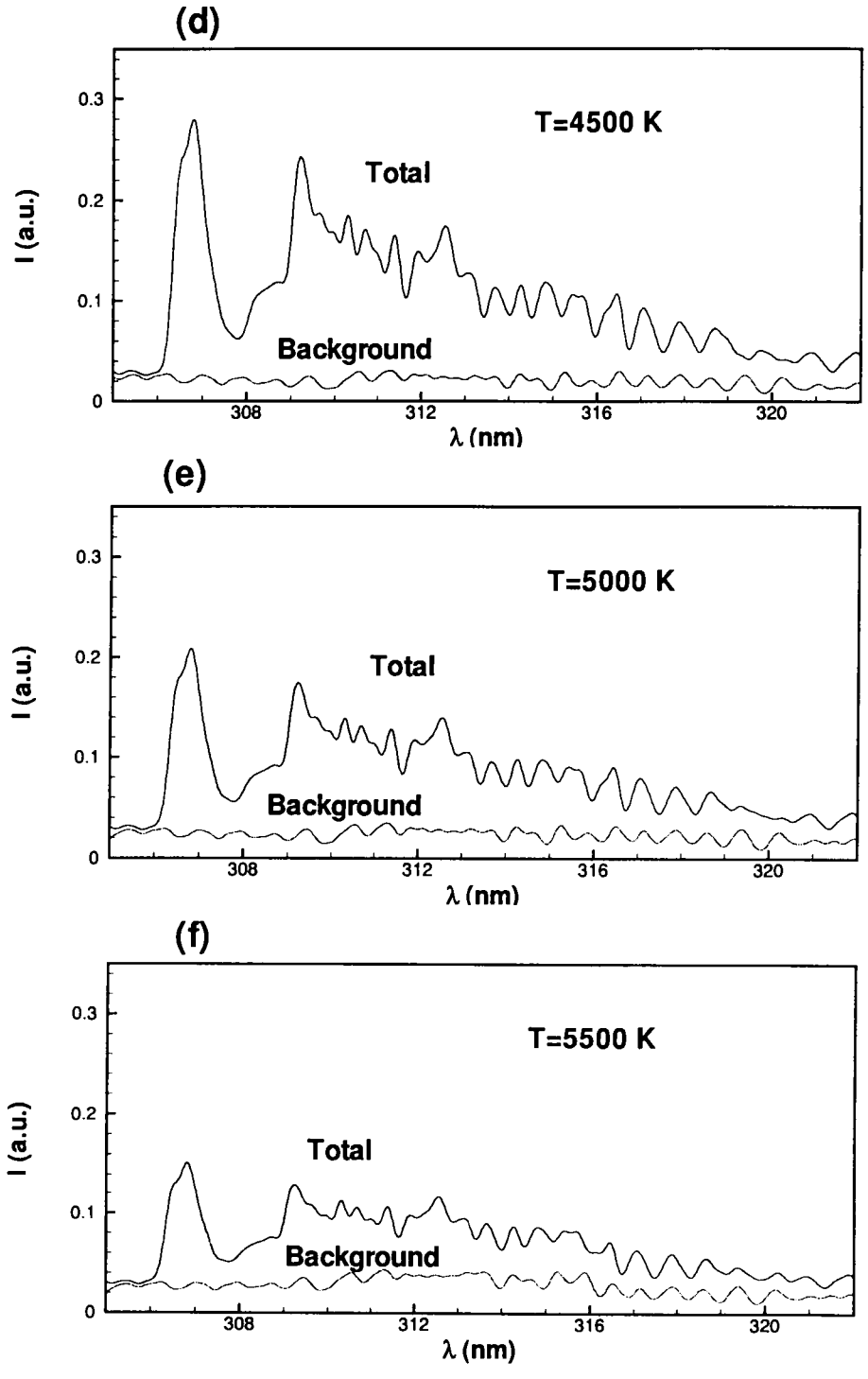

Figure 4.3: Synthetic emission spectra with and without OH (II): (d) $T = 4500K$; (e) $T = 5000K$; (f) $T = 5500K$.

quickly with higher temperature. The background emissions are negligible below 3500 K but become comparable with OH emissions above 4500 K.

4.4 Spectral Structure of the Diatomic Molecule

Herzberg [39] elaborated molecular spectra and molecular structure in his classic book. Of the many advanced discussions, only the Chidsey and Crosley's paper [40] is referenced here. In general, the electronic states are the primary structure. Each electronic state shows additional spectroscopic structure because of the relative motion of the two nuclei. This motion can be separated into a rotational mode and a vibrational mode. Therefore, each energy level is described by $\{e, v, J\}$ where $\{e\}$ defines electronic state, v is the vibrational quantum number and J is rotational quantum number. The energy term value can be expressed as

$$T_e(v, J) = E_e + G_e(v) + F_e(v, J), \tag{4.1}$$

where E_e is the contribution from electron-electron and electron-nuclei interaction with fixed nuclei positions, and

$$G_e(v) = \omega_e(v + 1/2) - \omega_e x_e(v + 1/2)^2 + \omega_e y_e(v + 1/2)^3 + ..., \tag{4.2}$$

$$F_e(v, J) = B_e(v)J(J + 1) - D_e(v)J^2(J + 1)^2 + ..., \tag{4.3}$$

where

$$B_e(v) = B_e - \alpha_e(v + 1/2) + ..., \tag{4.4}$$

$$D_e(v) = D_e + \beta_e(v + 1/2) + ... \tag{4.5}$$

The coefficients ω_e, x_e, y_e, B_e, D_e, α_e and β_e can be determined by fitting the molecular spectra using the above formulation. Practically, we fit a model Hamiltonian to the reported experimental spectra. Fitting with a model Hamiltonian yields accurate spectral positions and it also yields the wave functions and transition probabilities. All necessary data for computation of the investigated OH diatomic spectrum are contained in a file named line-strength file. Several line-strength files for different diatomic molecules have been generated at the Center for Laser Applications, The University of Tennessee Space Institute.

In the following, the computations of the intensity-values of spectral emissions from diatomic molecules are elaborated in terms of their wavelength and temperature dependence. The intensity of a spectral emission line, I_{nm}, is:

$$I_{nm} = N_n A_{nm} hc/\lambda_{nm}, \tag{4.6}$$

where n and m stand for the upper quantum state and lower quantum state, respectively. N_n is the number of molecules in upper state n. The photon energy, hc/λ_{nm}, is expressed in terms of the wave length λ_{nm}. The Einstein coefficient, A_{nm}, describes the transition probability for spontaneous emission. The emission spectral intensity at temperature T can be written approximately as

$$I(\lambda, N, T) \propto \frac{N}{\sum_l exp(-\epsilon_l/kT)} \sum_{nm} A_{nm}(hc/\lambda_{nm}) exp(-\epsilon_n/kT) g(\lambda, \lambda_{nm}), \tag{4.7}$$

where N is the number of total molecules and ϵ_n is the energy value of level n. $g(\lambda, \lambda_{nm})$ is the function of line profile.

4.5 Synthetic OH Spectra

The ground state of OH molecule is a $^2\Pi_i$ state and the first excited state is $^2\Sigma^+$. The structure of the $A^2\Sigma^+ \rightarrow X^2\Pi_i$ transition of OH is shown in references [39, 41] and the transition data are listed in reference [40]. The UTSI line-strength file for OH contains all the parameters needed to compute the spectrum.

The OH spectra can be calculated according to Eq. (4.7) with the specification of line profiles. The line profile is assumed as Gaussian in the study of OH spectra. Figure 4.4 shows low and high resolution spectra at a temperature of 4000 K. The full width at half maximum (FWHM) of the Gaussian lines for the low-resolution spectrum is 32 cm^{-1}. The FWHM for the high-resolution spectrum is 0.1 cm^{-1}. The fine structure of the spectrum is indicated for the high-resolution spectrum. Usually the measured emission spectra of OH matches the low-resolution spectrum. The spectrum in the range 305-322 nm primarily consists of $\Delta v = 0$ transitions, specifically the 0-0, 1-1 and 2-2 bands as indicated in Fig. 4.4, where 0, 1, and 2 are vibrational quantum numbers.

4.6 Fitting with OH Emission Spectra

The measured emission spectrum comprises contributions from many species. However, the OH emission dominates in a certain range of wavelength and temperature. The measured spectrum are separated into components contributed from OH and components contributed from all other species. The contributions from the other

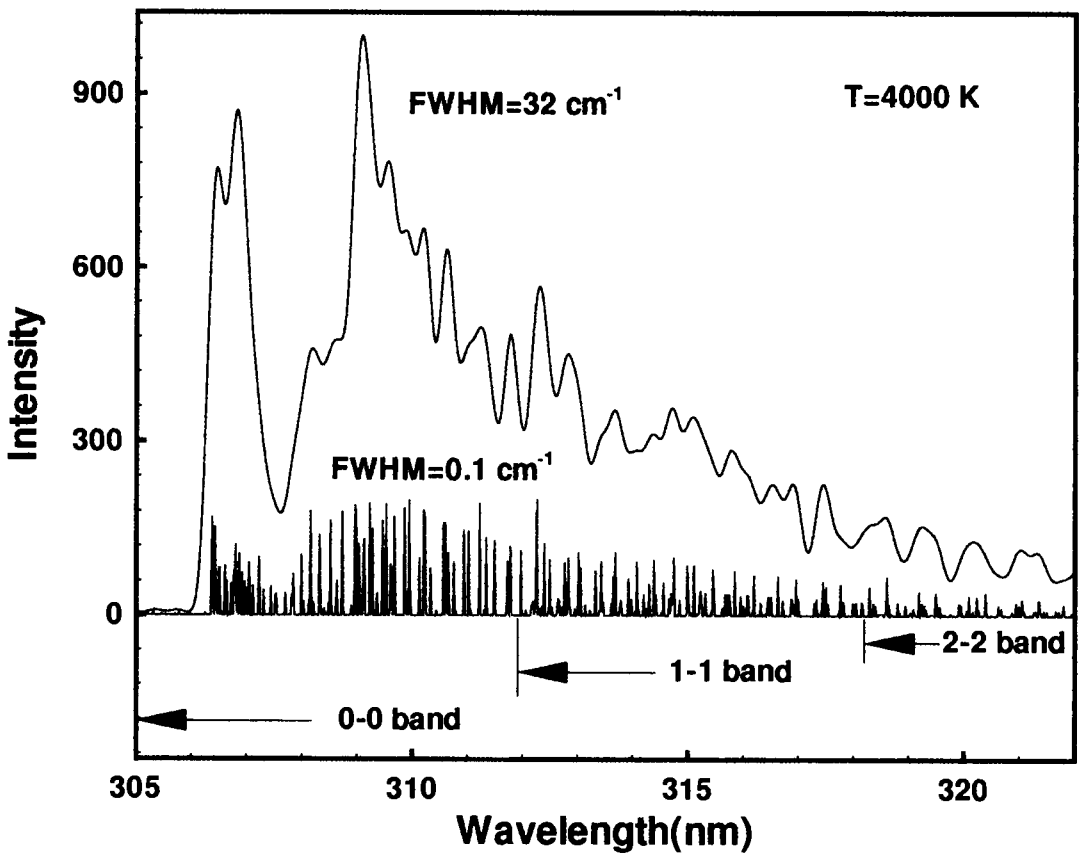

Figure 4.4: OH spectrum for $T = 4000K$: high resolution and low resolution.

species are referred to as background emission. Therefore, the emission spectrum can be formulated as

$$S(\lambda) = S_{OH}(\lambda) + S_b(\lambda), \tag{4.8}$$

where $S_{OH}(\lambda)$ represents the contributions form OH and $S_b(\lambda)$ represents the contributions from the background emission. The background $S_b(\lambda)$ is assumed constant for the relatively small background emissions.

A measured spectrum represents the spectral intensity accumulation in both the spatial and temporal domain. Therefore, the OH contribution in measured spectrum is also an integration of spectral intensity over emission volume and time gate. Using the mathematical mean value theorem, the OH contribution in measured spectrum is

$$S_{OH}(\lambda) = \int I(\lambda, N(\mathbf{x}, t), T(\mathbf{x}, t))dtd^3x = I(\lambda, N(\mathbf{x}_0, t_0), T(\mathbf{x}_0, t_0))\tau V, \tag{4.9}$$

where $\mathbf{x}_0$ and t_0 are mean values, τ is the OMA gate width and V is the volume of plasma from which the emission is collected. Equation (4.9) implies that the measured OH spectral intensity is the same as the spectral intensity obtained when all OH molecules are distributed uniformly with mean number density $N(\mathbf{x}_0, t_0)$ and mean temperature $T(\mathbf{x}_0, t_0)$.

In the following, the temperature T will indicate this mean temperature. Therefore, the measured OH spectral intensity can be evaluated from

$$S_{OH}(\lambda) \propto \sum_{nm} A_{nm}(hc/\lambda_{nm})exp(-\epsilon_n/kT)g(\lambda, \lambda_{nm}). \tag{4.10}$$

There are usually two methods in the analysis of spectra: the Boltzmann plot and the direct least-square fitting. We use the direct nonlinear least-square fitting (NL-LSF) in the analysis of OH spectra. The NL-LSF is applicable generally for all kinds of spectra.

Now we proceed with the discussion of spectra analysis by using least-square fitting. The spectroscopic data consists of a set of pair values (y_j, λ_j) where y_j is measured spectral intensity at pixel position j which is associated with λ_j. The emission spectrum is modeled as the sum of contribution from OH and a constant background. Similar to Eq. (3.32), we use a merit function defined as

$$\chi^2 = \sum_{j=1}^{M} [S_{OH}(\lambda_j) + B - y_j]^2 \tag{4.11}$$

$$= \sum_{j=1}^{M} \left[A \sum_{nm} A_{nm}(hc/\lambda_{nm}) exp(-\epsilon_n/kT) g(\lambda, \lambda_{nm}) + B - y_j \right]^2 \tag{4.12}$$

The fitting parameters in merit function are the spectroscopic temperature T, a factor A, a background B and the parameters in line profile function $g(\lambda, \lambda_{nm})$, for example, the line width D if $g(\lambda, \lambda_{nm})$ is assumed to be Gaussian shape.

For a typical spectrum measured at 80 μs delay time, the fitting temperatures are 3667 K, 3744K and 3508 K for fitting in three different ranges of wavelength 305-322 nm, 305-312 nm and 312-318 nm, respectively. Figure 4.5 (a), (b) and (c) show the measured spectra (black circles), the fitted spectra and their differences in the ranges of 305-322 nm, 305-312 nm and 312-318 nm, respectively. The structures in the differences come from the assumption of the data model that includes background and the line profiles $g(\lambda, \lambda_{nm})$.

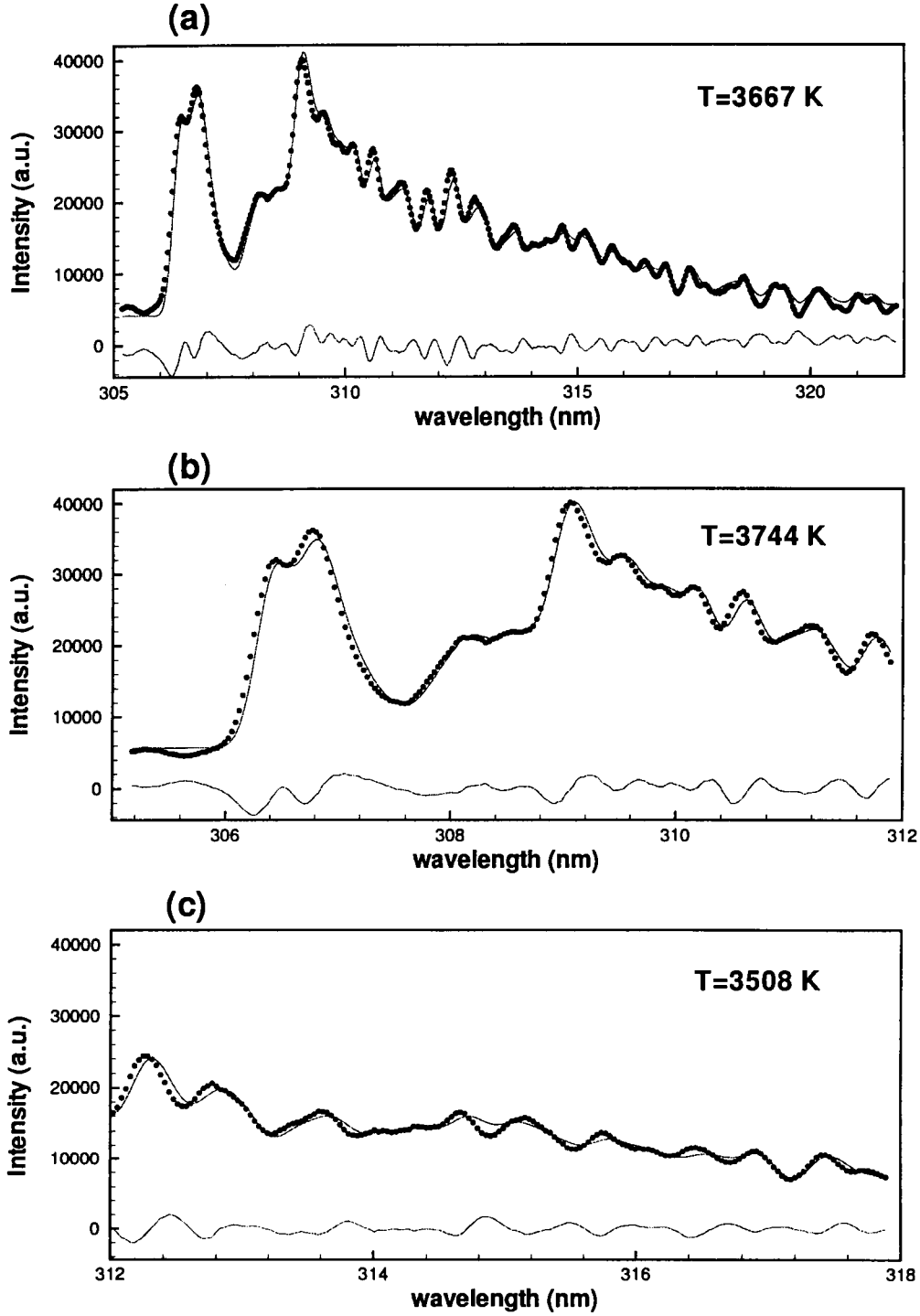

Figure 4.5: Measured and fitted emission spectra 80 μs after optical breakdown: (a) in the range 305-325 nm; (b) in the range 305-312 nm; (c) in the range 312-318 nm.

The reason of fitting in three different wavelength ranges is that different vibration states could be in nonequilibrium. Usually populations in different rotation-vibration levels of OH are produced on the dependence of the chemical dynamics. The OH molecules are redistributed in the rotation-vibration levels after the production. The energy transfer rate between different energy levels is dependent on the pressure and gas components. Advanced discussions about rotation energy transfer and vibration energy transfer may be found in the literature [42, 43, 44, 45]. Typically the rotation energy transfer rate of OH is in order of nanoseconds and the vibration energy transfer rate of OH is in order of microseconds. Therefore, the rotational temperature is usually the same as the temperature of the surrounding gases. The temperature including different vibration states might deviate from the temperature of surrounding gases. All quantum states are assumed in thermal equilibrium with the surrounding gases when the spectrum is fitted in the range of 305-322 nm. It is recommended to fit the data with 0-0 band in the range of 305-312 nm.

Both 0-0 band and 1-1 band are present in the range of 312-318 nm. It is assumed that the vibrational quantum state 0 is not in thermal equilibrium with the vibrational state 1. The fitting result does not provide any evidence of internal nonequilibrium of vibrational state 0 and vibrational state 1. However, fitting in this range yields big errors because more fitting parameters are presented in the merit function while fewer structures can be seen in this range. The deviation in temperature amounts to 236 K and 159 K for fitting in the wavelength ranges 305-312 nm and 305-322 nm, respectively.

Figure 4.6 (a), (b) and (c) show the scatter plots of (χ^2, T) for fitting in the range 305-322 nm, 305-312 nm and 312-318 nm, respectively. These graphs illustrate the fitting procedure results as obtained by the use of Powell's method. [36] The scatter plotter may be considered as a (χ^2, T, A, B, D) projection onto (χ^2, T) since there are four variables (T, A, B, D) in the merit function; (A, B, D) are not shown in the scatter plot. The minimum of the temperature-dependent χ^2 points indicates the quality of the fitting. It is shown that the merit function in Fig. 4.6 (b) converges to the minimum quickly and the merit function in Fig. 4.6 (c) converges to the minimum slowly. For a good LSF fitting, the merit function should converge to the minimum quickly. Therefore, fitting in 305-312 nm is the most reliable method for the three investigated wavelength regimes.

4.7 Error Analysis by the Use of Monte Carlo Simulations

The process of Monte Carlo simulation is similar to that discussed in Chapter 3. New sets of synthetic data are generated by adding random number to each measured data,

$$y'_j = y_j + x * y_{mean} * R(), \tag{4.13}$$

where y_j is measured data and y_{mean} is the mean value of $\{y_j\}$. R() is a generator function of random number with normal probability distribution. x is a constant factor and may be estimated from the differences between the measured data and the fitting curve. x amounts to typically 10-15 %. Note that the added random

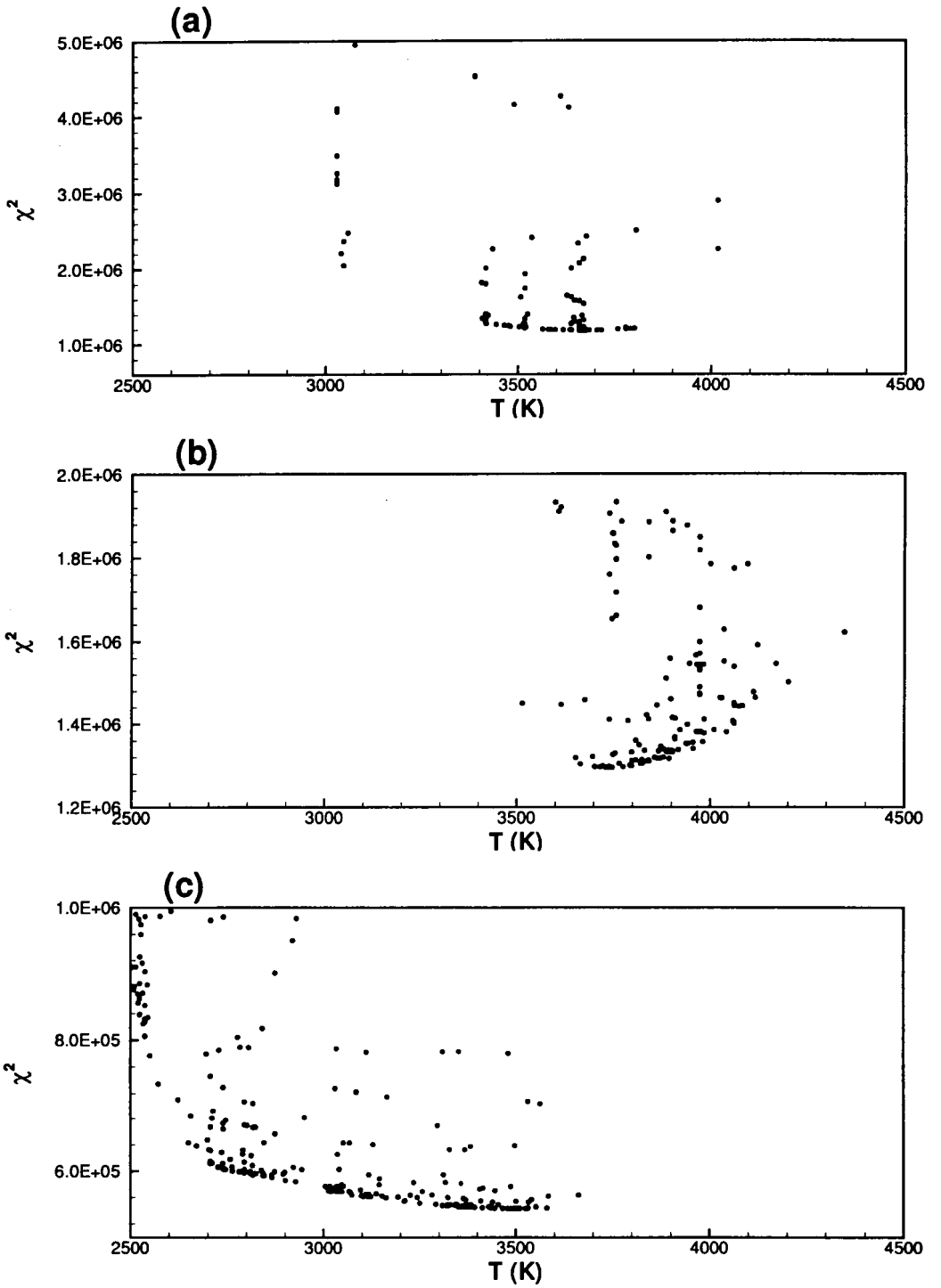

Figure 4.6: Results for the value of the merit function: (a) in the range 305-325 nm; (b) in the range 305-312 nm; (c) in the range 312-318 nm.

number is $x * y_{mean} * R()$ in the following investigations. New sets of parameters are obtained by fitting the synthetic data. The merit function Eq. (4.11) is utilized in the least-square fitting. The data reduction is performed in the range of 305-312 nm and 305-322 nm. The averages, variances and correlations of the parameters temperature, background and line width are determined from the computed parameter sets.

Figure 4.7 and 4.8 show the scatter plots of (T, A), (T, B) and (T, D) for fitting in the range of 305-312 nm and 305-322 nm, respectively. The error magnitude is set to $x = 0.1$. The averages and the variances of T, A, B and D are illustrated in the figures. The correlation coefficients between temperature T and the other parameters (A, B, D) are also shown in Fig. 4.7 and Fig. 4.8. The correlation coefficients are listed in Table 4.1 and in Table 4.2. It is shown that the background B, which indicates the largest correlation with T, is important in determining the spectroscopic temperature. The factor A and the line width D are almost not correlated with the spectroscopic temperature. In Chapter 3 quantity U and factor A show the largest correlation while quantity U and the background B show hardly any relation. The primary reason for the weak correlation between T and A in OH fitting is due to the spectral structures of OH. There are only two lines in the two-separate-line model of Chapter 3 while there are more than 30 lines in just one branch of a vibrational band of OH spectrum. The primary reason for the strong correlation between T and B in OH fitting is due to the background emission.

Now the relations are investigated between fitting parameters and error magnitude x. Monte Carlo simulations are performed both in the range of 305-312 nm and

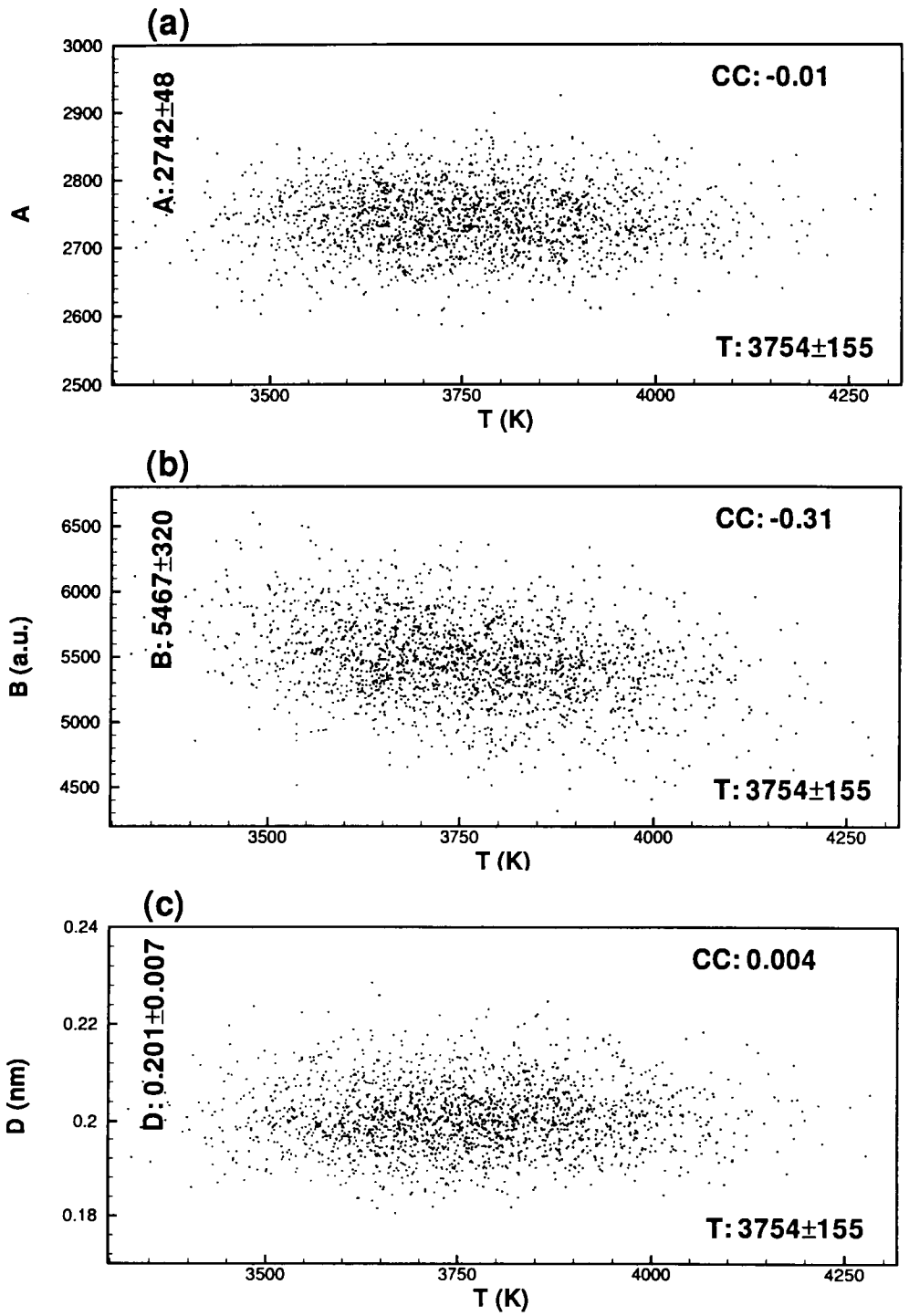

Figure 4.7: Scatter plots from Monte Carlo simulations in the range 305-312 nm: (a) (A, T); (b) (B, T); (c) (D, T).

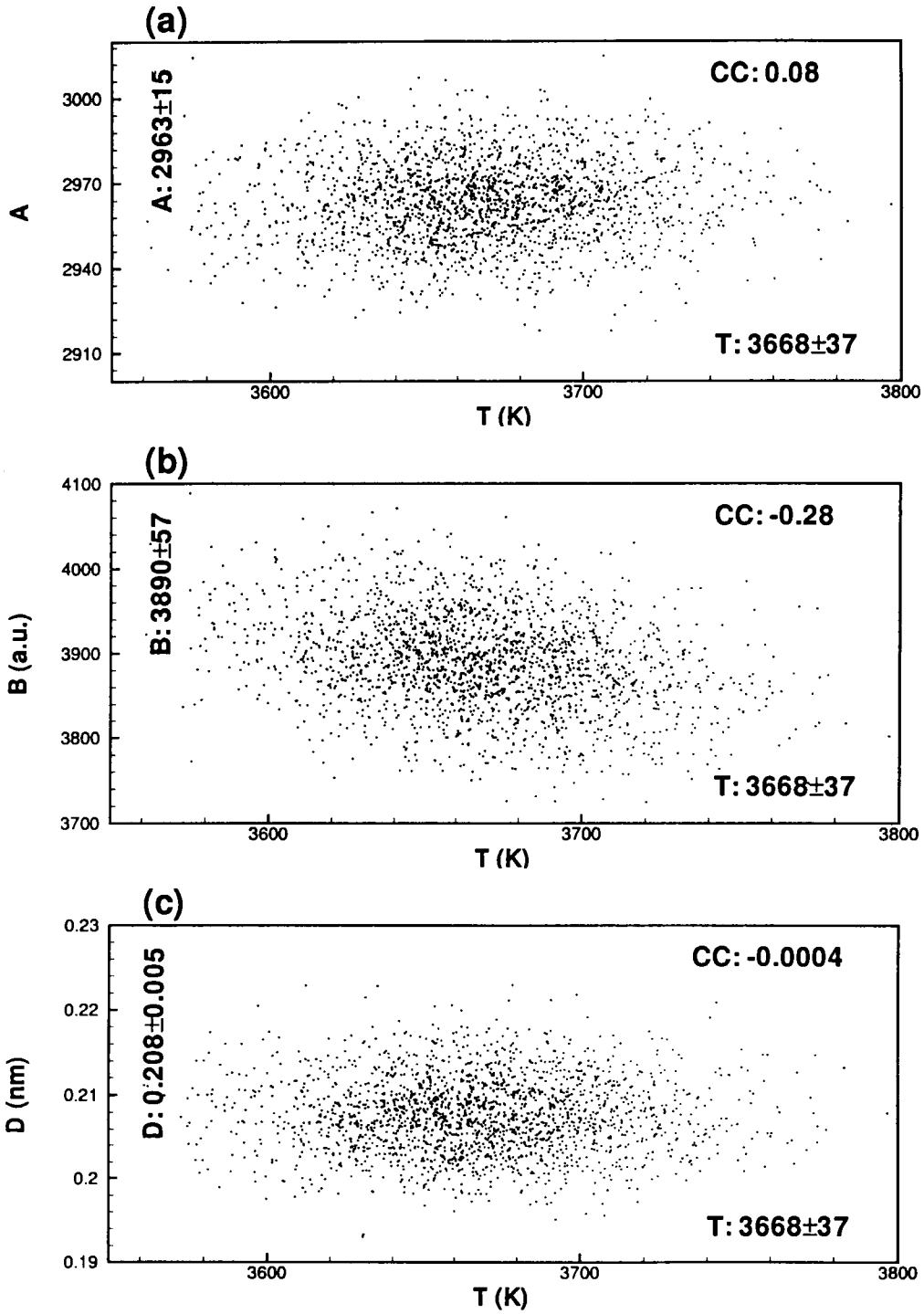

Figure 4.8: Scatter plots from Monte Carlo simulations in the range 305-322 nm: (a) (A, T); (b) (B, T); (c) (D, T).

Table 4.1: Correlation coefficients: in the range of 305-312 nm.

	T	A	B	D
T		-0.01	-0.31	0.004
A	-0.01		-0.83	0.37
B	-0.31	-0.83		-0.31
D	0.004	0.37	-0.31	

Table 4.2: Correlation coefficients: in the range of 305-322 nm.

	T	A	B	D
T		0.08	-0.28	-0.0004
A	0.08		-0.65	0.06
B	-0.28	-0.65		0.05
D	-0.0004	0.06	0.05	

in the range of 305-322 nm. In the investigation, the line width D is fixed at 0.21 nm since it has almost zero correlation with the temperature. The averages and the variances of parameters for different magnitude x are listed in Table 4.3 and in Table 4.4. All of the variances are almost proportional to the magnitude x for x smaller than 0.3. The variance from Monte Carlo simulations in the range of 305-322 nm is much smaller than that in the range of 305-312 nm. There are two main reasons: first, there are more data in the range 305-322 nm, second, the contributions from high vibrational quantum states reduces the variances. This has been previously discussed in Chapter 3, where it was shown that larger γ gives smaller variances (see Table 3.1). Figure 4.9 shows the bar chart of the temperature distribution for different error magnitudes x. The Monte Carlo simulations are performed in the range of 305-322 nm. The averages and variances of temperature from Monte Carlo simula-

Table 4.3: Averages and variances of parameters: fitting in 305-312 nm.

x	0.1	0.2	0.3
$T(K)$	3754± 155	3776± 315	3813± 492
A	2742± 48	2741± 97	2745± 147
B	5467± 320	5469± 649	5441± 986

Table 4.4: Averages and variances of parameters: fitting in 305-322 nm.

x	0.1	0.2	0.3
$T(K)$	3671± 37	3673± 74	3677± 111
A	2967± 14	2967± 28	2968± 43
B	3864± 57	3864± 113	3859± 168

tions are also shown in the figure. The solid curves are Gaussian distributions with the same averages and variances as shown in the figure. However, the temperature distribution looks more like a Poisson distribution than a Gaussian distribution.

The comparison of two types of random errors described by Eq. (3.24) and Eq. (4.13) is discussed in the following. The Monte Carlo simulations were performed for the spectrum recorded at 100 μs delay in the range of 305-322 nm. The average and variance of the temperature are found to be $T = 3366K$ and $\sigma_T = 40K$ for random errors with magnitude of 10% measured intensity (see Eq. (3.24)). The average and the variance of the temperature are found to be $T = 3368K$ and $\sigma_T = 31K$ for random errors with magnitude of 10% mean intensity (see Eq. (4.13)). The average temperatures are very close while the variances are slightly different. The explanation for the difference in variance is that larger errors are weighted on lower energy levels and fewer errors are weighted on higher energy levels when Eq. (3.24)

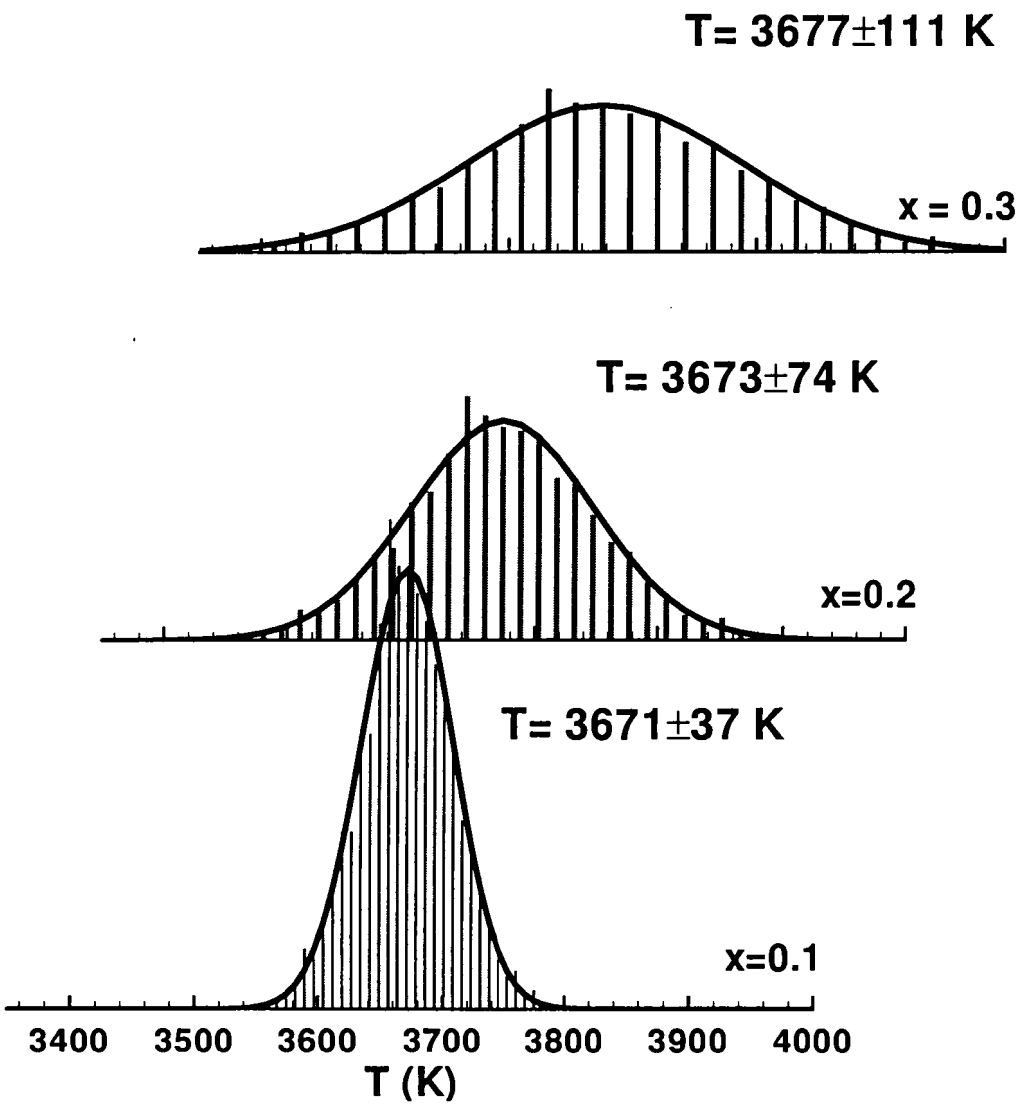

Figure 4.9: Temperature distributions for different error magnitudes from Monte Carlo simulations in the range 305-322 nm.

is applied. As mentioned previously, lower energy levels yield larger variance while higher energy levels yield smaller variance.

The primary errors are due to the background emissions, shot-to-shot variations and unknown spectral line profiles. According to the NEQAIR results, the background emissions are negligible for temperatures below 3500 K, and the shot-to-shot variations of the radiating plasma are the dominant contributions to the errors in the measured spectral intensity. These variations are assumed to be proportional to the measured spectral intensity. The errors due to unknown spectral line profiles would become also significant when the errors due to the background emission and the shot-to-shot variations are small. However, Eq. (4.13) is used to simulate the errors in all numerical investigations.

Figure 4.10 shows the temperature decay versus delay time. The red squares represent the spectroscopic temperatures of fitting in the range of 305-322 nm. The blue triangles represent the spectroscopic temperatures of fitting in the range of 305-312 nm. It is noted that the temperature decay rates are different. The reason for this difference is believed to be associated with the dynamics of energy transfer. The black circles and error bars represent the averages and variances of spectroscopic temperate from Monte Carlo simulations. The Monte Carlo simulations are performed in the range of 305-312 nm and with error magnitude $x = 0.2$. The errors for the spectroscopic temperature are large for time delays smaller than 50 μs and they are moderately small for time delays larger than 100 μs.

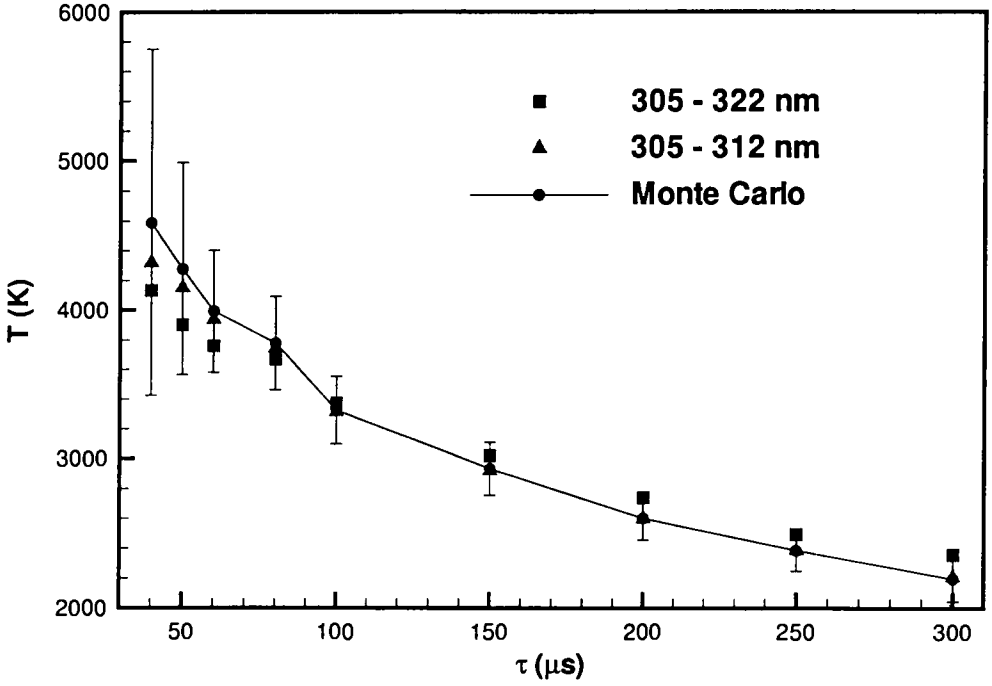

Figure 4.10: The temperature and its variance versus delay time.

Chapter 5

Formulation of Image Analysis

5.1 Introduction

Imaging techniques are frequently applied in research as for example discussed in the following literature [46, 47, 48, 49, 50]. In this Chapter, the following techniques are addressed in the image analyses: Fourier transforms, discrete Fourier transform, sampling theorem and filtering. Of many techniques on image analyses, [4] the technique of Fourier transform [36, 51, 52, 53] is unique to transform the information between space and spatial frequency. The information in an image can be decomposed according to the spatial frequencies. With an appropriate filter, different components may be separated. Since an image usually consists of a finite data array, the discrete Fourier transform are applied in image analysis. The algorithm of fast Fourier transform [36] is utilized in the computations of discrete Fourier transform.

5.2 Fourier Transform Details

The Fourier transform equations are:

$$h(t) = \frac{1}{2\pi}\int_{-\infty}^{\infty} H(\omega)e^{i\omega t}d\omega, \tag{5.1}$$

$$H(\omega) = \int_{-\infty}^{\infty} h(t)e^{-i\omega t}dt. \tag{5.2}$$

The kernels for Fourier transform have the typical $exp\{\pm i\omega t\}$ form. The Fourier transform can be viewed as a specific type of Fredholm integral equation of the first kind, with special orthogonal kernels. Each kernel contains information at different frequency.

The properties of Fourier transform may be found in many publications, for example, the two references [52, 53]. With two functions $g(t)$ and $h(t)$, some relations are summarized below. The convolution of the two functions, denoted $g*h$, is defined by

$$g * h \equiv \int_{-\infty}^{\infty} g(\tau)h(t-\tau)d\tau. \tag{5.3}$$

The Fourier transform of $g * h$ is multiplication of Fourier transforms of g and h,

$$\mathcal{F}(g * h) = \mathcal{F}(g)\mathcal{F}(h). \tag{5.4}$$

The correlation of the two functions, denoted $Corr(g,h)$, is defined by

$$Corr(g,h) \equiv \int_{-\infty}^{\infty} g(\tau+t)h^*(\tau)d\tau. \tag{5.5}$$

The Fourier transform of $Corr(g,h)$ is:

$$\mathcal{F}(Corr(g,h)) = \mathcal{F}(g)\mathcal{F}^*(h). \tag{5.6}$$

If g and h are the same function, the Fourier transform of the autocorrelation function is:

$$\mathcal{F}(Corr(g,g)) = |\mathcal{F}(g)|^2, \tag{5.7}$$

which is known as Wiener-Kintchine theorem. After inverse Fourier transform, one obtains the following relation for power spectrum at $t = 0$:

$$\int_{-\infty}^{\infty} |\mathcal{F}(g)|^2 d\omega = 2\pi \int_{-\infty}^{\infty} |g(\tau)|^2 d\tau. \tag{5.8}$$

5.3 Sampling Theorem and Discrete Fourier Transform

From the sampling theorem [36, 52, 53] we know that if $H(\omega) = 0$ for all $|\omega| \geq \omega_c$, then the function $h(t)$ is completely determined by its samples h_p taken at an interval $\Delta = \frac{\pi}{\omega_c}$. The frequency ω_c is called Nyquist critical frequency. The function $h(t)$ is given explicitly by the formula

$$h(t) = \sum_{p=-\infty}^{\infty} \frac{h_p}{\Delta} \frac{sin(\omega_c t - 2p\pi)}{\omega_c t - 2p\pi}. \tag{5.9}$$

The Fourier transform is found by substituting the function $h(t)$ into Eq. (5.2),

$$H(\omega) = \sum_{p=-\infty}^{\infty} h_p e^{-2\pi i p\omega/\omega_c} \qquad |\omega| < \omega_c; \qquad 0 \qquad |\omega| \geq \omega_c. \tag{5.10}$$

For experimental data, we have a finite number of data points, N. With N numbers of input, we produce no more than N independent numbers of output. So one samples only at the discrete values

$$\omega_n = n\omega_c/N, \qquad n = 0, 1, 2, ..., N-1. \tag{5.11}$$

The discrete Fourier transform is obtained,

$$H_n = \sum_{p=0}^{N-1} h_p e^{-2\pi i n p/N}. \tag{5.12}$$

The definition of H_n is extended to $n = -1, -2, ..., -N+1$. One obtains the following relations,

$$H_{-n} = H_{N-n}, \tag{5.13}$$

and,

$$H_{-n} = H_n^* \tag{5.14}$$

for real h_p. The discrete inverse Fourier transform is defined as

$$h_p = \frac{1}{N} \sum_{n=0}^{N-1} H_n e^{2\pi i n p/N}. \tag{5.15}$$

For discrete Fourier transform applications, all data are required to be equally spaced. If the data are not equally spaced, then the data need to be converted to equal intervals by the use of interpolation. The algorithm of fast Fourier transform [36] is utilized in discrete Fourier transform.

5.4 Filters

The term "filter" is introduced for a system with an input and an output [53]. We are only interested in simple filters that can be specified by a function $s(x)$. The output, $h_2(x)$, is obtained from the input, $h_1(x)$, by the use of the following relation,

$$h_2(x) = h_1(x)s(x). \tag{5.16}$$

By the use of Eq. (5.4), the Fourier transform of the output is the convolution of Fourier transform of the input and Fourier transform of filter function,

$$\mathcal{F}(h_2) = \mathcal{F}(h_1) * \mathcal{F}(s). \tag{5.17}$$

An example for a filter function is given in the following for the pair of Fourier transform variables x and k. A typical rectangular filter function in x-space is:

$$s(x) = 1 \qquad |x| \leq a; \qquad 0 \qquad |x| > a. \tag{5.18}$$

The Fourier transform of the rectangular filter is the sinc function $2asinc(ka)$. The output in k-space is the convolution,

$$H_2(k) = \int_{-\infty}^{\infty} 2asinc[(k-k')a]H_1(k')dk'. \tag{5.19}$$

Similarly, in k-space a rectangular filter may also be introduced to select and/or suppress contributions of specific spatial frequencies. The output in x-space would then be computed as the convolution of the sinc function with the input function.

Equation (5.19) is a Fredholm integral equation of the first kind. The kernels are sinc functions. By the use of eigen-analysis (see Chapter 2), a number of data at discrete k is sufficient to describe the output in a range between c and d. As in Chapter 2, the eigenvalues of covariant matrix and the relative information are used to describe how many data are significant. To accomplish the analysis numerically, M data are assumed to be taken in equal interval between the range c and d, i.e., $k_j = c+(j-1)\Delta$, j=1, 2, ..., M where Δ is the interval of data points, $\Delta = \dfrac{(d-c)}{(M-1)}$. In the computations the range c and d are set -100 and +100, respectively.

Figure 5.1 shows the eigenvalues and relative information for different filter widths when the interval is fixed. The number of significant data is nearly proportional to the filter width. Figure 5.2 shows the eigenvalues and relative information for different data numbers when the filter width is fixed. A critical number is 64. Eigenvalues

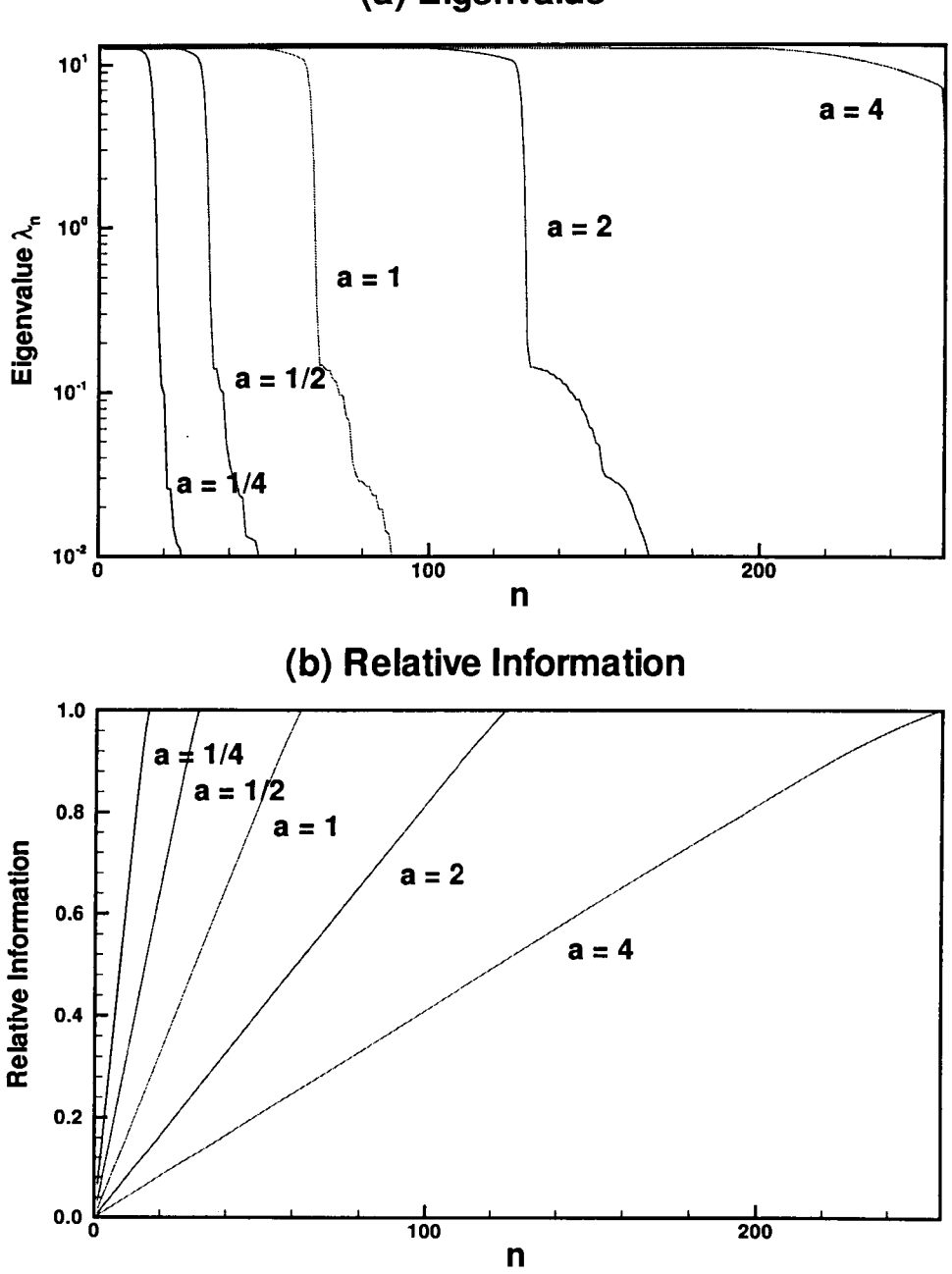

Figure 5.1: Eigenvalues and relative information for sinc kernels (I): fixed range c=-100, d=100 and fixed data number M=256.

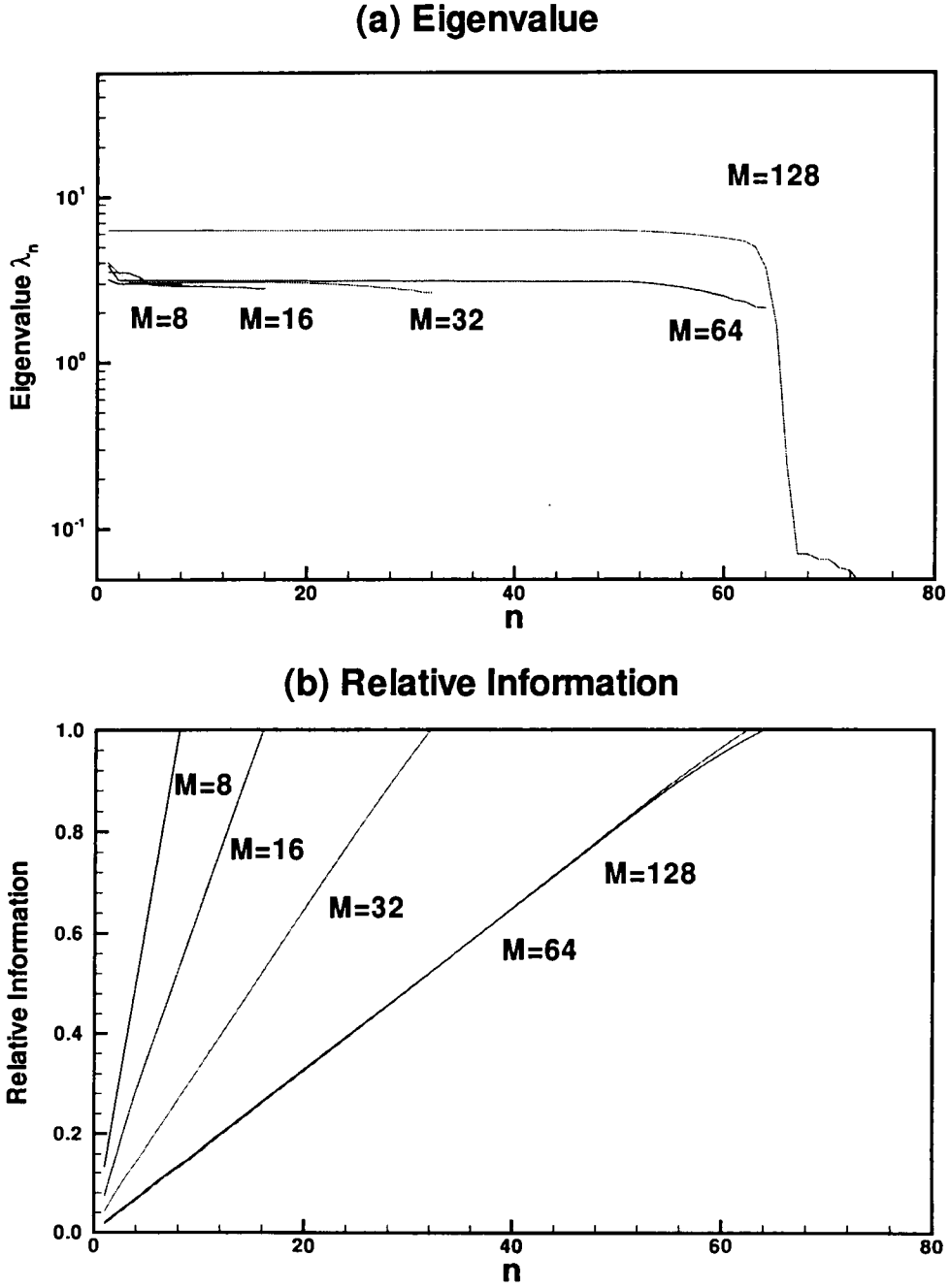

Figure 5.2: Eigenvalues and relative information for sinc kernels (II): fixed range c=-100, d=100 and fixed filter width a=1.

change dramatically around this number. The number of significant data is proportional to the number of total data, M, when M is less than 64. The curves of relative information for data number M bigger than 64 are very similar.

From the numerical results, the number of significant data is proportional to the product of filter-width and the interval. The following relation is found between the filter width and the optimum interval for the output data,

$$2a\Delta \sim 6.3. \tag{5.20}$$

One can obtain all of the information by collecting data at an interval $3/a$.

5.5 Two Dimensional Fourier Transform

The equations for the two dimensional Fourier transform are:

$$h(\mathbf{x}) = \frac{1}{(2\pi)^2}\int_{-\infty}^{\infty}\int_{-\infty}^{\infty} H(\mathbf{k})e^{\mathbf{ik\cdot x}}d\mathbf{k}, \tag{5.21}$$

$$H(\mathbf{k}) = \int_{-\infty}^{\infty}\int_{-\infty}^{\infty} h(\mathbf{x})e^{-\mathbf{ik\cdot x}}d\mathbf{x}. \tag{5.22}$$

The two-dimensional discrete formulation can be inferred from the sampling theorem as in the previous section. If $H(\mathbf{k}) = 0$ for all $|k_1| \geq k_{1c}$, $|k_2| \geq k_{2c}$, then the function $h(\mathbf{x})$ is completely determined by its samples h_{pq}. The subscripts 1, 2 represent the two orthogonal directions. Function $h(\mathbf{x})$ is given explicitly by the following formula,

$$h(\mathbf{x}) = \sum_{p=-\infty}^{\infty}\sum_{q=-\infty}^{\infty} \frac{h_{pq}}{\Delta_1\Delta_2}\frac{sin(k_{1c}x_1 - 2p\pi)}{k_{1c}x_1 - 2p\pi}\frac{sin(k_{2c}x_2 - 2q\pi)}{k_{2c}x_2 - 2q\pi}. \tag{5.23}$$

Substitution of $h(\mathbf{x})$ into Eq. (5.22) yields the discrete Fourier transform,

$$H(\mathbf{k}) = \sum_{p=-\infty}^{\infty}\sum_{q=-\infty}^{\infty} h_{pq}e^{-2\pi ipk_1/k_{1c}}e^{-2\pi iqk_2/k_{2c}} \tag{5.24}$$

for $k_1 < k_{1c}$ and $k_2 < k_{2c}$; otherwise $H(\mathbf{k}) = 0$.

For $M \times N$ data array $\{h_{pq}\}$, the discrete Fourier transform is defined by

$$H_{mn} = \sum_{p=0}^{N-1} \sum_{q=0}^{M-1} h_{pq} e^{-2\pi inp/N} e^{-2\pi imq/M}. \tag{5.25}$$

The discrete inverse Fourier transform is defined by

$$h_{pq} = \frac{1}{MN} \sum_{m=0}^{M-1} \sum_{n=0}^{N-1} H_{mn} e^{2\pi inp/N} e^{2\pi imq/M}. \tag{5.26}$$

It is appropriate to make a change of variables to polar format [51] if the function $h(x)$ has circular symmetry.

Chapter 6

Analysis of Interference Images

6.1 Introduction

Femtosecond-pulse laser amplification and the potential applications for optical breakdown, ablation and spectroscopic studies necessitate the characterization of ultrashort laser pulses including wavelength, band width, pulse width and coherence length. A simple means of characterization would be the measurement of the spectrum of the pulse. The spectrum yields the center wavelength and the bandwidth of the pulse. The pulse-width can be inferred for a transform-limited pulse [54] by assuming the temporal shape. An alternative method is the measurement of the autocorrelation function. J. C. Diels [55, 56] and K. Naganuma [57] published some early works on this subject. Subsequently, J. Chilla and O. Martinez [58, 59, 60] developed a frequency domain method to unambiguously determine the pulse shape and phase. D. Kane and R. Trebino [61, 62] and J. Paye [63] introduced the technique of frequency-resolved optical gating. More recent works are elaborated in the literature [64, 65, 66, 67, 68]. Typically, a nonlinear medium is required to generate a second or third harmonic signal that is associated with the autocorrelation trace.

The technique of interferometry or holography [29, 30, 31, 32, 68, 69] may be used to measure the correlation function. The coherence length of a laser pulse can be determined from the correlation function.

In this dissertation we present measurements of the autocorrelation function by scanning the relative delay of the two laser beams and by recording interference images. A nonlinear medium is not required in the overlap region. The image is decomposed into the spatial frequencies by the use of Fourier transform techniques [30, 31, 32, 68]. The interference information is usually restricted to a specific range of spatial frequencies in Fourier transform space. This range may be separated from the low frequency background and high frequency noise. The interference information can be extracted through an appropriate filter to yield the autocorrelation coefficient of the pulse. The pulse width is determined by fitting the autocorrelation coefficients for an assumed hyperbolic secant pulse-shape.

6.2 Experimental Arrangement

In this dissertation work, the interferometric method is used to measure the correlation of femtosecond laser pulses. The interference patterns of overlapping ultra-short pulses are directly recorded by the use of a CCD camera. Figure 6.1 shows the experimental arrangement. The Spectra Physics model Tsunami Ti:Sapphire laser pulses, produced at a repetition rate of 76 Mhz, are specified to be as short as 60 femtosecond when dispersion due to transit through the output coupler is fully compensated. The laser beam is reflected by mirrors M1, M2 and M3. A portion of the laser beam

(see BS1) enters a Jarrell-Ash MonoSpec 27 spectrometer and the approximately 10 nm band-width spectra are monitored by the use of a Princeton Applied Research optical multichannel analyzer (OMA). For the measurement of interference images the laser beam is further split by the use of a wedge (BS2) as a beam splitter. The tilt of the mirrors and the wedge are adjusted to obtain spatial overlap of the beams in the field of view of the camera. Figure 6.2 shows the details of the box indicated in Fig. 6.1. The reflected beam from the front-face of the wedge is reflected by mirrors M4 and M5 and passes through the wedge to the interference field. The transmitted beam is reflected by mirror M6 and by the back-face of the wedge to the interference field. Two other relatively strong reflections are also illustrated in the figure. The weak multiple reflections are not shown for simplicity. The mirror M6 is mounted on an AEROTECH model ATS302 position stage. The time delay between the two beams is varied by systematically translating the mirror M6. The two beams each pass the wedge once and are subject to similar dispersion. Therefore, it can be assumed that the pulses have the same temporal profile. The intensity ratio of two beams is close to 1. However, the exact value of the intensity ratio is not important in our analysis.

A digital camera, model EDC-1000HR, is used to record the interference patterns. Neutral density filters are used to adjust the light intensity below the camera saturation levels. The laser beam is attenuated by typically 2-3 orders of magnitude. The magnification lens LEICA MONOZOOM 7 is used to record magnified interference patterns. The exposure time of the camera and the translator's motion

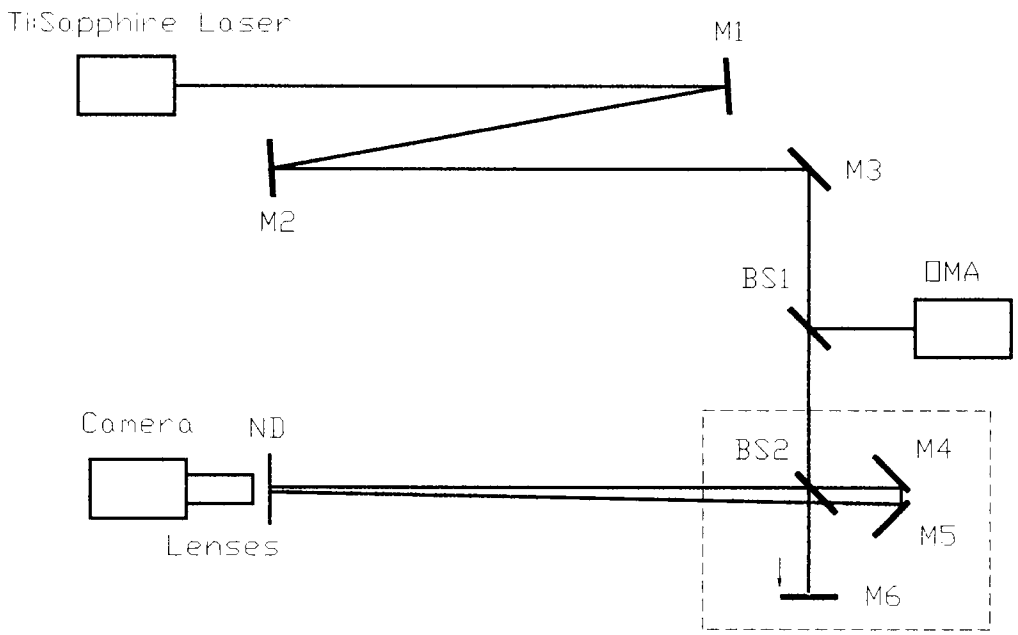

Figure 6.1: Experimental arrangement for the short pulse interference measurements.

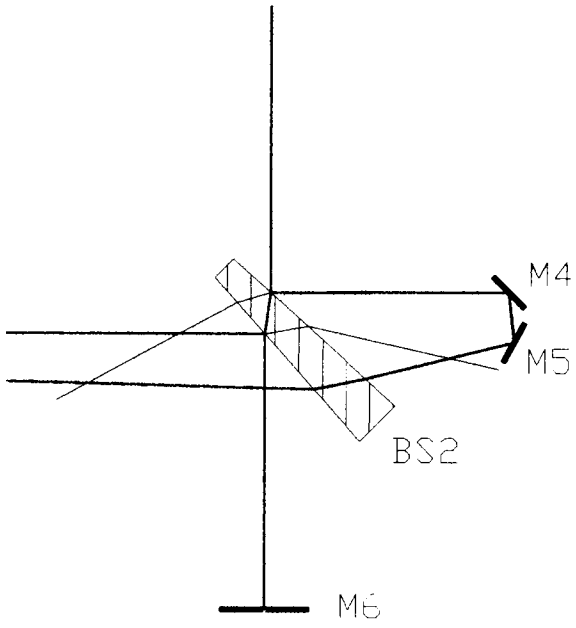

Figure 6.2: Detailed arrangement of the beam paths at the wedge.

is controlled by the use of a personal computer.

6.3 Experimental Results

In an individual experimental run, the two beam's temporal overlap was scanned, i.e., the step translator was moved to different positions and the images were recorded at the different positions. The images were stored and were analyzed subsequently, although real-time recording/analyzing could be possible in principle. The translation stage was moved by a distance, $d/2$, in 0.5 μm steps which corresponds to a time-delay, d/c, of approximately 3.3 fs. The resolution of the translation stage is specified to be 0.1 μm with an accuracy of 2.5 μm per 25 mm of travel. For an overall linear travel distance of 100 μm, an inaccuracy of at most 0.01 μm is inferred, i.e., 0.03 fs for time-delay. The angle between the two beams was adjusted to 0.5°. During a 5 ms camera exposure time, interference patterns of approximately 380,000 laser pulses are generated. The individual images represent an average obtained from 380,000 spatio-temporal pulse superpositions.

Figure 6.3 displays two typical recorded images. These images were recorded in two individual experimental runs. Each image consists of 753×244 8-bit data. Only a small portion of the interference pattern is recorded in the top image and it shows details of the fringes. The bottom picture shows the majority of the interference pattern. In the experimental runs with the larger magnification the zoom lens was adjusted to a $\times 6$ larger than for the small magnification experimental runs. Both images were recorded for approximately zero time delay between the two beams.

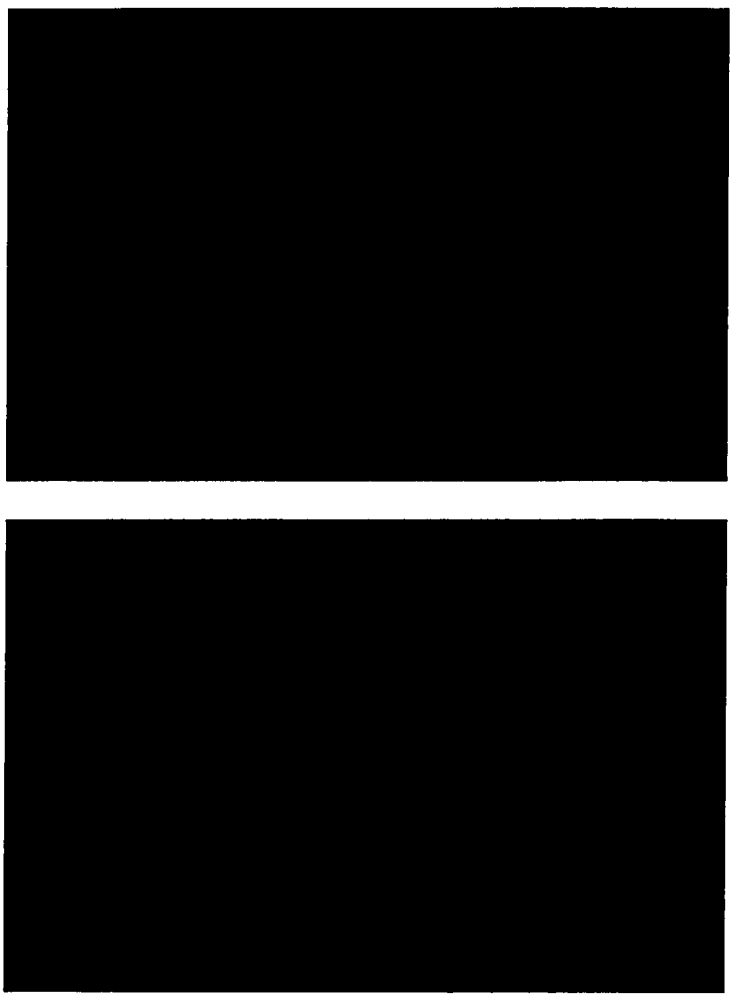

Figure 6.3: Images of interference patterns. The camera lens magnification used is $\times 6$ larger for (a) top image than (b) bottom image.

6.4 Short-Pulse Interference Details

In this section the intensity distribution in the overlap region of the two beams is derived. The classical electromagnetic theory is used in the analysis of ultra-short pulse interference.

First we formulate the electric field of a laser pulse that propagates in the $\hat{\mathbf{z}}$ direction. In this formulation we use a wave packet, [70]

$$E(t,\mathbf{x}) \;=\; A(\mathbf{x})\int_{-\infty}^{\infty} F(\omega-\omega_0)e^{-i(\omega t-\mathbf{k}\cdot\mathbf{x})}d\omega. \tag{6.1}$$

Here, $\mathbf{k}$ is the wave vector $\mathbf{k}=\hat{\mathbf{k}}\dfrac{\omega}{c}$, c is the speed of light and $\hat{\mathbf{k}}$ is the unit vector in the $\mathbf{k}$ direction ($\mathbf{k}\uparrow\uparrow\hat{\mathbf{z}}$). $F(\omega-\omega_0)$ describes the spectral distribution of the wave packet centered at ω_0, with the usual normalization

$$\int_{-\infty}^{\infty}|F(\omega-\omega_0)|^2d\omega=1. \tag{6.2}$$

The complex, spatial amplitude, $A(x)$, satisfies the spatial part of the wave equation, [71]

$$\nabla^2A(\mathbf{x})-2ik\frac{\partial A(\mathbf{x})}{\partial z}=0. \tag{6.3}$$

In the paraxial approximation, the laser beam distribution $A(x)$ can be described by a Gaussian beam that propagates along the $\hat{\mathbf{z}}$ direction. [72]

Next we define the Fourier transform, f, of the spectral distribution F as:

$$f(t-\hat{\mathbf{k}}\cdot\mathbf{x}/c)=\int_{-\infty}^{\infty}F(\omega-\omega_0)e^{-i(\omega-\omega_0)(t-\hat{\mathbf{k}}\cdot\mathbf{x}/c)}d\omega, \tag{6.4}$$

with f also normalized to unity,

$$\int_{-\infty}^{\infty} |f(t - \hat{\mathbf{k}} \cdot \mathbf{x}/c)|^2 dt = 1, \tag{6.5}$$

because of the unitary property of Fourier transforms. By the use of the Fourier transform Eq. (6.4), the electric field becomes

$$E(t, \mathbf{x}) = A(\mathbf{x}) f(t - \hat{\mathbf{k}} \cdot \mathbf{x}/c) e^{-i\omega_0(t - \hat{\mathbf{k}} \cdot \mathbf{x}/c)}. \tag{6.6}$$

Now we proceed to describe the interference of two beams. The two beams of identical, linear polarization propagate in directions $\hat{\mathbf{k}}_1$ and $\hat{\mathbf{k}}_2$, respectively, and are described by

$$\begin{aligned} E_1(t, \mathbf{x}) &= A_1(\mathbf{x}) f_1(t - \hat{\mathbf{k}}_1 \cdot \mathbf{x}/c) e^{-i\omega_0(t - \hat{\mathbf{k}}_1 \cdot \mathbf{x}/c)}, \\ E_2(t, \mathbf{x}) &= A_2(\mathbf{x}) f_2(t - \hat{\mathbf{k}}_2 \cdot \mathbf{x}/c - d/c) e^{-i\omega_0(t - \hat{\mathbf{k}}_2 \cdot \mathbf{x}/c - d/c)}. \end{aligned}$$

The time delay between beam 1 and 2 equals d/c. In the overlap region of the two laser beams, the electric field is the sum of the individual fields,

$$\begin{aligned} E(t, \mathbf{x}) &= E_1(t, \mathbf{x}) + E_2(t, \mathbf{x}) \\ &= A_1(\mathbf{x}) f_1(t - \hat{\mathbf{k}}_1 \cdot \mathbf{x}/c) e^{-i\omega_0(t - \hat{\mathbf{k}}_1 \cdot \mathbf{x}/c)} \\ &+ A_2(\mathbf{x}) f_2(t - \hat{\mathbf{k}}_2 \cdot \mathbf{x}/c - d/c) e^{-i\omega_0(t - \hat{\mathbf{k}}_2 \cdot \mathbf{x}/c - d/c)}. \end{aligned} \tag{6.7}$$

The intensity of the total electric field is:

$$\begin{aligned} I(t, \mathbf{x}) &= E(t, \mathbf{x}) E^*(t, \mathbf{x}) \\ &= |A_1(\mathbf{x}) f_1(t - \hat{\mathbf{k}}_1 \cdot \mathbf{x}/c)|^2 + |A_2(\mathbf{x}) f_2(t - \hat{\mathbf{k}}_2 \cdot \mathbf{x}/c - d/c)|^2 \\ &+ 2\Re e \left\{ A_1(\mathbf{x}) A_2^*(\mathbf{x}) f_1(t - \hat{\mathbf{k}}_1 \cdot \mathbf{x}/c) f_2^*(t - \hat{\mathbf{k}}_2 \cdot \mathbf{x}/c - d/c) e^{i\omega_0((\hat{\mathbf{k}}_1 - \hat{\mathbf{k}}_2) \cdot \mathbf{x}/c - d/c)} \right\}. \end{aligned} \tag{6.8}$$

The two pulses are assumed to have identical pulse shape subsequently. This assumption is valid provided the optical lengths of the two short pulses in a dispersive medium are equal. The temporal pulse shape for both beams is described by $f(t)$, i.e., the subscripts for the pulse shapes $f_1(t)$ and $f_2(t)$ can be omitted. Then, the intensity of the summed electric field becomes:

$$\begin{aligned} I(t,\mathbf{x}) &= |A_1(\mathbf{x})f(t-\hat{\mathbf{k}}_1\cdot\mathbf{x}/c)|^2 + |A_2(\mathbf{x})f(t-\hat{\mathbf{k}}_1\cdot\mathbf{x}/c+\tau(\mathbf{x})|^2 \\ &+ 2\Re e\left\{A_1(\mathbf{x})A_2^*(\mathbf{x})f(t-\hat{\mathbf{k}}_1\cdot\mathbf{x}/c)f^*(t-\hat{\mathbf{k}}_1\cdot\mathbf{x}/c+\tau(\mathbf{x}))e^{i\omega_0\tau(\mathbf{x})}\right\}, \end{aligned}$$

where the spatially dependent time-delay is

$$\tau(\mathbf{x}) = (\hat{\mathbf{k}}_1-\hat{\mathbf{k}}_2)\cdot\mathbf{x}/c - d/c. \tag{6.9}$$

The interference intensity is integrated during each pulse in the ultra-short pulse interference measurements. The integration limits are extended to positive and negative infinity since the interval between subsequent pulses is more than five orders of magnitude larger than the pulse width. The integrated intensity, denoted by $\Pi(\mathbf{x})$, is calculated to be

$$\begin{aligned} \Pi(\mathbf{x}) &= \int_{-\infty}^{\infty} I(t,\mathbf{x})dt \\ &= |A_1(\mathbf{x})|^2\int_{-\infty}^{\infty}|f(t-\hat{\mathbf{k}}_1\cdot\mathbf{x}/c)|^2dt \\ &+ |A_2(\mathbf{x})|^2\int_{-\infty}^{\infty}|f(t-\hat{\mathbf{k}}_1\cdot\mathbf{x}/c+\tau(\mathbf{x})|^2dt \\ &+ 2\Re e\left\{A_1(\mathbf{x})A_2^*(\mathbf{x})\int_{-\infty}^{\infty}f(t-\hat{\mathbf{k}}_1\cdot\mathbf{x}/c)f^*(t-\hat{\mathbf{k}}_1\cdot\mathbf{x}/c+\tau(\mathbf{x}))dte^{i\omega_0\tau(\mathbf{x})}\right\} \\ &= |A_1(\mathbf{x})|^2+|A_2(\mathbf{x})|^2+2\Re e\left\{A_1(\mathbf{x})A_2^*(\mathbf{x})g(\tau(\mathbf{x}))e^{i\omega_0\tau(\mathbf{x})}\right\}, \end{aligned} \tag{6.10}$$

where we have used that the temporal pulse-shapes are normalized. Also, the spatially dependent autocorrelation function $g(\tau(\mathbf{x}))$ of f is defined by

$$g(\tau) = \int_{-\infty}^{\infty} f(t) f^*(t+\tau) dt. \tag{6.11}$$

The interference cross term (third term in Eq. (6.10)) is proportional to the first-order correlation function which is equal to the autocorrelation function for identical temporal pulse shapes of the two beams. The autocorrelation function depends on the time delay d/c of the two beams and it also depends on the time delay that varies spatially according to $(\hat{\mathbf{k}}_1 - \hat{\mathbf{k}}_2) \cdot \mathbf{x}/c$.

6.5 Determination of the Autocorrelation Function

Fourier transform techniques are utilized to separate the interference cross term from the other contributions in the spatial frequency domain. [30, 31, 32] The terms $|A_1(\mathbf{x})|^2$ and $|A_2(\mathbf{x})|^2$ are transformed only into the domain of low spatial frequency. The interference cross term is transformed into the domain of high spatial frequency mainly due to the component $e^{i\omega_0 \tau(\mathbf{x})}$. Therefore, we consider only the interference cross term in following derivation,

$$\Pi_{12}(\mathbf{x}) = 2\Re e \left\{ A_1(\mathbf{x}) A_2^*(\mathbf{x}) g(\tau(\mathbf{x})) e^{i\omega_0 \tau(\mathbf{x})} \right\}. \tag{6.12}$$

By using Eq. (5.22), the Fourier transform in x-y plane, denoted by $\mathbf{x}_\perp$, of the interference cross term is:

$$\xi(\kappa) = \int_{-\infty}^{\infty} \int_{-\infty}^{\infty} \Pi_{12}(\mathbf{x}) e^{i\kappa \cdot \mathbf{x}_\perp} d\mathbf{x}_\perp$$

$$
\begin{aligned}
&= \int_{-\infty}^{\infty}\int_{-\infty}^{\infty} 2\Re e\left\{A_1(\mathbf{x})A_2^*(\mathbf{x})g(\tau(\mathbf{x}))e^{i\omega_0\tau(\mathbf{x})}\right\}e^{i\kappa\cdot\mathbf{x}_\perp}d\mathbf{x}_\perp \\
&= \int_{-\infty}^{\infty}\int_{-\infty}^{\infty} A_1(\mathbf{x})A_2^*(\mathbf{x})g(\tau(\mathbf{x}))e^{i\omega_0((\hat{\mathbf{k}}_1-\hat{\mathbf{k}}_2)\cdot\mathbf{x}/c-d/c)}e^{i\kappa\cdot\mathbf{x}_\perp}d\mathbf{x}_\perp \qquad (6.13) \\
&+ \int_{-\infty}^{\infty}\int_{-\infty}^{\infty} A_1^*(\mathbf{x})A_2(\mathbf{x})g^*(\tau(\mathbf{x}))e^{-i\omega_0((\hat{\mathbf{k}}_1-\hat{\mathbf{k}}_2)\cdot\mathbf{x}/c-d/c)}e^{i\kappa\cdot\mathbf{x}_\perp}d\mathbf{x}_\perp
\end{aligned}
$$

in the frequency domain, Equation (6.13) represents two peaks at $\kappa^I = (\hat{\mathbf{k}}_2 - \hat{\mathbf{k}}_1)\omega_0/c$ and $\kappa^{II} = (\hat{\mathbf{k}}_1 - \hat{\mathbf{k}}_2)\omega_0/c$. The peak at κ^I can be isolated by using an appropriate filter, and one obtains

$$
\xi^I(\kappa) = \int_{-\infty}^{\infty}\int_{-\infty}^{\infty} A_1(\mathbf{x})A_2^*(\mathbf{x})g(\tau(\mathbf{x}))e^{i\omega_0((\hat{\mathbf{k}}_1-\hat{\mathbf{k}}_2)\cdot\mathbf{x}/c-d/c)}e^{i\kappa\cdot\mathbf{x}_\perp}d\mathbf{x}_\perp. \qquad (6.14)
$$

The inverse Fourier transform of the peak is:

$$
\mathcal{F}^{-1}(\xi^I) = A_1(\mathbf{x})A_2^*(\mathbf{x})g(\tau(\mathbf{x}))e^{i\omega_0((\hat{\mathbf{k}}_1-\hat{\mathbf{k}}_2)\cdot\mathbf{x}/c-d/c)}. \qquad (6.15)
$$

The autocorrelation function $g(\tau)$ may be determined from one image (for a relative time delay of approximately zero) for known $A_1(\mathbf{x})A_2^*(\mathbf{x})$. For an accurate measurement of $g(\tau(\mathbf{x}))$, the spatial frequency distribution of $g(\tau(\mathbf{x}))$ must be significantly broader than the spatial frequency distribution of $A_1(\mathbf{x})A_2^*(\mathbf{x})$. Equivalently, for approximately constant $A_1(\mathbf{x})A_2^*(\mathbf{x})$ and for sufficient temporal variation due to the term of the spatial time-delay, $(\hat{\mathbf{k}}_1 - \hat{\mathbf{k}}_2)\cdot\mathbf{x}/c$, across the detector surface, the autocorrelation function is proportional to the envelope of the fringe maxima, i.e., the visibility of fringes.

The determination of the autocorrelation function with the time-delay method is elaborated in the following. For each image recorded at a set time delay between the two beams, one integrates the intensity contribution of one interference peak in

frequency domain (the κ space). The integration limit is extended to $\pm\infty$ since the integration of the intensity contribution of one peak in the region beyond 3 times full width from the peak center is negligible. By direct substitution or by the use of the Wiener-Kintchine theorem (see Eq. (5.8)), one obtains

$$\begin{aligned}\Xi(d/c) &= \int_{-\infty}^{\infty}\int_{-\infty}^{\infty}\xi_i^I(\kappa)\xi_i^I(\kappa)^* d\kappa \\ &= 4\pi^2\int_{-\infty}^{\infty}\int_{-\infty}^{\infty}|A_1(\mathbf{x})A_2^*(\mathbf{x})g((\hat{\mathbf{k}}_1-\hat{\mathbf{k}}_2)\cdot\mathbf{x}/c-d/c)|^2 d\mathbf{x}_\perp. \quad (6.16)\end{aligned}$$

This results shows that the square of the autocorrelation function is convolved with the square of the amplitude distributions. A temporal distribution $\Xi(d/c)$ is obtained as function of the time delay d/c due to the spatial integration. The Fredholm integral equation (Eq. (6.16)) can be inverted by the application of standard mathematical methods, i.e., by the use of the Fourier convolution theorem, [33]

$$|g(d/c)|^2 = \frac{1}{4\pi^2}\mathcal{F}^{-1}\left\{\mathcal{F}\{\Xi\}/\mathcal{F}\{|A_1A_2^*|^2\}\right\}. \quad (6.17)$$

This additional Fourier transform is not used in the analysis of the recorded images.

Now we consider measured image data represented by a two dimensional array. Each array element, h_{pq}, is the integrated intensity over the corresponding pixel. For the array elements one can write

$$h_{pq} = \Pi(\mathbf{x}_{pq})\Delta_1\Delta_2 \qquad 1\le p\le M, \qquad 1\le q\le N, \quad (6.18)$$

where Δ_1 and Δ_2 are the pixel sizes in the two perpendicular directions. The total area of the image is $a\times b$. The intensity of the electric field at the point $\mathbf{x}_{pq}$ may be of the same order as that in Eq. (6.18) for the interference pattern outside the recorded

image region. However, in the numerical analysis the array values h_{pq} are set to zero outside the active area of the camera. Output correction in κ space due to this filter can be calculated as discussed in Section 5.4 (see Eq. (5.19)). The corrections are negligible for the applied filter. Setting h_{pq} to zero outside the recorded area is equivalent with setting $A_1(\mathbf{x})A_2^*(\mathbf{x})$ to zero. Consequently, one can write for the temporal distribution $\Xi(d/c)$,

$$\Xi(d/c) \;=\; 4\pi^2 \int_0^a \int_0^b |A_1(\mathbf{x})A_2^*(\mathbf{x})g((\hat{\mathbf{k}}_1 - \hat{\mathbf{k}}_2)\cdot\mathbf{x}/c - d/c)|^2 d\mathbf{x}_\perp. \qquad (6.19)$$

$|g(d/c)|^2$ may be obtained by inverting this integral equation. However, if the amplitude terms can be modeled by a 2-dimensional δ-distribution, the spatial integration would yield that the temporal distribution $\Xi(d/c)$ is directly proportional to the square of the autocorrelation function. The use of a δ-distribution is justified for widths $|A_1(\mathbf{x})A_2^*(\mathbf{x})|^2$ much narrower than the width of $|g(\tau(\mathbf{x}))|^2$. The temporal distribution $\Xi(d/c)$ will also be approximately proportional to the square of the autocorrelation function for a range of the spatial time-delay, $(\hat{\mathbf{k}}_1 - \hat{\mathbf{k}}_2)\cdot\mathbf{x}/c$, that is small compared to the width of the autocorrelation function.

The numerical analysis of Eq. (6.19) is presented in the following. It is assumed that the two beams propagate in the directions (sin $\frac{\theta}{2}$, 0, cos $\frac{\theta}{2}$) and (-sin $\frac{\theta}{2}$, 0, cos $\frac{\theta}{2}$), respectively, where θ is the angle between the two beams. The temporal distribution $\Xi(d/c)$ is:

$$\Xi(d/c) \;=\; \int_0^a \left[4\pi^2 \int_0^b |A_1(\mathbf{x})A_2^*(\mathbf{x})|^2 dy\right] |g(\frac{2x}{c}\sin\frac{\theta}{2} - \frac{d}{c})|^2 dx. \qquad (6.20)$$

In numerical analysis, a normalized, centered Gaussian is assumed for the amplitude

contribution (term in square brackets),

$$4\pi^2 \int_0^b |A_1(\mathbf{x})A_2^*(\mathbf{x})|^2 dy = \frac{C}{w} e^{-(x-a/2)^2/w^2}, \tag{6.21}$$

where C is a proportionality constant and w is the width of the Gaussian. For small width w compared to the horizontal image dimension a, this Gaussian can be viewed as a representation of a one-dimensional δ-distribution.

The autocorrelation function, defined in Eq.(6.11), for a hyperbolic secant temporal pulse shape equals

$$|g(\tau)| = \frac{\tau/t_w}{e^{\tau/t_w} - e^{-\tau/t_w}}. \tag{6.22}$$

This result can be obtained from the assumed temporal, hyperbolic-secant pulse shape,

$$|f(t)| = \frac{2}{e^{t/t_w} + e^{-t/t_w}}, \tag{6.23}$$

where t_w is the width of the hyperbolic secant. This width is related to the pulse-width t_p (FWHM of the square of the pulse profile $|f|^2$) by $t_p = 1.76t_w$. One obtains for the temporal distribution $\Xi(d/c)$,

$$\Xi(d/c) \;=\; \int_0^a \frac{C}{w} e^{-(x-a/2)^2/w^2} |g(2x \sin\frac{\theta}{2}/c - d/c)|^2 dx, \tag{6.24}$$

and in terms of the variables $x' = \frac{2x}{c}\sin\frac{\theta}{2}$, $a' = \frac{2a}{c}\sin\frac{\theta}{2}$ and $w' = \frac{2w}{c}\sin\frac{\theta}{2}$, one finds

$$\Xi(d/c) \;=\; \int_0^{a'} \frac{C}{w'} e^{-(x'-a'/2)^2/w'^2} |g(x' - d/c)|^2 dx'. \tag{6.25}$$

Figure 6.4 shows the temporal distribution $\Xi(d/c)$ for the integration limits of $a' = 17$ fs and $a' = 100$ fs (corresponding to the large and small magnification experiments, respectively) and for different width w'. The solid curve shows the temporal profile $\Xi(d/c)$ for $w' = 0$, i.e., this temporal distribution is proportional to the square of the autocorrelation function as the Gaussian profile approaches a δ-distribution. Differences are negligible for $a' = 17$ fs because the integration range is small compared to the width of the square of the autocorrelation function. This result is almost independent of the width w' for the amplitude distributions. However, for $a' = 100$ fs broadening effect of the temporal distribution $\Xi(d/c)$ would be noticeable if the width w' were larger than 50 fs. For the small magnification experiments, the width w' is approximately 20 fs which results in a broadening of 1 fs for the pulse width t_p.

6.6 Analysis of Experimental Results

The analysis of the recorded images is accomplished by the use of discrete Fourier transforms for the finite image which is represented by a two dimensional array, (h_{pq}), as indicated in Eq. (6.18). In the numerical analysis we use Nyquist critical frequencies $\kappa_{1c} = \frac{\pi}{\Delta_1}$ and $\kappa_{2c} = \frac{\pi}{\Delta_2}$. The value of $H(\kappa)$ at the position $\kappa_1 = \frac{m}{M}\kappa_{1c}$ and $\kappa_2 = \frac{n}{N}\kappa_{2c}$, denoted by H_{mn}, is given by the discrete Fourier transform of the set $\{h_{pq}\}$,

$$H_{mn} = \sum_{p=0}^{M-1} \sum_{q=0}^{N-1} h_{pq} e^{2\pi i p m/M} e^{2\pi i q n/N}. \tag{6.26}$$

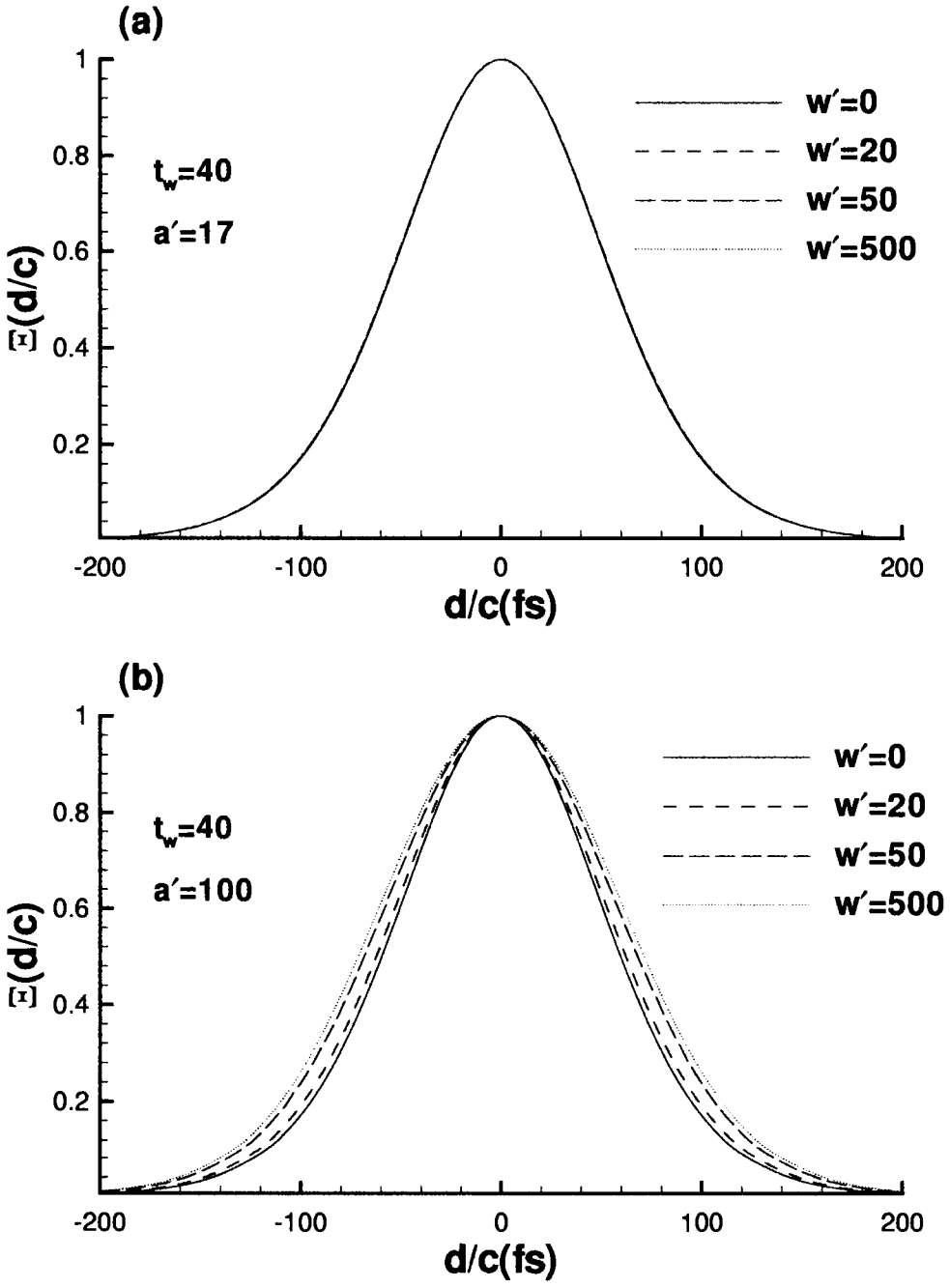

Figure 6.4: Comparison of the temporal distribution $\Xi(d/c)$ and the square of the autocorrelation function for different effective width w': (a) $a' = 17$ fs; (b) $a' = 100fs$.

The discrete Fourier transform is computed by the use of fast Fourier transform algorithm. [36] The upper limits of the sum in Eq. (6.26) must be set to numbers of power of 2 in the fast Fourier transform algorithm.

Figure 6.5(a) shows a portion of the intensity distribution $\mathcal{F}(\Pi)\mathcal{F}^*(\Pi)$ which corresponds to the small magnification experiment shown in Fig. 6.3(b). The first two terms of Eq. (6.10) are included in the peak near the origin. Figure 6.5(b) shows details of the interference peak near the pair ($m = 0$, $n = 50$). In principle, we may obtain the parameters of the laser pulse from this peak. However, it is not feasible to obtain accurate information of the autocorrelation function from this peak since $|A_1(\mathbf{x})A_2^*(\mathbf{x})|$ shows broader spatial frequency than $g(\tau(\mathbf{x}))$. We integrate the intensity near the peak to obtain $\Xi(d/c)$ at time delay d/c. In the numerical evaluation of the temporal distribution $\Xi(d/c)$, the integration over κ reduces to a summation over m and n of discrete values $H_{mn}H_{mn}^*$ near the pair $(0, 50)$, i.e., in the restricted domain (m, n) that corresponds to one of the interference cross terms for the used filter.

Figure 6.6 shows the square of the autocorrelation function, which is approximately proportional to the temporal distribution $\Xi(d/c)$ (or the results of the above mentioned summation), versus time delay. The approximation is valid for both experiments according to the numerical analysis discussed in previous section. The effective range a' is approximately 17 fs for the large magnification experiment. The effective range a' is approximately 100 fs and the effective width w' is about 20 fs for the small magnification experiment. The effective range a' is determined by the

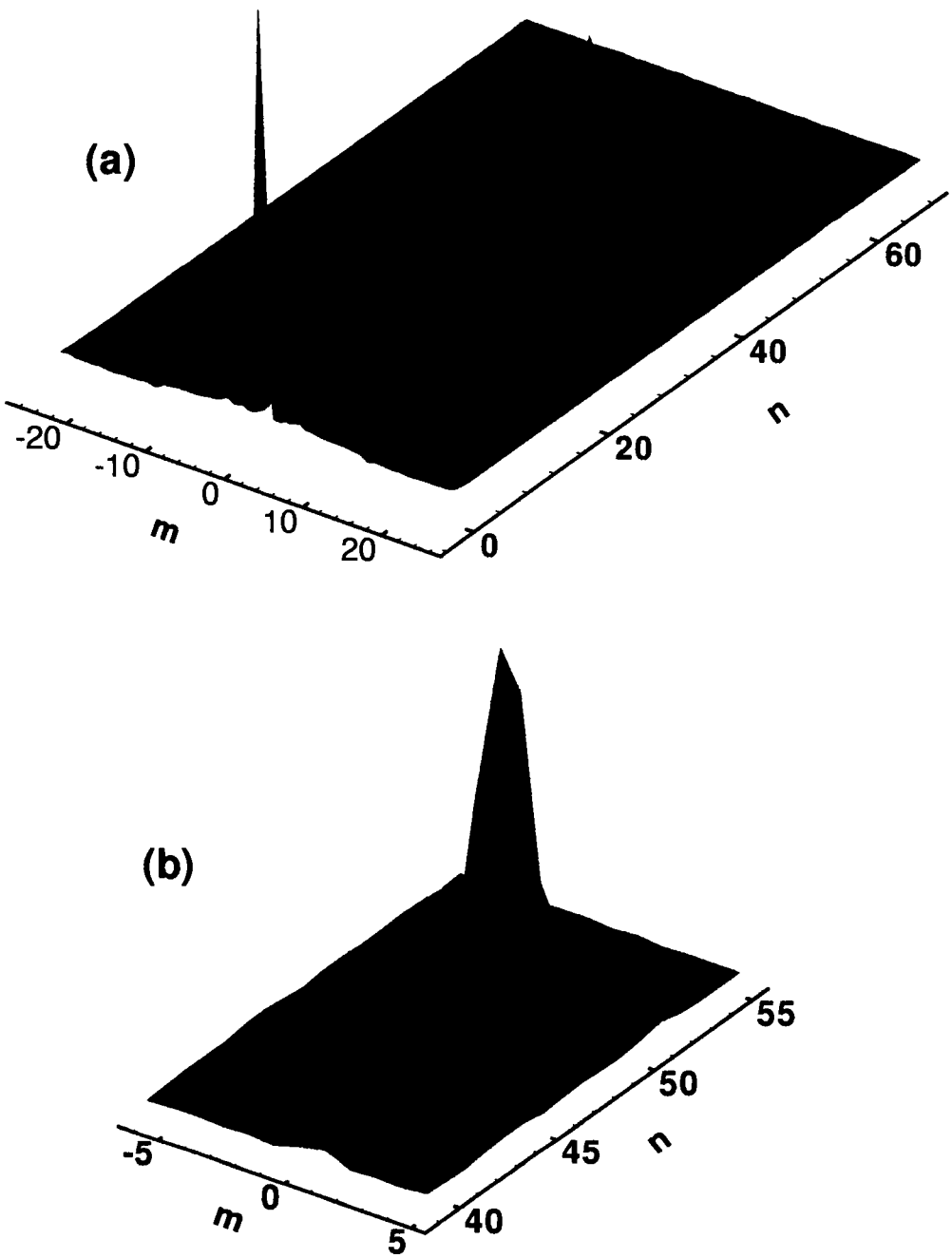

Figure 6.5: Spatial frequency distribution of the recorded images: (a) Fourier transform of the intensity distribution; (b) detailed view of the interference cross term near the pair ($m = 0$, $n = 50$).

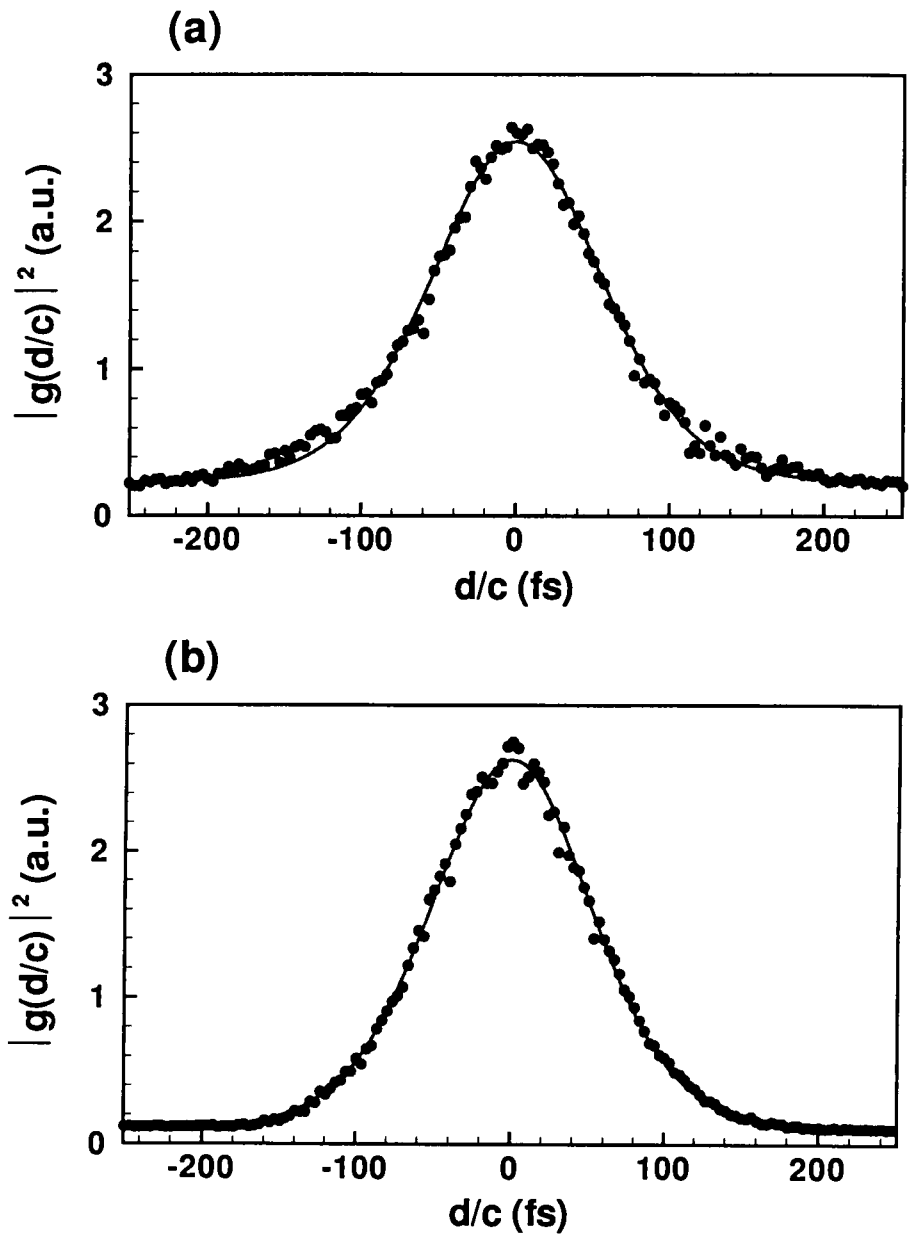

Figure 6.6: Measured (circles) and fitted temporal distribution, or square of the scaled autocorrelation function, for a hyperbolic-secant temporal pulse-shape versus time delay d/c: (a) large magnification; (b) small magnification.

angle between the beams and the camera area. It can also be estimated from the interference images by multiplying the number of fringes with the duration of an optical cycle, for example, 36×2.9 fs $\simeq 100$ fs for the small magnification experiments. The effective width w' may be determined from the beam's intensity distributions. The square of the autocorrelation function can be obtained by the use of smoothing algorithms. The width t_w is determined by fitting the experimental data with $C_1 + C_2|g(\tau)|^2$ where $g(\tau)$ is assumed to be the autocorrelation function of the hyperbolic secant pulse (see Eq. (6.22) and (6.23)). The least-square method is applied in the data fitting. The fitting curves are also shown in Fig. 6.6. The fitting results of t_w are 44 fs and 42 fs, respectively.

The FWHM of the laser pulses are obtained from the intensity profile $|f|^2$. The laser pulse widths t_p (FWHM) amount to 77 fs and 72 fs, respectively. Note that these results are obtained from different experimental runs. The error bars are estimated from the distribution of the autocorrelation coefficients to be at most 5% for the pulse width t_p. Smaller error bar result for the smaller magnification experiments. This can be seen, for example, by comparing the wings of the profiles in Fig. 6.6. The discrete Fourier transform can be more precisely determined from approximately 36 fringes (small magnification) than for 6 fringes (large magnification) for each time delay. Lens aberration effects will also be smaller when using a smaller magnification of the zoom lens. The 5 fs disparity is attributed to the different pulse-width that was available for the separate experimental runs. Broadening from the convolution process is insignificant for an angle of 0.5° between the beams, the recorded horizontal

image dimensions of 0.6 mm and 3.6 mm, respectively, and for pulse widths of approximately 70 fs. The broadening would amount to 0.5% and 1.5%, or 0.3 fs and 1 fs, respectively.

Finally, it is discussed how many data are sufficient to describe the measurement of the autocorrelation function. In the performed experiments, about 200 images are recorded in a scan of 663 fs. The autocorrelation is a special type of Fredholm integral equation for the pulse profile. The kernel function is also the pulse profile. The same eigen-analysis is performed as in Chapter 2 for the hyperbolic secant kernel. The covariant matrix of the kernel is computed and the eigenvalues of the covariant matrix are found. Figure 6.7 show the eigenvalue and the relative information versus the number of the eigenvalue. From the diagram, about 16 data are independent. Therefore, only 16 images are required to describe the autocorrelation function in a scan of 1000 fs.

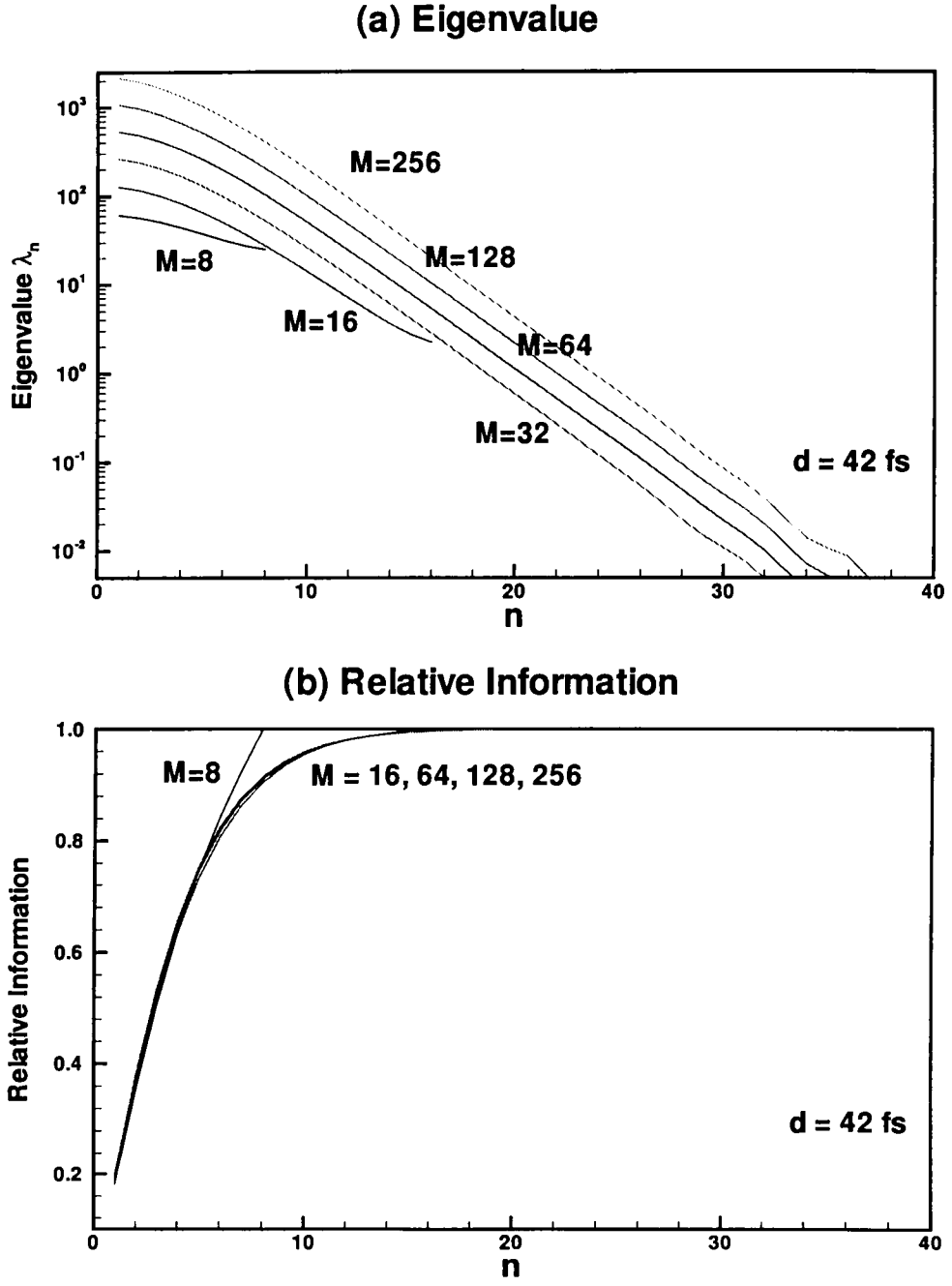

Figure 6.7: Eigenvalues and relative information for hyperbolic secant kernels: fixed range from -500 fs to 500 fs, and fixed interval d=42 fs.

Chapter 7

Summary and Conclusions

In this dissertation, emission spectra and interference images were analyzed. It was found that a detailed investigation is important for the evaluation of spectroscopic temperature and laser pulse width, respectively.

Measurement of data usually involves integration. The quantity of interest is in the integrand, therefore, one needs to solve an integral equation. Of interest are the Fredholm integral equation of the first kind since the formal dependencies of the data can be put in this form. The eigen-analysis technique is utilized to determine the interdependency of the kernels. The technique of singular value decomposition should be utilized in the inversion of the Fredholm integral equation for nonorthogonal kernels. Three kinds of nonorthogonal kernels were investigated with the eigen-analysis technique. The results are summarized below. For Gaussian kernels, the significant number of data is about 1.25 times of the data range divided by FWHM of Gaussian kernel. For sinc function kernels, the significant number of data is about 1.11 times of the data range divided by FWHM of sinc kernel. For hyperbolic secant function kernels, the significant number of data is about 1.76 times of the data range

divided by FWHM of the hyperbolic secant kernel. The information contained in the measurement with a special type of kernel is restricted because of resolution of the kernel. A significant number of data contains over 99% information that can be measured by that type of kernel. The data should be equally spaced for these three types of kernel.

Alternatively, least-square fitting is often used in data analysis. One usually has a model of the quantity of interest prior to least-square fitting. Different weights in merit function are defined depending on the data set. The correlation coefficients and the error propagation equations can be deduced in the parabolic approximation. Generally Monte Carlo simulation may be used to investigate the correlation and accuracy of parameters.

Several simple models of spectral data are assumed and investigated numerically. The investigations emphasized the study of the error propagation and the correlation between parameters. These simple models of data help to understand the results of complex spectral data.

Emission spectra after laser-induced breakdown of air are investigated. The NEQAIR code can be used to provide an overview of the emission spectra. It is found that OH contributions dominate the emission spectra in the range of 305-322 nm when the temperature of the emission source is below 5000 K. Therefore, the emission spectra are fitted with the OH synthetic emission spectra by using the least-square method. The rotation-vibration temperature is obtained from the fitting. The correlation and precision of the fitting parameters are studied by using

Monte Carlo simulations. The background emission is strongly correlated with temperature while the line shape has hardly any effect in the spectroscopic temperature determination. The errors in the estimation by least-square fitting are proportional to the error magnitude used in Monte Carlo simulations.

An important technique in image analysis is Fourier transform. Fourier transform converts image information between space and spatial frequency. Related topics, such as discrete Fourier transform, sampling theorem and filter, are discussed.

Interference patterns of two time-delayed beams are recorded by using a CCD camera. The Fourier transform is used to convert the image data to the domain of spatial frequencies. The interference components are separated from the background in the spatial frequency domain. The autocorrelation function, and consequently the pulse width for an assumed pulse shape is determined from these interference components. In this dissertation, the autocorrelation function for nominally 70 fs laser pulses is obtained by scanning the overlap of two beams. However, it is possible to obtain the autocorrelation function from one image. The pulse width is determined by fitting the autocorrelation function with a model autocorrelation function in which the hyperbolic secant is assumed as the pulse shape. Usually more than 100 images are recorded to obtain a complete autocorrelation function. However, 16 images are sufficient to describe the measurement.

Bibliography

Bibliography

[1] Stuart L. Meyer. *Data Analysis for Scientists and Engineers.* John Wiley & sons, Inc., second edition edition, 1975.

[2] Philip R. Bevington and D. Keith Robinson. *Data Reduction and Error Analysis for the Physical Sciences.* McGraw-Hill, Inc., Case Western Reserve Univ., second edition edition, 1992.

[3] C. W. Groetsch. *The Theory of Tikhonov Regularization for Fredholm Equations of the First Kind.* Pitman Advanced Published Program, University of Cincinnati, 1984.

[4] Henry Stark. *Image Recovery Theory and Application.* Academic Press, Inc., Rensselaer Polytechnic Institute, Troy, New York, 1987.

[5] S. Twomey. *Introduction to the Mathematics of Inversion in Remote Sensing and Indirect Measurements.* American Elsevier, 1977.

[6] S. Twomey. "Information Content in Remote Sensing". *Applied Optics,* 13(4):942–945, 1974.

[7] J. Y. Wang and R. Goulard. "Numerical Solutions in Remote Sensing". *Applied Optics*, 14(4):862–871, 1975.

[8] J. Heintzenberg, H. Muller, H. Quenzel, and E. Thomalla. "Information Content of Optical Data with respsect to Aerosol Properties: Numerical Studies with a Randomized Minimization-Search-Technique Inversion Algorithm". *Applied optics*, 20(8):1308–1315, 1981.

[9] C. D. Capps, R. L. Henning, and G. M. Hess. "Analytic Inversion of Remote-Sensing Data". *Applied Optics*, 21(19):3581–3586, 1982.

[10] G. Viera and M. A. Box. "Information Content Analysis of Aerosol Remote-Sensing Experiments Using an Analytic Eigenfunction Theory: Anomalous Diffraction Approximation". *Applied Optics*, 24(24):4525–4533, 1985.

[11] G. Viera and M. A. Box. "Information Content Analysis of Aerosol Remote-Sensing Experiments Using Singular Function Theory. 1: Extinction Measurements". *Applied Optics*, 26(7):1312–1327, 1987.

[12] G. Viera and M. A. Box. "Information Content Analysis of Aerosol Remote-Sensing Experiments Using Singular Function Theory. 2: Scattering Measurements". *Applied Optics*, 27(15):3262–3273, 1988.

[13] M. A. Box and G. Viera. "Information Content Analysis of Aureole Inversion Methods: Differential Kernel versus Normal". *J. Opt. Soc. Am. A*, 7(6):1015–1018, 1990.

[14] A. Ben-David, B. M. Herman, and J. A. Reagan. "Inverse Problem and the Pseudoempirical Orthogonal Function Method of Solution. 1: Theory". *Applied Optics*, 27(7):1235–1242, 1988.

[15] A. Ben-David, B. M. Herman, and J. A. Reagan. "Inverse Problem and the Pseudoempirical Orthogonal Function Method of Solution. 2: Use". *Applied Optics*, 27(7):1243–1254, 1988.

[16] Feng Sun. *"Optical Measurement of Particle Size Distribution Function Using Downhill Simplex Method: Theory and Experiment"*. PhD thesis, The University of Tennessee Space Institute, 1994.

[17] David R. Crosley and Jay B. Jeffries. "Temperature Measurements by Laser-induced Fluorescence of the Hydroxyl Radical". In *Temperature: Its Measurement and Control in Science and Industry*, volume 6, pages 701–704, New York, 1992. American Institute of Physics.

[18] P. Desgroux and M. J. Cottereau. "Local OH Concentration Measurement in Atmospheric Pressure Flames by a Laser-saturated Fluorescence Method: Two-optical path Laser-induced Fluorence". *Applied Optics*, 30(1):90–97, 1991.

[19] K. Kohse-Hoinghaus, U. Meier, and B. Attal-Tretout. "Laser-induced Fluorescence Study of OH in Flat Flames of 1-10 Bar Compared with Resonance CARS Experiments". *Applied Optics*, 29(10):1560–1569, 1990.

[20] A. A. Neuber, J. Janicka, and E. P. Hassel. "Thermally Assisted Fluorescence of Laser-excited OH $A^2\Sigma^+$ as a Flame Diagnostic Tool". *Applied Optics*, 35(21):4033–4040, 1996.

[21] J. M. Seitzman, R. K. Hanson, P. A. DeBarber, and C. F. Hess. "Application of Quantitative Two-line OH Planar Laser-induced Fluorescence for Temporally Resolved Planar Thermometry in Reacting Flows". *Applied Optics*, 33(18):4000–4012, 1994.

[22] J. L. Palmer and R. K. Hanson. "Temperature Imaging in a Supersonic Free Jet of Combustion Gases with Two-line OH Fluorescence". *Applied Optics*, 35(3):485–499, 1996.

[23] C. Parigger, J. W. L. Lewis, D. H. Plemmons, G. Guan, and J. O. Hornkohl. "Hydroxyl measurements in air-breakdown microplasmas". Technical report, 1996 OSA Technical Digest Series: Laser Applications to Chemical and Environmental Analysis, 1996.

[24] G. Guan, C. Parigger, J. O. Hornkohl, and J. W. L. Lewis. "Analysis of molecular emission spectra". Technical report, APS 64th Annual Southeastern Section Meeting, Nashville, TN, November 1997.

[25] J. O. Hornkohl, C. Parigger, and J. W. L. Lewis. "Temperature Measurements From CN Spectra in a Laser-Induced Plasma". *J. Quant. Spectrosc. Transfer*, 46(5):405–411, 1991.

[26] K. H. Burrell. "Error Analysis for Parameters Determined in Nonlinear Least-squares Fits". *American Journal in Physics*, 58(2):160–164, 1990.

[27] C. Park. "Nonequilibrium Air Radiation (NEQAIR) Program: User's Manual". Technical Report NASA TM 86707, NASA Ames Research Center, Moffet Field, CA 94035, 1985.

[28] E. E. Whiting, C. Park, Y. Liu, J. O. Arnold, and J. A. Paterson. "NEQAR96, Nonequilibrium and Equilibrium Radiative Transport and Spectra Program: User's Manual". Technical Report NASA RP-1389, NASA Ames Research Center, Moffet Field, CA 94035, 1996.

[29] James A. Cobbles. "Picosecond Coherene Time Measurement with a Double Slit". *Applied Optics*, 26(19):4048–4051, 1987.

[30] Mitsuo Takeda, Hideki Ina, and Seiji Kobayashi. "Fourier-transform Method of Fringe-pattern Analysis for Computer-based Topography and Interferometry". *J. Opt. Soc. Am.*, 72(1):156–160, 1982.

[31] Jr. W. W. Macy. "Two-dimensional Fringe-pattern Analysis". *Applied Optics*, 22(23):3898–3901, 1983.

[32] Thomas Kreis. "Digital Holographic Interference-phase Measurement using the Fourier-transform Method". *J. Opt. Soc. Am. A*, 3(6):847–855, 1986.

[33] G. Arfken and H. J. Weber. *Mathematical Methods for Physicists.* Academic Press, Inc., Miami Univ., Oxford, Ohio, fourth edition, 1995.

[34] R. W. Hamming. *Numerical Methods for Scientists and Engineers.* McGraw-Hill Book Company, Inc, Bell Telephone Laboratories, 1962.

[35] J. P. Hessler, D. H. Current, and P. J. Ogren. "A New Scheme for Calculating Weights and Describing Correlations in Nonlinear Least-squares Fit". *Computers in Physics*, 10(2):186–199, 1996.

[36] W. H. Press, S. A. Teukolsky, W. T. Vetterling, and B. P. Flannery. *Numerical Recipes in Fortran.* Cambridge University Press, 1992.

[37] Mansoor A. Khan, Charly Allemand, and Thomas W. Eagar. "Noncontact Temperature Measurements. II. Least Squares Based Techniques". *Rev. Sci. Instrum.*, 62(2):403–409, 1991.

[38] S. Gordan and B. McBride. "Computer program for calculation of complex equilibrium compositions, rocket performance, incident and reflected shocks, and Chapman-Jouguet detonations". Interim Revision NASA Report SP-273, NASA Lewis Research Center, 1976.

[39] G. Herzberg. *Molecular Spectra and Molecular Structure: I Spectra of Diatomic Molecules.* D. Van Nostrand Company, Inc., second edition edition, 1950.

[40] Irving L. Chidsey and David R. Crosley. "Calculated Rotational Transition Probabilities for the A-X System of OH". *J. Quant. Spectrosc. Radiat. Transfer*, 23:187–199, 1980.

[41] B. Attal-Tretout, S. C. Schmidt, E. Crete, P. Dumas, and J. P. Taran. "Resonance CARS of OH in High-pressure Flames". *J. Quant. Spectrosc. Radiat. Transfer*, 43(5):351–364, 1990.

[42] J. A. Silver, W. L. Dimpfl, J. H. Brophy, and J. L. Kinsey. "Laser-induced Fluorescence Determination of Internal-state Distribution of OH Produced by H+NO_2 in crossed molecular beams". *J. Chem. Phys.*, 65(5):1811–1822, 1976.

[43] Russell K. Lengel and David R. Crosley. "Energy Transfer in $A^2\Sigma^+$ OH. II. Vibrational". *J. Chem. Phys.*, 68(12):5309–5324, 1978.

[44] David R. Crosley and Gregory P. Smith. "Vibrational Energy Transfer in Laser-excited $A^2\Sigma^+$ OH as a Flame Thermometer". *Applied Optics*, 19(4):517–520, 1980.

[45] T. Nielsen, F. Bormann, M. Burrows, and P. Andersen. "Picosecond Laser-induced Fluorescence Measurement of Rotational Energy Transfer of OH $A^2\Sigma^+(v' = 2)$ in Atmospheric Pressure Flames". *Applied Optics*, 36(30):7960–7969, 1997.

[46] L. Montgomery Smith. *"A Unified Study of the Effects of Aberrations in Focused Laser Beams"*. PhD thesis, The University of Tennessee Space Institute, 1988.

[47] David H. Plemmons. *"Laser-Spark Ignition and the NH Radical"*. PhD thesis, The University of Tennessee Space Institute, 1996.

[48] Ying-Ling A. Chen. *"Laser-Induced Gas Breakdown and Ignigtion"*. PhD thesis, The University of Tennessee Space Institute, 1998.

[49] G. Guan, C. Parigger, and J. W. L. Lewis. "Measurement of Focal Volume Characteristics of Lens-axicon Doublets". Technical report, APS 64th Annual Southeastern Section Meeting, Nashville, TN, November 1997.

[50] C. Parigger, J. W. L. Lewis, and G. Guan. "Focal Volume Intensity Distributions of Lens-axicon Doublets". Technical report, OSA Annual Meeting and ILS-XIII Conference, Long Beach, CA, 1997.

[51] Robert Guenther. *Modern Optics.* John Wiley and Sons, Inc., 1990.

[52] Norman Morrison. *Introduction to Fourier Analysis.* John Wiley & Sons, Inc, 1994.

[53] Ron Bracewell. *The Fourier Transform and Its Applications.* McGraw-Hill Book Company, Stanford University, 1965.

[54] "Tsunami Mode-locked Ti:sapphire Laser User's Manual". Technical report, Spectra-Physics, 1995.

[55] J. C. M. Diels, J. J. Fontaine, I. C. McMichael, and F. Simoni. "Control and Measurement of Ultrashort Pulse Shapes (in Amplitude and Phase) with Femtosecond Accuracy". *Applied Optics*, 24(9):1270–1282, 1985.

[56] C. Yan and J. C. Diels. "Amplitude and Phase Recording of Ultrashort Pulses". *J. Opt. Soc. Amer. B*, 8:1259–1263, 1991.

[57] K. Naganuma, K. Mogi, and H. Yamada. "General Method for Ultrashort Light Pulse Chirp Measurement". *IEEE J. Quantum Electron.*, 25(6):1225–1233, 1989.

[58] J. L. A. Chilla and O. E. Martinez. "Frequency Domain Phase Measurement of Ultrashort Light Pulses. Effect of Noise". *Optics Communications*, 89(5,6):434–440, 1992.

[59] J. L. A. Chilla and O. E. Martinez. "Direct Determination of the Amplitude and the Phase of Femtosecond Light Pulses". *Optics Letters*, 16(1):39–41, 1991.

[60] J. L. A. Chilla and O. E. Martinez. "Analysis of a Method of Phase Measurement of Ultrashort Pulses in the Frequency Domain". *IEEE J. Quantum Electron.*, 27(5):1228–1235, 1991.

[61] D. J. Kane and R. Trebino. "Characterization of Arbitrary Femtosecond Pulses Using Frequency-Resolved Optical Gating". *IEEE J. Quantum Electron.*, 29(2):571–577, 1993.

[62] R. Trebino and D. J. Kane. "Using Phase Retrieval to Measure the Intensity and Phase of Ultrashort Pulses: Frequency-Resolved Optical Gating". *J. Opt. Soc. Am. A*, 10(5):1101–1111, 1993.

[63] J. Paye, M. Ramaswamy, J. G. Fujimoto, and E. P. Ippen. "Measurement of the Amplitude and Phase of Ultrashort Light Pulses from Spectrally Resolved Autocorrelation". *Optics Letters*, 18(22):1946–1948, 1993.

[64] K. C. Chu, J. P. Heritage, R. S. Grant, K. X. Liu, A. Dienes, W. E. White, and A. Sullivan. "Direct Measurement of the Spectral Phase of Femtosecond Pulses". *Optics Letters*, 20(8):904–906, 1995.

[65] D. Meshulach, Y. Barad, and Y. Silberberg. "Measurement of Ultrashort Optical Pulses by Third-Harmonic Generation". *J. Opt. Soc. Am. B*, 14(8):2122–2125, 1997.

[66] Y. Miyamoto, T. Kuga, M. Baba, and M. Matsuoka. "Measurement of Ultrafast Optical Pulses with Two-photon Interference". *Optics Letters*, 18(11):900–992, 1993.

[67] Ying Li, M. Baba, and M. Matsuoka. "Femtosecond Measurement of Fluorescence by Two-photon Interference". *Physical Review A*, 55(4):3177–3183, 1997.

[68] G. Guan, C., and J. W. L. Lewis. "Measurements of femto-second pulses interferences". Technical report, 1998 OSA Annual Meeting and ILS-XIV Conference, Baltimore, MD, October 1998.

[69] X. Zhu, K. G. Spears, and J. Serafin. "Ultrashort Pulsed Laser Coherence Measurements by Sigle-pulse Holography and Four-wave Mixing". *J. Opt. Soc. Am. B*, 6(7):1356–1362, 1989.

[70] J. D. Jackson. *Classical Electrodynamics.* John Wiley and Sons, University of California, Berkeley, second edition edition, 1975.

[71] Anthony E. Siegman. *Lasers.* University Science Books, Stanford University, 1986.

[72] P. W. Milonni and J. H. Eberly. *Lasers.* John Wiley and Sons, New York, 1988.

[73] Jr. S. A. Collins. "Lens-System Diffraction Integral Written in Terms of Matrix Optics". *J. Opt. Soc. Am.*, 60(9):1168–1177, 1970.

[74] H. T. Yura and S. G. Hanson. "Optical Beam Wave Propagation through Complex Optical Systems". *J. Opt. Soc. Am. A*, 4(10):1931–1948, 1987.

[75] J. C. Feltz and M. A. Karim. "Modulation Transfer Function of Charge-Coupled Devices". *Applied Optics*, 29(5):717–722, 1990.

Appendices

Appendix A

Description of Lens System by Beam Propagation Theory

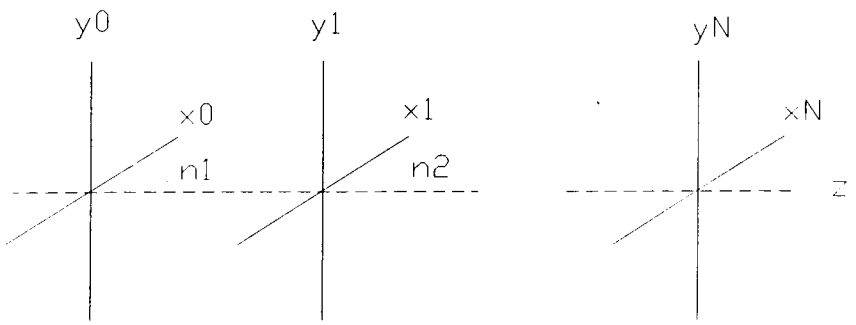

Figure A.1: Schematic Representation of a Lens System.

Figure A.1 shows a schematic representation of a lens system. The input plane is denoted by the subscript 0. The output plane is denoted by the subscript N. In geometric optics an ABCD matrix describes the lens system [51]:

$$\begin{pmatrix} n_N p_N \\ x_N \end{pmatrix} = \begin{pmatrix} A & B \\ C & D \end{pmatrix} \begin{pmatrix} n_1 p_1 \\ x_0 \end{pmatrix} \tag{A.1}$$

where n_i is the refractive index of the medium between (i-1)th-plane and ith-plane. p_i is the slope defined by

$$p_i = (x_i - x_{i-1})/(z_i - z_{i-1}), \tag{A.2}$$

where (x_i, y_i, z_i) is a point in ith-plane as in Fig. A.1. It is obvious that D equals to the linear magnification factor.

The ABCD matrix of a straight distance L is: $\begin{pmatrix} 1 & 0 \\ L & 1 \end{pmatrix}$.

The ABCD matrix of a thin lens is: $\begin{pmatrix} 1 & -1/f \\ 0 & 1 \end{pmatrix}$.

Therefore, the ABCD matrix of a system with a thin lens, object plane at L_1 and image plane at L_2 is:

$$\begin{pmatrix} 1 - L_1/f & -1/f \\ L_1 + L_2 - L_1 L_2/f & 1 - L_2/f \end{pmatrix}. \tag{A.3}$$

If L_1, L_2 are conjugate, the term C is zero.

The beam propagation through the lens system can be described also by using ABCD parameters [73, 74]:

$$\begin{aligned} E_N(x_N, y_N) &= -\frac{ik}{2\pi C} e^{ikL_0} \int\int dx_0 dy_0 E_0(x_0, y_0) \\ &\quad e^{\frac{ik}{2C}[D(x_0^2+y_0^2)-2(x_0 x_N + y_0 y_N)+A(x_N^2+y_N^2)]} \qquad \text{(A.4)} \\ &= e^{ikL_0 + \frac{ik}{2C}(A-1/D)(x_N^2+y_N^2)} \\ &\quad - \frac{ik}{2\pi C} \int\int dx_0 dy_0 E_0(x_0, y_0) e^{\frac{ikD}{2C}[(x_N/D-x_0)^2+(y_N/D-y_0)^2]}. \qquad \text{(A.5)} \end{aligned}$$

The integration can be solved analytically as $C \to 0$,

$$\lim_{C \to 0} E_N(x_N, y_N) = \frac{1}{D} E_0(x_N/D, y_N/D) e^{ikL_0 + \frac{ik}{2C}(A-1/D)(x_N^2+y_N^2)}. \tag{A.6}$$

It is shown that the electrical field has the same distribution pattern of intensity as the source except the linear magnification factor D.

Appendix B

Detector Equations of Charge-Coupled Devices

In the description of the detector equations of charged-coupled devices, one typically assumes the response function $r(x)$ of a one-dimension pixel as a rectangular function, [75]

$$r(x) = \begin{cases} 1 & -a \leq x \leq a \\ 0 & otherwise \end{cases} \tag{B.1}$$

where a is the active width of the pixel.

The optical transfer function (OTF) [51] $R(k)$ is defined as the Fourier transform of the impulse response function $r(x)$,

$$R(k) = \int_{\infty}^{\infty} r(x) e^{ikx} dx = \frac{2sin(ka)}{k}. \tag{B.2}$$

The readout of a pixel at x_0 is:

$$H(x_0) = \int_{-\Delta/2}^{\Delta/2} I(x + x_0) r(x) dx, \tag{B.3}$$

where Δ is the pixel size.

Appendix C

Slit Functions of Spectrometer

A typical monochromator with Czerny-Turner configuration is shown in Fig. C.1. It usually consists of an entrance slit, collecting element, dispersing element, focusing element, an exit slit and detector. Typically, a diffraction grating is the dispersing element.

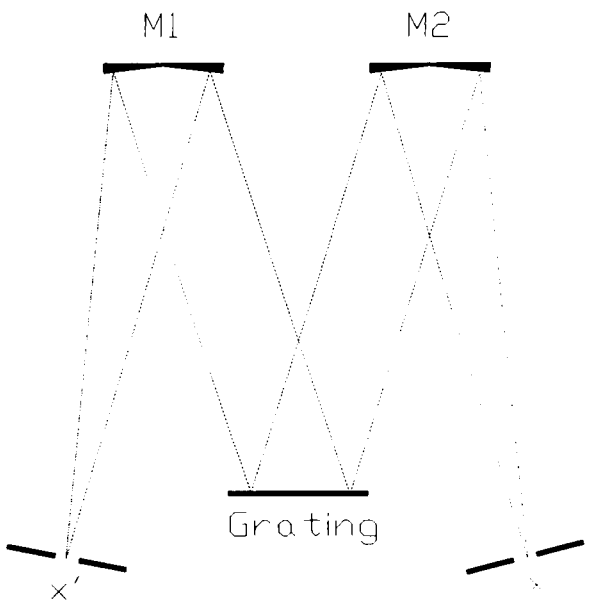

Figure C.1: A typical Czerny-Turner monochromator.

C.1 Grating Equation

The fundamental grating equation is:

$$(sin\alpha + sin\beta) = nd\lambda, \tag{C.1}$$

where d is the grating groove density (grooves/mm), n is the diffraction order, α and β are incident angle and exit angle, respectively.

Usually we arrange the grating in first order, n=1. The position x' of entrance slit, position x of exit slit and the light wavelength λ have following relations,

$$x = (\lambda - \lambda_0)\frac{dx}{d\lambda} - \frac{f'cos\alpha}{fcos\beta}x', \tag{C.2}$$

$$x' = [(\lambda - \lambda_0)\frac{dx}{d\lambda} - x]\frac{fcos\beta}{f'cos\alpha}, \tag{C.3}$$

$$\lambda = \lambda_0 + (x + \frac{f'cos\alpha}{fcos\beta}x')\frac{d\lambda}{dx}, \tag{C.4}$$

where λ_0 is a constant determined by the spectrometer setup, $\frac{d\lambda}{dx}$ is linear dispersion. f and f' are the focal lengths of entrance lens and exit lens, respectively.

C.2 Entrance Slit

One assumes the electric field on the entrance slit as follows,

$$E(\lambda, x') = p(\lambda)A(x'), \tag{C.5}$$

where $p(\lambda)$ is spectral distribution of electric field and $A(x')$ is a filter function.

Both x' and λ map to x through diffraction gratings according to (C.2-C.4). Therefore the electric field on exit plane is:

$$E'(x) = \int_{-a/2}^{a/2} p(\lambda_0 + (x + \frac{f'cos\alpha}{fcos\beta}x')\frac{d\lambda}{dx})A(x')dx', \tag{C.6}$$

where a is the entrance slit width.

For a rectangular filter function

$$A(x') = \begin{cases} 1 & -a/2 \leq x \leq a/2 \\ 0 & otherwise \end{cases}, \tag{C.7}$$

the electric field on the exit plane becomes

$$E'(x) = \int_{-a/2}^{a/2} p(\lambda_0 + (x + \frac{f'cos\alpha}{fcos\beta}x')\frac{d\lambda}{dx})dx'. \tag{C.8}$$

C.3 Exit Slit

According to Appendix B, the readout of detector at point x_0 is:

$$\begin{aligned} s(x_0) &= \int_{x_0-\Delta/2}^{x_0+\Delta/2} r(x)I'(x)dx \\ &= \int_{x_0-\Delta/2}^{x_0+\Delta/2} r(x)E'^2(x)dx, \end{aligned} \tag{C.9}$$

where $r(x)$ is the impulse response function of the detector.

Appendix D

The Bivariate Normal Distribution

The correlation coefficient ρ_{uv} between variables u and v is defined as

$$\rho_{uv} = \frac{\overline{(u-\bar{u})(v-\bar{v})}}{[\overline{(u-\bar{u})^2}\cdot\overline{(v-\bar{v})^2}]^{1/2}} \tag{D.1}$$

$$= \frac{\overline{uv}-\mu_u\mu_v}{\sigma_u\sigma_v}, \tag{D.2}$$

where σ_u and σ_v are the variances of u and v, μ_u and μ_v are the averages of u and v. The bivariate normal distribution for two variables (u,v) [1] is defined by the joint probability distribution,

$$p(u,v) = \frac{1}{2\pi\sigma_u\sigma_v(1-\rho_{uv}^2)^{1/2}} e^{-G(u,v;\mu_u,\mu_v;\sigma_u,\sigma_v)/2}, \tag{D.3}$$

where $G(u,v;\mu_u,\mu_v;\sigma_u,\sigma_v)$ is defined as

$$G = \frac{1}{1-\rho_{uv}^2}[(\frac{u-\mu_u}{\sigma_u})^2 - 2\rho_{uv}\frac{(u-\mu_u)(v-\mu_v)}{\sigma_u\sigma_v} + (\frac{v-\mu_v}{\sigma_v})^2]. \tag{D.4}$$

Vita

Guoming Guan was born in Jiangdu, Jiangsu province of China on Dec. 12 1966. He graduated from high school in 1985 and enrolled in Beijing University. He graduated from Beijing University with a B.S. degree in physics in 1989 and enrolled at the Shanghai Institute of Optics and Fine Mechanics (SIOFM) to pursue a graduate degree. In 1992 he graduated from SIOFM with a M.S. degree in optics. From 1992 to 1994 he worked as an electro-optics engineer in a semiconductor device company. In 1994 he enrolled in the graduate school at The University of Tennessee Space Institute to pursue a Ph.D. degree in physics. He completed studies with the Ph.D. degree in December 1998.